DOTTORATO DI RICERCA IN

"*Ingegneria Industriale e dell'Affidabilità*"

CICLO *XXVI*

COORDINATORE Prof. Maurizio De Lucia

REFERENTE Prof. Mario Tucci

MODELLING, CONTROL AND TESTING OF UNDERWATER MOBILE ROBOTS

Settore Scientifico Disciplinare ING-IND/13

Dottorando
Ing. *Alessandro Ridolfi*

Tutore
Prof. *Benedetto Allotta*

DRAFT VERSION FOR 31/12/2013

Anni 2011/2013

Ai miei genitori

e a mio nonno Fosco,

che mi hanno sempre supportato nel percorso di studi

Contents

List of Figures

Ringraziamenti

La presente tesi di dottorato nasce dal coinvolgimento del Laboratorio di Modellazione Dinamica e Meccatronica (MDM Lab) del Dipartimento di Ingegneria Industriale, ex Dipartimento di Energetica "Sergio Stecco", dell'Università degli Studi di Firenze in una serie di importanti progetti di Robotica Sottomarina durante gli anni 2010-2013. I due principali progetti di Robotica Sottomarina che hanno visto e vedono coinvolto l'MDM Lab sono il progetto regionale THESAURUS (TecnicHe per l'Esplorazione Sottomarina Archeologica mediante l'Utilizzo di Robot aUtonomi in Sciami) ed il progetto europeo ARROWS (ARchaeological RObot systems for the World's Seas): di quest'ultimo l'MDM Lab è sia partner tecnico che coordinatore.

Le esperienze vissute in tale settore, sommate alle altre attività svolte nei tre anni di dottorato, hanno senza dubbio arricchito le mie competenze teniche, organizzative e relazionali.

Il mio primo ringraziamento è rivolto al Professore Benedetto Allotta, mio tutor di dottorato, ed al Professore Paolo Toni che mi hanno sempre seguito con grande professionalità ed attenzione, riponendo su di me fiducia e grandi aspettative, alle quali spero di aver risposto positivamente; la loro guida, unita a quella dei miei co-tutor di dottorato, l'Ing. Andrea Rindi e l'Ing. Enrico Meli, hanno alimentato il mio senso di responsabilità, impegno e motivazione per le discipline della robotica e della meccanica applicata in generale.

Un sincero ringraziamento è poi rivolto a tutti i miei colleghi, presenti e passati, con i quali spero di aver instaurato un legame di amicizia, stima e collaborazione reciproca che vada oltre il puro rapporto professionale, a cominciare dagli Ingg. Riccardo Costanzi, Roberto Conti, Andrea Giusti e Gregorio Vettori e proseguendo con gli Ingg. Luca Pugi e Monica Malvezzi con i quali ho lavorato a fianco in molti progetti ed anche durante la mia tesi specialistica, a tutti i colleghi con i quali ho trascorso una piacevole "convivenza" negli uffici fiorentini, Ingg. Susanna Papini, Francesco Cangioli, Mirko Ignesti, Stefano Falomi e Alice Innocenti e finendo, ma non per ordine di importanza, con i "colleghi pistoiesi" Ingg. Fabio Bartolini, Jury Auciello, Lorenzo Marini, Niccolò Monni, Johnatan Gelli, Marco Natalini e Pierluca D'Adamio.

Infine, un doveroso ringraziamento a tutti i tesisti con cui ho collaborato e che ho

cercato di aiutare nelle varie attività, ed ai colleghi, Professori e ricercatori conosciuti durante questi tre anni di lavoro: in particolare, un ringraziamento speciale è rivolto al Prof. Andrea Caiti, coordinatore del progetto THESAURUS, al geologo Francesco Mugnai, al Prof. Nicola Casagli, al Prof. Andrea Arnone, agli Ingg. Claudio Fantacci, Davide Fenucci e Matteo Checcucci ed un ultimo sentito ringraziamento all'Ing. Stefano Biagini del NATO CMRE (NATO Centre for Maritime Research and Experimentation), ex NURC, di La Spezia.

Firenze, 30 Gennaio 2014

Alessandro

Introduction

The present work deals with the modelling, control and construction of underwater robots, developed by the Mechatronics and Dynamic Modelling Laboratory (MDM Lab) of the Department of Industrial Engineering of the University of Florence, during the years 2011-2013.

The research group of the MDM Lab, Department of Industrial Engineering (ex Department of Energy Engineering) works, more generally speaking, in the study of two typologies of underwater vehicles: AUVs (Autonomous Underwater Vehicle) and ROVs (Remotely Operated Vehicle), which are both classified as UUVs (Unmanned Underwater Vehicle), i.e. vehicles able to navigate without a human presence on board. These studies started thanks to the funding for underwater archaeologist purposes. A ROV is a teleoperated robot employed in underwater applications, usually including maintenance or monitoring operations which are particularly difficult or dangerous. Examples of these ones are the Nemo ROV (chapter 2) used by the University of Florence to monitor the "Costa Concordia wreck" and the ROVs used to intervene on the underwater Oil&Gas platforms. ROVs differ from an AUV, which is on the contrary a programmable robot able to navigate underwater without being driven by a pilot and on which the main attentions of the MDM Lab have been and are concentrated, because of the need of a remote connection, generally a cable, with an external operator, allowing on the control and the power supply for the mobile robot. The aim to make completely autonomous an underwater vehicle, which is in general endowed with different types of sensors, e.g. cameras or mechanical arms, is justified by the will to solve some problems linked to the use of the ROVs, such as the communication troubles and delays present underwater, and, generally speaking, problems concerning a remote type control (inconveniences which are mainly due to the presence of long cables).

The AUVs are employed nowadays for a large variety of missions: for commercial aims from Oil&Gas industries, to realize detailed maps of sea-beds before starting to build platforms rigs, for military aims, to set out the presence of mines or unidentified objects in an area of interest, or used in anti-submarine missions, in the field research activities to study flora and fauna of lakes and seas, to monitor the quality of the sea waters (temperature, biological activity, salinity, dissolved oxygen, water turbidity, etc.). These vehi-

cles vary their own dimensions, from the “portable” ones for man to great diameters and lengths of over 10 m; they have similar designs for most of missions and navigate following a predetermined route with a controlled cruising speed between 1 and 4 knots.

The study and the design of underwater vehicles started at MDM Lab as a result of the awarding of the THESAURUS project in 2010 (TecnicHe per l'Esplorazione Sottomarina Archeologica mediante l'Utilizzo di Robot aUtonomi a Sciami) from Regione Toscana, which had the aim to develop multidisciplinary scientific methodologies useful to individualize, survey, register and document artefacts and underwater wrecks of archaeological, historical-artistic and anthropological value, which are in the Tuscan Archipelago. The attainment of such a goal scheduled the design and testing of Autonomous Underwater Vehicles equipped with optical, acoustic and magnetic instruments for navigation, monitoring and reconstruction of the seabed just as three-dimensional interactive virtual environment; the robotic fleet members are able to cooperate and communicate to the outside in real time. Particularly, the contribution of the Department of Industrial Engineering (ex Department of Energy Engineering) of the University of Florence inside the project related to the design and control of each single vehicle belonging to the swarm, named Typhoon [38], [8], [25]. The work developed on THESAURUS (topic described in chapter 1), in particular the project of the control system of navigation algorithm through the use of on board sensors, integrated in a mathematical model implemented in Matlb-Simulink^{TM} environment [1] has made up the starting point for the herein presented work.
To remain within the limits of underwater exploration with an archaeologist aim the MDM Lab is planning, in these years, other autonomous AUV vehicles within the ARROWS (ARchaeological RObot systems for the World's Seas) European Project [9]. This project is financed by the FP7 of the European Community: the planned heterogeneous AUV swarm will carry out mapping underwater missions, diagnoses and cleaning demonstrations in interesting archaeological sites in the sea of Sicily and in the Baltic Sea. In the perspective to develop its own expertises and competences in the field of underwater robotics the MDM Lab of the University of Florence took part in 2012, for the first time, and in 2013, for the second time, in SAUC-e competition (Student Autonomous Underwater Challenge - Europe) [10] [40] [39]. SAUC-e is a University competition at European level among autonomous underwater vehicles developed by different Universities, born in 2006 and arrived this year at the 8th edition; in 2012 and 2013 it took place at the ex NURC (NATO Undersea Research Centre) basin, currently called CMRE (Centre for Maritime Research and Experimentation), in La Spezia, Italy.

During the THESAURUS project, the MDM Lab thanks to the collaboration with the Department of the Earth Sciences of the University of Florence developed a mini-ROV, called Nemo (topic described in chapter 2). The specific goal of Nemo ROV is to have a detailed vision of the areas which are hardly accessible by divers and experts: it has been specifically designed and built to monitor the Costa Concordia wreck, at Isola del Giglio. Particularly the submarine, remotely piloted, has to operate as a robotised camera and be able to scan the wreck inside areas too. The second specification identifies with the very reasonable dimensions of the vehicle and the high control accuracy of its movements in restricted environments. Besides, the ROV must be simple to be driven in order to allow a general user to employ it promptly (according to this aim, a dedicated graphic interface has been developed).

Another research interesting topic (chapter 3) in the underwater robotics field that has affected the MDM Lab research group is the possibility to mount a robotic arm on an AUV. These complex mobile robots are known as I-AUVs (Intervention - Autonomous Underwater Vehicle). There are already several applicative examples [2] [3] of remote controlled underwater vehicles equipped with arms, composing what in robotics is called a telemanipulation system. Generally speaking a telerobot [4] is a system controlled by a human operator through a process such as Human-in-the-loop. All the "high level" decisions are the operator's duty, while the robot is just responsible for their mechanical execution.

Problems coming from the communication delay and the use in environment whose geometrical and physical characteristics are usually not totally known beforehand, make telemanipulation a branch of science which is called advanced robotics. The possibility to use an on board manipulator on an autonomous underwater vehicle is an even more complex topic of research. Despite up to now the use of telemanipulators on ROV vehicles appears to be widespread enough, concerning the AUVs only a few examples of vehicles equipped with a robotic arm are present in literature [5] [6] [7]. Moreover, in these cases the manipulator is always kept in a rest position while the vehicle is moving and used just when the underwater robot is still, because reducing its use to hovering phases it is possible to control separately the master system and the slave, uncoupling the tracking trajectory problem from the one of the arm handling for manipulation.
The study of a control strategy dealing with the two problems at the same time appears to be more complex; this strategy would allow this way to handle objects by the arm while the mobile robot is moving, at limited speed, following a desired trajectory. The last problem represents a topic of advanced study (important contributions in literature are still limited) and some preliminary ideas and simulation results will be treated in the third part of this dissertation. The recent interest about this subject is easily explainable con-

Figure 1: ROV Panther, example of an underwater robot equipped with two telemanipulators (China National Oil)

sidering the large range of specific applications a complete autonomous underwater manipulation system might have, among which water samplings at different depths, coring or acquisition of specimen of minerals, animals and plants, the conception of robotic systems able to replace or help the scuba-divers in maintenance (e.g. welds) on oil platforms and in many other complex operations (not least, the ones linked to monitoring and protection of archaeological sites).

Chapter 1

Typhoon AUV

1.1 State of the art of AUVs

An AUV (Autonomous Underwater Vehicle) is an underwater mobile robot able to navigate without any intervention of an external user (pilot).

The first AUV dates back to 1957 and was developed in the laboratories of applied physics at the University of Washington under the name of SPURV (Special Purpose Underwater Research Vehicle); it was built to perform studies of diffusion, acoustic transmission and submarine measurements. Other AUVs were developed in the seventies by the Massachusetts Institute of Technology (MIT). Until relatively recently the AUVs have been used for a very small number of operations, but with the evolution of the available technologies now are used in a wide variety of missions.

In general, the AUVs have very different sizes; there are both "portable" ones both with large diameters and lengths, exceeding 10 m. The advantages of larger vehicles consist in greater autonomy and a greater number of sensors transportable; the smaller ones, instead, benefit from a more simple logistics (avoiding e.g. support vessels, launch and recovery systems). Throughout the world there are about a dozen companies that produce AUVs for sale; the market is basically divided into three parts: scientific, commercial and military use. The majority of missions use similar design and are performed in the cruise mode (i.e. data collection by following a predetermined path with a controlled speed between 1 and 4 knots).

The most common applications are:

- **Commercial -** oil industries use AUVs to make detailed maps of the seabed before starting to build platforms;
- **Military field -** a typical military mission for an AUV is to map an area to determine if there are mines, or to monitor protected areas. The AUV can also be employed in

anti-submarine missions, to assist in the localization of enemy submarines;

- **Research -** scientists use AUVs to study lakes, oceans and their flora. They can be equipped with different sensors to determine the concentration of various elements, the absorption or reflection of light and the presence of microscopic life;
- **Hobby -** many hobbyists build AUV for pleasure. Such amateur vehicles can participate in national and international competitions where they compete in the achievement of predetermined objectives.

1.2 THESAURUS project

The THESAURUS project (TecnicHe per l'Esplorazione Sottomarina Archeologica mediante l'Utilizzo di Robot aUtonomi in Sciami, 2011-2013) had the aim to develop multidisciplinary scientific methodologies useful to individualize, survey, register and document artefacts and underwater wrecks of archaeological, historical-artistic and anthropological value, in the Tuscan Archipelago.

The team of partners included two Universities (Centro Interdipartimentale di Ricerca in Robotica e Bioingegneria E. Piaggio, University of Pisa - MDM Lab of the Department of Industrial Engineering, ex Department of Energy Engineering "Sergio Stecco", University of Florence) with specific know-how in Underwater Robotics and marine sensors, in navigation and control of underwater robots and data analysis; one research institution (Istituto di Scienze e Tecnologie dell'Informazione, Pisa, Consiglio Nazionale delle Ricerche) with experience in image elaboration, 3D representation and data analysis; Scuola Normale Superiore, Pisa, with specific know-how in the field of historical and archaeological research and in multimedia data management.

The project dealt with the design and testing of AUVs for the survey of the seabed of archaeological interest with optical, acoustic and magnetic instruments. These low-cost, programmable vehicles, usable from the surface to a depth of 300 m, will in future be a useful tool for the understanding and protection of the historical and archaeological heritage still present on the seabed.

The THESAURUS project focuses on the Tuscan Archipelago, rich in ancient and modern archaeological remains, whose history can be reconstructed thanks to archival sources, documentaries and technological applications developed in the framework of the project. The reconstruction of the seabed as an interactive 3D virtual environment will be used to tell the story of underwater archaeological sites, difficult to access by the general public.

In particular, the MDM Lab of the University of Florence faced the design (Figure 1.1), the modelling, navigation and control of the AUV, called Typhoon. In this chapter part of the work of the MDM Lab within the THESAURUS project is described, mainly focusing

Figure 1.1: Typhoon design evolution

on the modelling and navigation topics and on the final sea testing, made in September 2013.

The technical requirements of a single Typhoon AUV are:

- Maximum reachable depth: 300 m;
- Maximum speed: 5-7 knots;
- Cruise speed: 3-4 knots;
- Autonomy: about 8 hours.

The underwater fleet, composed of 3 vehicles able to communicate among themselves through proper acoustic modems, working principle is the following:

- One AUV moves near the surface, to be able to get the GPS signal (thus knowing accurately its position) and to communicate it to the other AUVs;
- Two AUVs navigating underwater: one of them has a Doppler Velocity Sensor (DVL) on board.

In Figure 1.2 a final CAD design of Typhoon AUV is displayed.

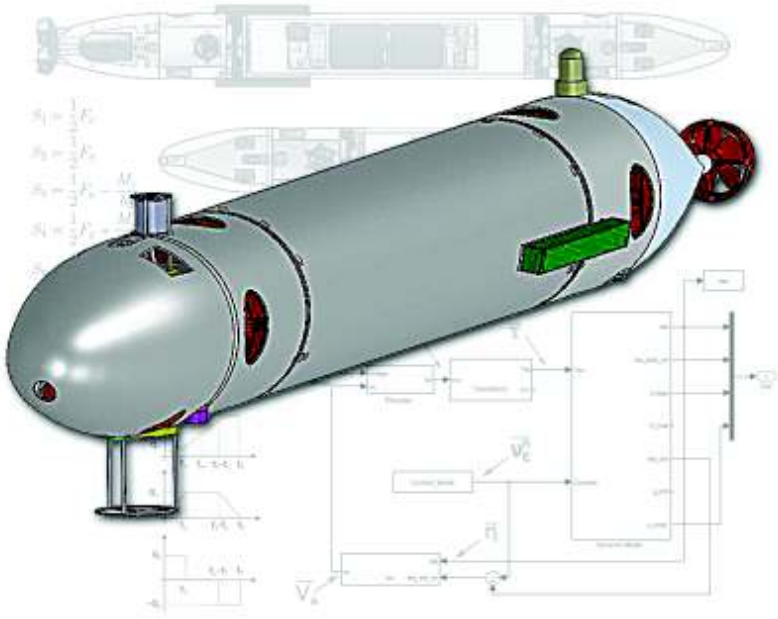

Figure 1.2: Typhoon AUV

1.3 Modelling of an underwater vehicle

The modelling of an underwater vehicle (as well the one of a whatever rigid body) includes the study of kinematics and dynamics of the body itself. In this section the kinematic and dynamic quantities allowing the description of the motion according to the classical notation for sea vehicles by SNAME (Society of Naval Architects and Marine Engineers, 1950) and a mathematical model representing the motion of a rigid body with 6 degrees of freedom (DOFs) freely moving into a fluid are presented [1]. This model has afterwards been made applicable to the specific vehicle, Typhoon AUV, through the adoption of a simplified treatment according to the body shape and the CFD calculations of its hydrodynamic parameters. Finally some elements of non-ideality have been integrated, such as the presence of propellers providing the thrusts for the vehicle handling and the possible presents of sea currents (disturbing elements) investing the vehicle body during the navigation.

1.3.1 Kinematics of an underwater vehicle

In order to analyse the motion of an underwater vehicle it is advisable to set out two different reference frames, shown in Figure 1.3:

- **"Body" frame $< b >$:** reference frame with origin O^b placed in the center of mass of the body and axes lined up to the main inertia axes of the body itself. In case of a vehicle of regular shape, x^b axis is longitudinal, pointing to the forward motion,

z^b axis is vertical downward and y^b axis is set out in order to form a right-handed frame with the other two axes;

- **"Fixed" frame $< n >$:** inertial reference frame, described for the analysed scene as the frame with origin O^n placed on the surface and axes lined up to the ones of a NED (North-East-Down) frame. x^n axis heads to the north, y^n axis heads to the east and z^n axis to the bottom.

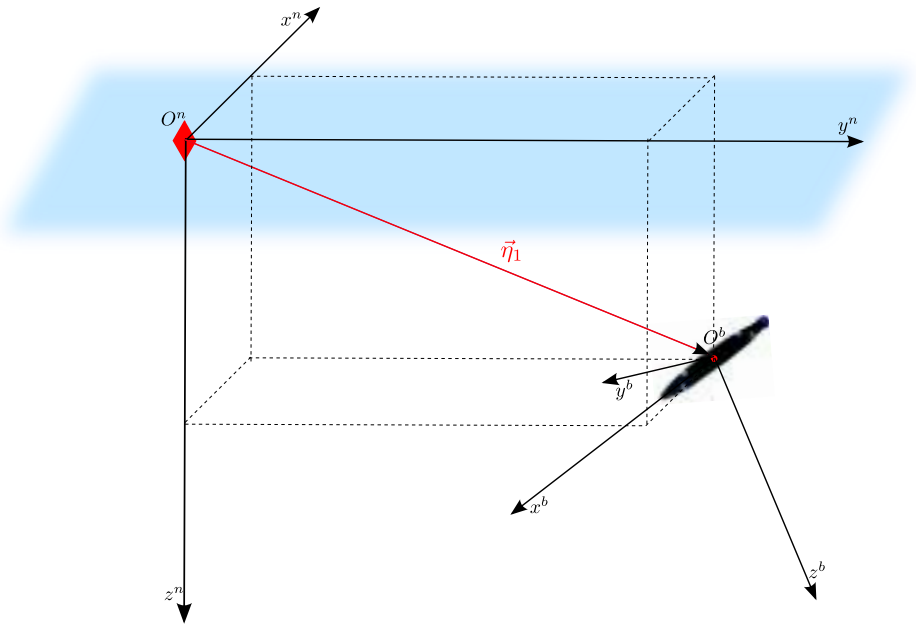

Figure 1.3: Body frame $< b >$ and fixed frame $< n >$

As it has been advanced, the motion of an underwater vehicle having 6 degrees of freedom has been taken into consideration: 6 are the coordinates necessary to calculate the position and orientation of a rigid body in the space. According to SNAME notation the following coordinate vectors are set out:

$$\begin{aligned}
\vec{\eta} &= \left[\vec{\eta}_1^{\top}\ \vec{\eta}_2^{\top}\right]^{\top} \quad \text{with} \quad \vec{\eta}_1 = [x\ y\ z]^{\top} \quad \vec{\eta}_2 = [\varphi\ \vartheta\ \psi]^{\top} \\
\vec{\nu} &= \left[\vec{\nu}_1^{\top}\ \vec{\nu}_2^{\top}\right]^{\top} \quad \text{with} \quad \vec{\nu}_1 = [u\ v\ w]^{\top} \quad \vec{\nu}_2 = [p\ q\ r]^{\top} \\
\vec{\tau} &= \left[\vec{\tau}_1^{\top}\ \vec{\tau}_2^{\top}\right]^{\top} \quad \text{with} \quad \vec{\tau}_1 = [X\ Y\ Z]^{\top} \quad \vec{\tau}_2 = [K\ M\ N]^{\top},
\end{aligned} \tag{1.1}$$

where $\vec{\eta}$ represents the vector of position $(\vec{\eta}_1)$ and orientation $(\vec{\eta}_2)$ in the fixed frame $< n >$, $\vec{\nu}$ includes the components of linear $(\vec{\nu}_1)$ and angular $(\vec{\nu}_2)$ speeds, expressed in the body frame $< b >$ and $\vec{\tau}$ are the forces $(\vec{\tau}_1)$ and torques $(\vec{\tau}_2)$ applied to the vehicle, expressed in the body frame $< b >$.
As concerns the nomenclature of the degrees of freedom:

- x motion along x^b axis is defined *surge* motion;
- y motion along y^b axis is defined *sway* motion;
- z motion along z^b axis is defined *heave* motion;
- φ rotation around x^b axis is defined *roll* motion;
- ϑ rotation around y^b axis is defined *pitch* motion;
- ψ rotation around z^b axis is defined *yaw* motion.

It is easily possible to link the quantities expressed in the fixed frame $< n >$ and the quantities given in the body frame $< b >$ at "speed level". As regards the translational part:

$$\dot{\vec{\eta}}_1 = R_b^n\left(\vec{\eta}_2\right)\vec{\nu}_1\,, \tag{1.2}$$

where $R_b^n\left(\vec{\eta}_2\right)$ is the rotation matrix between $< b >$ and $< n >$ that, as a function of the Euler Roll-Pitch-Yaw angles (RPY) $\left[\varphi,\vartheta,\psi\right]^T$, is equal to:

$$R_b^n\left(\vec{\eta}_2\right) = \begin{bmatrix} c_\psi c_\vartheta & -s_\psi c_\varphi + c_\psi s_\vartheta s_\varphi & s_\psi s_\varphi + c_\psi c_\varphi s_\vartheta \\ s_\varphi c_\vartheta & c_\psi c_\varphi + s_\psi s_\vartheta s_\varphi & -c_\psi s_\varphi + s_\psi c_\varphi s_\vartheta \\ -s_\vartheta & s_\varphi c_\vartheta & c_\varphi c_\vartheta \end{bmatrix}\,, \tag{1.3}$$

using for the generic angle α

$$c_\alpha = cos\left(\alpha\right)\,,\; s_\alpha = sin\left(\alpha\right)\,. \tag{1.4}$$

As regards instead the orientation part:

$$\dot{\vec{\eta}}_2 = T_b^n\left(\vec{\eta}_2\right)\vec{\nu}_2\,, \tag{1.5}$$

where the transform matrix $T_b^n\left(\vec{\eta}_2\right)$ is defined as function of RPY angles as:

$$T_b^n\left(\vec{\eta}_2\right) = \frac{1}{c_\vartheta}\begin{bmatrix} c_\vartheta & s_\varphi s_\vartheta & c_\varphi s_\vartheta \\ 0 & c_\varphi c_\vartheta & -c_\vartheta s_\varphi \\ 0 & s_\varphi & c_\varphi \end{bmatrix}\,. \tag{1.6}$$

As notable from (1.6), the RPY angle representation has a singularity when $\vartheta = (2n+1)\frac{\pi}{2}$, with $n \in \mathbb{N}$. This problem could be overcome by introducing an alternative representation of the orientation of redundant type, e.g. using the components of the unitary quaternion. In short, the relationship linking vectors $\dot{\vec{\eta}}$ and $\vec{\nu}$ is expressed like this:

$$\dot{\vec{\eta}} = J_b^n\left(\vec{\eta_2}\right)\,\vec{v}\,, \tag{1.7}$$

where

$$J_b^n\left(\vec{\eta_2}\right) = \begin{bmatrix} R_b^n\left(\vec{\eta_2}\right) & 0_{3\times3} \\ 0_{3\times3} & T_b^n\left(\vec{\eta_2}\right) \end{bmatrix}. \tag{1.8}$$

Using equation (1.7) it is possible to write also relationships between the time derivatives of the same quantities:

$$\begin{aligned} \dot{\vec{\eta}} &= J_b^n\,\vec{v} && \Leftrightarrow\ \vec{v} = \left(J_b^n\right)^{-1}\dot{\vec{\eta}} \\ \ddot{\vec{\eta}} &= J_b^n\,\dot{\vec{v}} + \dot{J}_b^n\,\vec{v} && \Leftrightarrow\ \dot{\vec{v}} = \left(J_b^n\right)^{-1}\left(\ddot{\vec{\eta}} - \dot{J}_b^n\left(J_b^n\right)^{-1}\dot{\vec{\eta}}\right), \end{aligned} \tag{1.9}$$

leaving out the explicit dependence from the variables to simplify the notation.

1.3.2 Equations of motion of an underwater vehicle

The motion of a rigid body in underwater environment can be described as a function of the previously defined coordinates, by the following equation of motion:

$$M_{RB}\dot{\vec{v}} + C_{RB}(\vec{v})\vec{v} = \vec{\tau}_{RB}\,, \tag{1.10}$$

where $\vec{\tau}_{RB}$ is the vector of forces and external moments acting on the body, M_{RB} and C_{RB} are the mass and centrifugal and Coriolis effect matrices.

These actions can be classified as environmental disturbances $\vec{\tau}_E$ (sea currents, waves, wind), propulsive actions $\vec{\tau}$ (thrusts of the propulsion systems, forces due to the presence of control surfaces, such as rudders) and forces and torques $\vec{\tau}_H$ of hydrodynamic and hydrostatic nature.

The last ones are commonly given by the sum of three effects: the hydrodynamic damping, the gravity and buoyancy forces and the effects caused by added mass and inertia, whose meaning will be explained later on. In conclusion:

$$\vec{\tau}_{RB} = \vec{\tau}_H + \vec{\tau}_E + \vec{\tau}\,, \tag{1.11}$$

with

$$\vec{\tau}_H = -M_A\dot{\vec{v}} - C_A(\vec{v})\vec{v} - D(\vec{v})\vec{v} - \vec{g}(\vec{\eta})\ . \tag{1.12}$$

M_A and $C_A(\vec{v})$ are respectively the matrices of mass and added centrifugal and Coriolis effects, $D(\vec{v})$ the matrix of hydrodynamic damping; $\vec{g}(\vec{\eta})$ represents the gravity and buoyancy effects. Replacing (1.11) and (1.12) inside (1.10):

$$M\dot{\vec{v}} + C(\vec{v})\vec{v} + D(\vec{v})\vec{v} + \vec{g}(\vec{\eta}) = \vec{\tau} + \vec{\tau}_E \,, \tag{1.13}$$

having defined the general matrices of mass and the centrifugal and Coriolis effects,

$$M = M_{RB} + M_A \tag{1.14}$$

$$C = C_{RB} + C_A \ . \tag{1.15}$$

O^b origin of $< b >$ reference frame, linked to the body in motion, coincides with the center of mass of the vehicle and its axes are linked up with the principal inertia directions. For this reason, M_{RB}, the mass matrix linked to the rigid body dynamics, takes the simple diagonal form:

$$M_{RB} = \begin{bmatrix} m & 0 & 0 & & & \\ 0 & m & 0 & & 0_{3\times3} & \\ 0 & 0 & m & & & \\ & & & I_{xx} & 0 & 0 \\ & 0_{3\times3} & & 0 & I_{yy} & 0 \\ & & & 0 & 0 & I_{zz} \end{bmatrix}, \tag{1.16}$$

where m is the mass of the vehicle, while I_{ii} represents its barycentric moment of inertia with respect to the i-th axis. Also C_{RB} matrix takes a simplified form, with this particular choice of the relative reference frame and turns out to be block diagonal:

$$C_{RB} = \begin{bmatrix} 0 & -mr & mq & & & \\ mr & 0 & -mp & & 0_{3\times3} & \\ -mq & mp & 0 & & & \\ & & & 0 & I_{zz}r & -I_{yy}q \\ & 0_{3\times3} & & -I_{zz}r & 0 & I_{xx}p \\ & & & I_{yy}q & -I_{xx}p & 0 \end{bmatrix}. \tag{1.17}$$

1.3.3 Hydrodynamic and buoyancy effects

The hydrodynamic effects acting on a rigid body in motion inside a fluid are mainly of two types:

- **Added mass and inertia**: contribution linked to the inertia of the fluid, adhering to the vehicle surface, and being therefore accelerated with the vehicle itself;

- **Lift and drag (hydrodynamic resistance)**: contribution taking into account the acting force of the body which moves comparatively to the viscous fluid where it is immersed.

As regards the static effects, on the contrary, these ones are produced by the combinations of the gravity and buoyancy forces, responsible of the so called "restoring forces".

Added mass and inertia - This effect, typically neglected in the dynamic modelling of land vehicles or industrial robots, in virtue of the consideration that air density is decidedly lower than the one of the body in motion, becomes significant in underwater scenarios, as fluid density on the contrary can be compared to the vehicle one. The added, or virtual, mass effect usually explained as that part of the fluid, which, in virtue of the adhesion condition to the wall, needs an additional force to be accelerated and slowed down together with the vehicle, can be more precisely traced back to the forces and moments caused by the pressure field starting as a result of a forced harmonic motion of the body. These forces are proportional to the acceleration of the body itself, with a phase shift of 180° compared to the oscillations characterizing its motion. In the same way for dynamic contributions of the rigid body, the effect of those terms is modelled introducing a M_A added mass and inertia matrix and a C_A matrix of added centrifugal and Coriolis effects. To the aim of the examined application, the hypotheses the vehicle is totally immersed, it presents three planes of symmetry and moves at limited speed can be considered valid, M_A matrix gets a diagonal shape:

$$M_A = -\text{diag}\left\{X_{\dot{u}}, Y_{\dot{v}}, Z_{\dot{w}}, K_{\dot{p}}, M_{\dot{q}}, N_{\dot{r}}\right\} , \tag{1.18}$$

where the hydrodynamic force of added mass Y_A along y axis, caused by a $\dot{u}$ acceleration in x direction, is given by:

$$Y_A = Y_{\dot{u}}\,\dot{u} , \quad \text{con} \quad Y_{\dot{u}} = \frac{\partial Y}{\partial \dot{u}} . \tag{1.19}$$

For totally immersed bodies M_A matrix is, in the same way as mass matrix of a rigid body, strictly positive. As regards C_A matrix, on the contrary, this one is always skew-symmetric, depending on speed, and, under the previous hypotheses, gets the form:

$$C_A = \begin{bmatrix} 0 & 0 & 0 & 0 & -Z_{\dot{w}}\,w & Y_{\dot{v}}\,v \\ 0 & 0 & 0 & Z_{\dot{w}}\,w & 0 & -X_{\dot{u}}\,u \\ 0 & 0 & 0 & -Y_{\dot{v}}\,v & X_{\dot{u}}\,u & 0 \\ 0 & -Z_{\dot{w}}\,w & Y_{\dot{v}}\,v & 0 & -N_{\dot{r}}\,r & M_{\dot{q}}\,q \\ Z_{\dot{w}}\,w & 0 & -X_{\dot{u}}\,u & N_{\dot{r}}\,r & 0 & -K_{\dot{p}}\,p \\ -Y_{\dot{v}}\,v & X_{\dot{u}}\,u & 0 & -M_{\dot{q}}\,q & K_{\dot{p}}\,p & 0 \end{bmatrix} . \tag{1.20}$$

Lift and drag - Whenever exists a relative motion between a rigid body and the viscous fluid surrounding it, on the body acts a resulting force whose intensity is due to many factors (relative speed, shape, dimensions of the body, fluid properties) and which is traditionally subdivided into the component parallel to the motion direction, said "drag force" and into the orthogonal component "lift force". Drag and lift forces are conceptually found integrating the wall tangential shears due to viscosity (friction contribution) and the normal efforts due to the local pressure of the fluid (shape contribution) on the whole wet body surface.

In case of small autonomous robots, assuming motions along the directions of the main axes, lift forces can be reasonably ignored, also considering the fact that control surfaces, such as wings or rudders, have not been included in the schematization and the design of the vehicle. As regards on the contrary drag forces, their damping effect is significant in the study of the dynamic behaviour of an underwater vehicle, as it poses an important contribution of non-linearity inside the motion equations. A common simplification is to consider only forces with linear and quadratic speed dependence. In this case, for a totally immersed body, and characterized by three planes of symmetry, $D(\vec{v})$ hydrodynamic damping matrix, introduced in (1.12), is diagonal and defined positive and given by the expression:

$$\begin{aligned} D = &- \operatorname{diag}\left\{X_u, Y_v, Z_w, K_p, M_q, N_r\right\} + \\ &- \operatorname{diag}\left\{X_{u|u|}|u|, Y_{v|v|}|u|, Z_{w|w|}|w|, K_{p|p|}\left|p\right|, M_{q|q|}\left|q\right|, N_{r|r|}|r|\right\} . \end{aligned} \tag{1.21}$$

Assuming a diagonal for the damping matrix means to ignore the coupling of dissipative terms: this is reasonable if speeds are not high, as in case of small autonomous robots whose speed of advance is usually controlled under 3-4 knots.
Considering the linear friction terms are not so important compared to drag forces (quadratic) and that in any case it would have been difficult to separate the two contributions in the results of the carried out CFD simulations, the first term in (1.21) is fixed equal to zero, while only $X_{iu_j|u_j|}$ coefficients are estimated.
Gravity and buoyancy - As it has been announced in advance, $\vec{g}\left(\vec{\eta}\right)$ term in (1.13) is the result of the combination between gravity force and buoyancy force. Buoyancy is the vertical force operating on a immersed body and it does not depend on the relative motion between vehicle and fluid, but exclusively on the body geometry and its mean density (hydrostatic effect).
$\vec{g}^{\,n}$ vector is set out as the gravitational acceleration expressed in the fixed frame $< n >$:

$$\vec{g}^{\,n} = [0 \;\; 0 \;\; 9.81]^{\top} \,\mathrm{m/s^2} \,. \tag{1.22}$$

If V_{rb} is the vehicle volume (completely immersed, for hypothesis), m its mass and ρ_a the water local density, the module of weight force $\left\|\vec{W}\right\|$ and the module of the buoyancy force $\left\|\vec{B}\right\|$ are given by:

$$\begin{aligned} W &= \left\|\vec{W}\right\| = m \left\|\vec{g}^{\,n}\right\| \\ B &= \left\|\vec{B}\right\| = \rho_a V_{rb} \left\|\vec{g}^{\,n}\right\| \,, \end{aligned} \tag{1.23}$$

with both forces directed along z^n axis, the former towards the bottom and the latter to the top. Therefore the weight force $\vec{f}_G^{\,b}$ expressed in the body frame $< b >$, put in the center of mass of the vehicle coinciding with the origin of $< b >$ itself, is equal to:

$$\vec{f}_G^{\,b} = R_n^b \begin{bmatrix} 0 \\ 0 \\ W \end{bmatrix} \,, \tag{1.24}$$

where R_n^b represents the inverse transformation compared to (1.3), equal to $R_n^b = \left(R_b^n\right)^{\top}$, according to the properties of the rotation matrices.
Buoyancy force $\vec{f}_B^{\,b}$ is instead, in the body frame $< b >$:

$$\vec{f}_B^{\,b} = -R_n^b \begin{bmatrix} 0 \\ 0 \\ B \end{bmatrix} \,. \tag{1.25}$$

This force is applied in the center of buoyancy, identified by vector $\vec{r}_B^{\,b}$, with coordinates:

$$\vec{r}_B^{\,b} = \left[x_B^b \; y_B^b \; z_B^b\right]^{\top} \,. \tag{1.26}$$

Vector $\vec{g}\left(\vec{\eta}\right)$ is thus given by

$$\vec{g}\left(\vec{\eta}\right) = \begin{bmatrix} \vec{f}_G^{\,b} + \vec{f}_B^{\,b} \\ \vec{r}_B^{\,b} \times \vec{f}_B^{\,b} \end{bmatrix} \,, \tag{1.27}$$

where "$\times$" is the symbol used to represent the operation of cross product.

Making this relationship explicit, the expression of $\vec{g}(\vec{\eta})$ is extracted so that it can be replaced in the equation of motion (1.13):

$$\vec{g}(\vec{\eta}) = \begin{bmatrix} \left(\|\vec{W}\| - \|\vec{B}\|\right) s_\vartheta \\ -\left(\|\vec{W}\| - \|\vec{B}\|\right) c_\vartheta s_\varphi \\ -\left(\|\vec{W}\| - \|\vec{B}\|\right) c_\vartheta c_\varphi \\ y_B^b \|\vec{B}\| c_\vartheta c_\varphi - z_B^b \|\vec{B}\| c_\vartheta s_\varphi \\ -z_B^b \|\vec{B}\| s_\vartheta - x_B^b \|\vec{B}\| c_\vartheta c_\varphi \\ x_B^b \|\vec{B}\| c_\vartheta s_\varphi + y_B^b \|\vec{B}\| s_\vartheta \end{bmatrix}, \tag{1.28}$$

in the body frame $< b >$ (linked to the vehicle).

1.3.4 Modelling of sea current disturbance

The presence of sea currents is an important element, it is necessary to take into account, to be able to get a realistic simulation model of the vehicle. Currents, due to different elements (e.g. wind, heat exchange near the free surface, rotation of the earth) may be a noteworthy problem to navigation of small underwater robots, being such currents characterized by speeds able to reach up to $2 \div 3$ m/s in open sea, against cruising speeds of these robots rarely exceeding $0.4 \div 0.5$ m/s.
To include the effect of forces and torques created by currents in motion equations (1.13), it is assumed they may be written in terms of relative speed $\vec{v_r}$:

$$\vec{v_r} = \vec{v} - \vec{v_c} \ . \tag{1.29}$$

$\vec{v_c} = [u_c, v_c, w_c, 0, 0, 0]^T$ is the current speed vector (expected to be irrotational) expressed in the body frame $< b >$.
Such a vector can be obtained from the decomposition of the current speed in the fixed frame, $< n >$, $\vec{\mathrm{V}}_c = \left[u_c^E, v_c^E, w_c^E\right]^T$ (as shown in Figure 1.4, where "E" indicates *Earth*), through R_n^b (1.3) rotation matrix:

$$\begin{bmatrix} u_c \\ v_c \\ w_c \end{bmatrix} = R_n^b \begin{bmatrix} u_c^E \\ v_c^E \\ w_c^E \end{bmatrix} \ . \tag{1.30}$$

Presuming the current speed is steady or slightly variable

$$\dot{\vec{v}}_c = \vec{0} \ \Rightarrow \ \dot{\vec{v}}_r = \dot{\vec{v}} \ , \tag{1.31}$$

motion equations, indicated in a reference frame moving linked to the current, be-

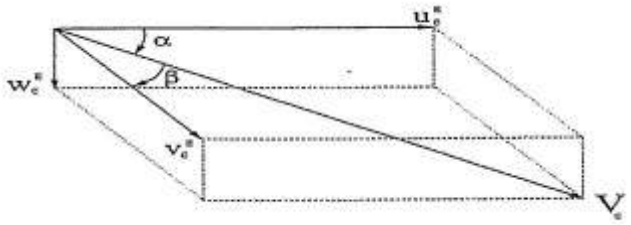

Figure 1.4: Decomposition of the current speed as to x^n, y^n, z^n axes of the NED system

come:

$$M\dot{\vec{v}}_r + C(\vec{v}_r)\vec{v}_r + D(\vec{v}_r)\vec{v}_r + \vec{g}\left(\vec{\eta}\right) = \vec{\tau}\,. \tag{1.32}$$

This way it is possible to introduce in the dynamic model of the vehicle a disturbance simulating an irrotational current with constant speed, in the fixed frame, both in module and in direction.

1.3.5 Propeller positions and hydrodynamic coefficient evaluation

Typhoon AUV is an under-actuated system: the roll degree of freedom cannot be controlled using the actuator configuration. The roll stability is given by positioning the center of mass of the vehicle below its center of buoyancy. On the other hand it is worth to note that the actuation of the yaw degree of freedom is redundant: in fact a desired yaw angle can be reached using the lateral thrusters or the rear propellers. The rear propellers are used for the surge motion and to travel curves during the cruise navigation. Lateral thrusters are used during hovering orientation manoeuvres and to travel curves with a limited radius of curvature. In order to optimize the design of the actuation and control systems a model of the vehicle has been implemented in Matlab-Simulink^{TM} according to [1]. The actuator behaviour, including the reaction forces, has been simulated using the bilinear Blanke model [1]. Hydrodynamic features of the vehicle have been preliminary identified through CFD simulations.

In Figure 1.5 the layout of the six actuators on the real vehicle is shown. The characteristics of the propulsion system and the hardware ones of Typhoon AUV are described in more details in section 1.5.

In Figure 1.6 a schematic representation of the layout of the six actuators is shown; the x-axis is directed along the longitudinal direction of the vehicle, the y-axis is along the lateral direction on the horizontal plane of symmetry of the vehicle, pointing to the right, while the z-axis is defined according to a right-handed frame. S_n indicates the thrust of the n-th propeller, which is directed along its axis. b_1, b_2 and b_3 are the distances of the

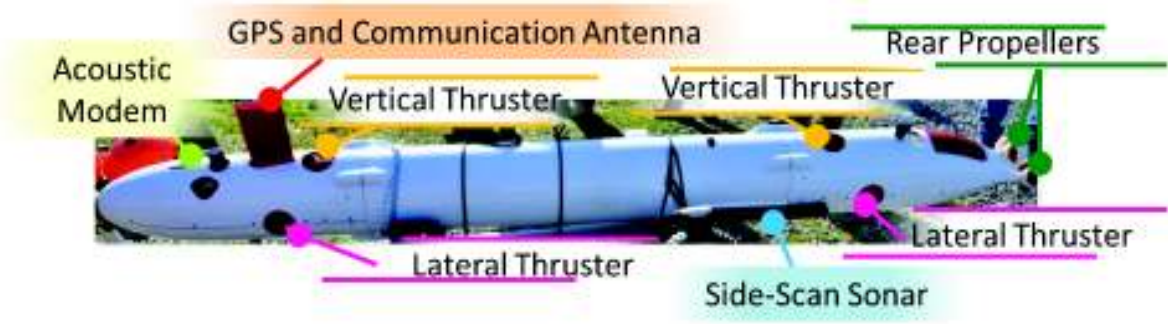

Figure 1.5: Propeller positions

actuators from the center of mass of the vehicle.

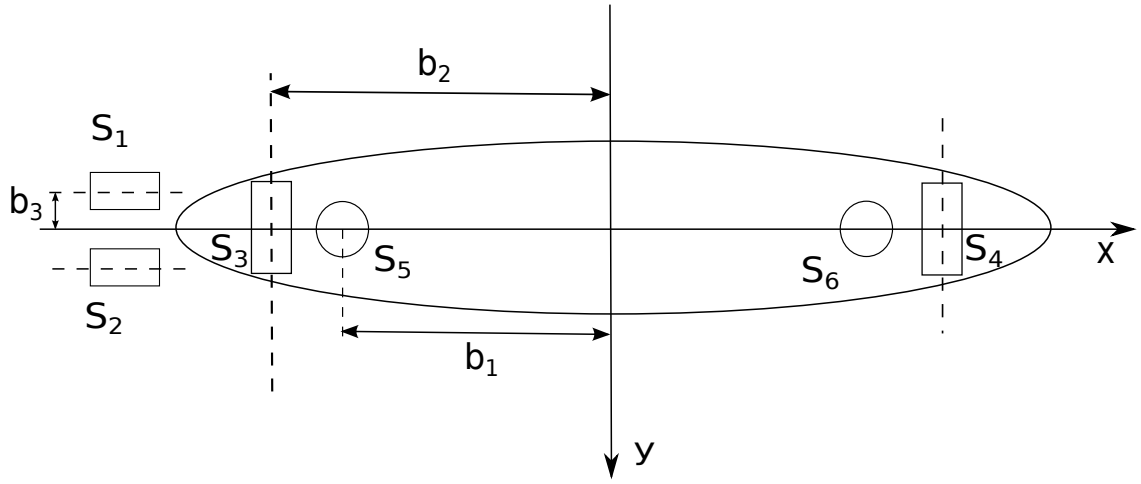

Figure 1.6: Propeller layout scheme

The hydrodynamic forces have a dominant effect in the vehicle motion. Consequently, it is essential to estimate, as realistically as possible, the forces that the fluid exerts on the surface of the body and to find the correct dumping coefficients. Since the forces exerted by the fluid on the surface depend directly on the body shape, geometries sufficiently representative of the real vehicle have been considered. Because of the difficulties in finding reliable data in the case of non-elementary surfaces, the use of a fluid dynamic computation software is necessary; CFD simulations have been carried out and they have allowed to estimate, with good approximation, a series of parameters, including the forces mentioned above. In particular ANSYS CFX software has been used. It is useful to express the forces and moments by dimensionless coefficients, in order to use them in any condition of similarity. The calculated coefficients are 6:

Frontal drag coefficient:

$$C_{Dx} = \frac{F_x}{\frac{1}{2}\rho A_f v^2} \tag{1.33}$$

Lateral and vertical drag coefficients (with the assumption that the body has a cylindrical symmetry they have the same value):

$$C_{Dy} = \frac{F_y}{\frac{1}{2}\rho DLv^2} \qquad C_{Dz} = \frac{F_z}{\frac{1}{2}\rho DLv^2} \tag{1.34}$$

Roll resistance coefficient:

$$C_{Mx} = \frac{M_x}{\frac{1}{2}\rho A_f D^3 \omega^2} \tag{1.35}$$

Pitch and yaw resistance coefficients:

$$C_{Mz} = \frac{M_z}{\frac{1}{2}\rho DL^4 \omega^2} \qquad C_{My} = \frac{M_y}{\frac{1}{2}\rho DL^4 \omega^2} \tag{1.36}$$

where the used symbols are: speed v (scalar value in the considered direction), angular velocity ω (scalar value in the considered direction), frontal area A_f (in the considered direction), diameter D, fluid density ρ, length L.

Frontal drag coefficient

The calculation of the above mentioned frontal drag coefficient C_{Dx}, defined according to (1.33), is has been the main goal of the carried out numerical analysis. This coefficient is linked to the speeds the AUV will be able to reach, the power required to the propellers and consequently the battery consumption too. More tests have been made modifying the vehicle mesh both as typology and numbers of elements. Subsequently the trend of C_{Dx} at different speeds has been estimated.

The utilized domain has the shape of a regular parallelepiped of 4x4x8 m; the analysed vehicle surface is placed in its middle. The fluid is water (unsalted) and has got a speed equal to 2 m/s along the submarine longitudinal axis (the salinity effects are here considered negligible). The fluid pressure is 30 bar, corresponding to the depth of about 300 m.

The combination of the cells defining the fluid domain is called “mesh”. The number of elements influences the accuracy and complexity of calculation: a higher number of cells improves the accuracy but also involves much higher calculation times. It is sometimes necessary to reach a compromise between these two aspects and use useful precautions such as thickening in interested zones, or, where it is possible, using planes of

symmetry.

It is possible to distinguish between:

- Structured mesh: in this case the cells have a hexahedral and are placed in a very regular way. This fact offers some advantages in terms of accuracy, but brings to a greater complexity of construction and an exaggerated number of cells in areas where the structure of flow field does not request an elevated thickening;

- Non-structured mesh: in this typology the domain is filled with elements of variable dimension (for instance tetrahedrons). Near the wall, on the contrary, to solve in a fair way the boundary layer, are created some layers of prisms (in this case they are called non-hybrid structured meshes). The first advantage is the simplicity of construction: generally speaking, the construction of a non-structured mesh requires much shorter time compared to a structured one. Another advantage lies in its flexibility: cells can be thickened at will in the areas of interest.

5 different types of mesh have been considered: 2 non-structured and 3 structured with number of elements among 1.2 and 2.5 million.
The CFD analysis allows to obtain the evolution of the fluid variables (pressure, speed, etc.) that characterize the phenomenon in each cell of the calculation domain. Figure 1.7 returns the speed value in one of the planes of symmetry.

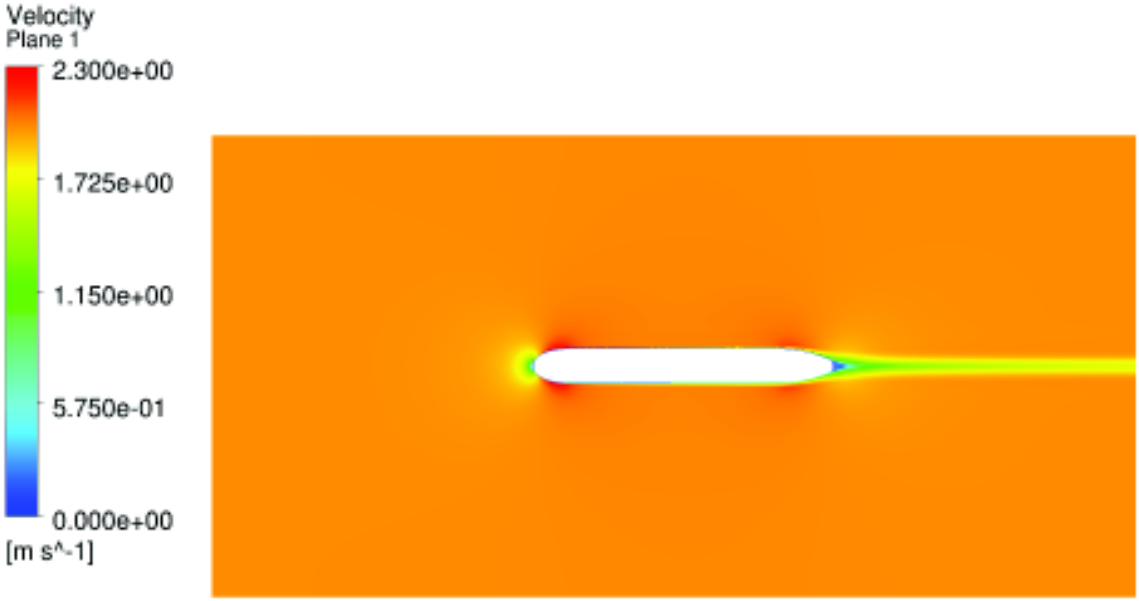

Figure 1.7: Lateral view of the flow field during the calculation for C_{Dx}

For each mesh the computation of the frontal drag coefficient has been carried out. In Table 1.1 the results of some of the simulations are shown. It may be noted that the

contribution related to the shape is significantly lower than the one related to friction: this is due to the rather hydrodynamic form of the geometry that gives precedence to the shear stresses on those due to the pressure distribution.

Mesh	Geom	F_{tot} (N)	$F_{friction}$ (N)	F_{shape} (N)	C_{Dx}	$C_{Dxfriction}$	$C_{Dxshape}$
1	1	18.37	15.14	3.51	0.1320	0.1071	0.0248
2	1	17.90	14.92	2.98	0.1267	0.1055	0.0210
3	1	18.23	15.00	3.23	0.1290	0.1062	0.0228
4	1	18.06	14.96	3.10	0.1278	0.1059	0.0219
5	2	16.39	13.42	2.97	0.1160	0.0950	0.0210

Table 1.1: Frontal drag coefficient

It is worth to note that the calculated coefficients are not constant but vary according to the flow conditions which the body is subject to. It is therefore studied the influence of the forward speed on the coefficient under consideration. In this case it is very useful to analyse the dependence on the Reynolds number defined as*

$$Re = \frac{\rho D v}{\mu} \tag{1.37}$$

where ρ is the density of the flow and μ its dynamic viscosity. The achieved results are shown in Table 1.2.

Speed (m/s)	F_{tot} (N)	$F_{friction}$ (N)	F_{shape} (N)	C_{Dx}	$C_{Dxfriction}$	$C_{Dxshape}$	Re
1	5.055	4.211	0.844	0.1431	0.1192	0.0239	$3 \cdot 10^6$
2	18.06	14.96	3.10	0.1278	0.1059	0.0219	$6 \cdot 10^6$
3	38.22	31.56	6.66	0.1202	0.0993	0.0209	$9 \cdot 10^6$
5	98.48	81.06	17.42	0.1115	0.0918	0.0197	$2.5 \cdot 10^7$

Table 1.2: Advancing speed influence

In Figure 1.8 the advance resistance coefficient as a function of Reynolds number is reported. It is worth to note how such a coefficient decreases when Reynolds number increases, according to what happens in literature for simpler cases (such as a cylinder). It is important to observe that the dependence from the advancing speed has been neglected in the dynamic model, where a steady value of the coefficient C_{Dx} has been assumed.

*Generally drag coefficients are expressed in terms of dimensionless numbers that the "Similarity theory" identifies to be the variables that regulate the phenomenon, including the Reynolds number.

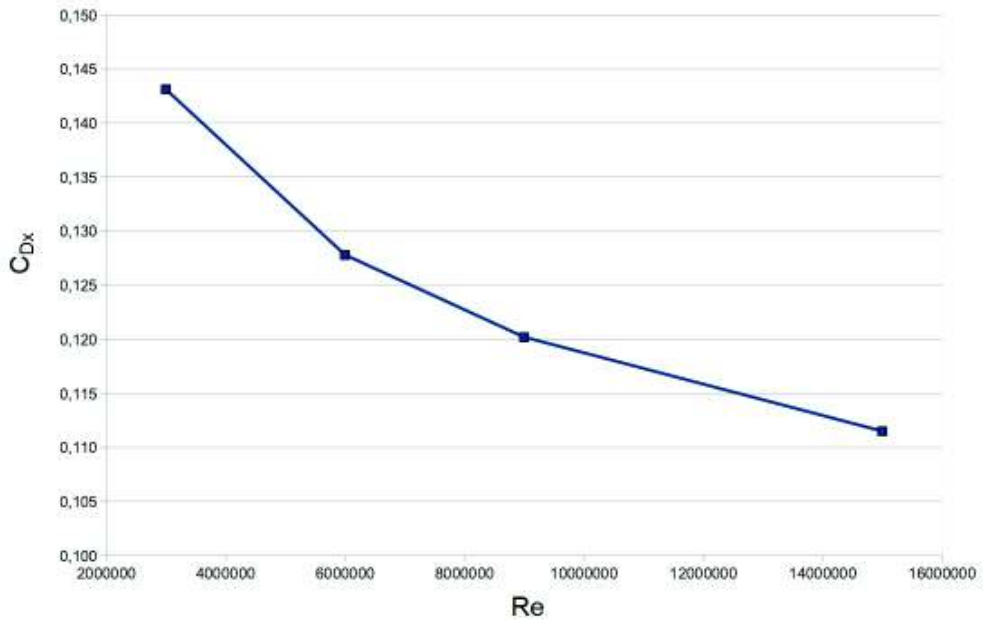

Figure 1.8: C_{Dx} as a function of the Reynolds number

Lateral and vertical drag coefficients

The study of these parameters is not fundamental, as this type of motions are not a top priority; for the completeness of the model the values of these two quantities have been estimated too. Considering the "almost" cylindrical geometry of the hull, it has been decided to estimate just one of the two coefficients (C_{Dy}), approximating the other (C_{Dz}) to the same value.

In Table 1.3 force and coefficient values (friction and shape) for side displacement simulations are displayed.

F_{tot} (N)	$F_{friction}$ (N)	F_{shape} (N)	C_{Dy}	$C_{Dyfriction}$	$C_{Dyshape}$
50.80	1.08	49.82	0.506	0.0108	0.496

Table 1.3: Drag coefficients for side displacements

In Figure 1.9 the speed field for the lateral displacement is shown.

Roll resistance coefficient

As it has been previously mentioned, roll is an "undesired" motion. If it is too high it may be harmful for the control, as there are not active ways to reduce it on Typhoon. The roll motion is decreased locating the center of mass of the vehicle under the center of buoyancy; this allows to have a greater stability and not to capsize the unit, but the only

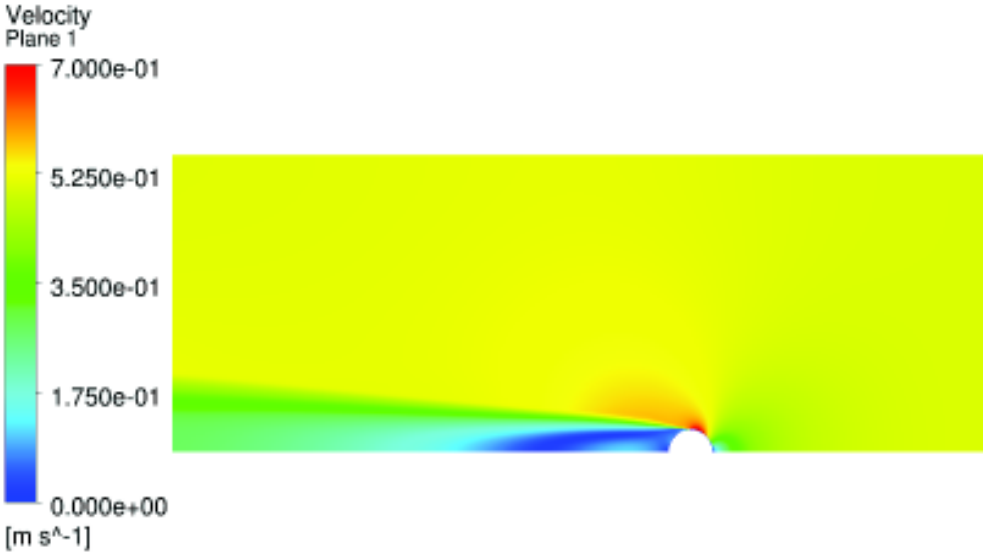

Figure 1.9: Speed field for the lateral displacement

component damping down this motion is the hydrodynamic resistance (roll resistance coefficient C_{Mx}). The higher this coefficient is the better the roll motion will consequently be. Two tests have been carried out, where in one case some stabilizers have been added. In this case the fluid in the domain has not a linear speed but, it is rotated (rolled) at a speed of 5 degrees per second. In Table 1.4 and Figure 1.10 the comparison between the two tests is shown: it is possible to observe that in the second situation the roll resistance coefficient results bigger of an order of magnitude.

Test	Torque (Nm)	C_{Mx}
Without stabilizers	$4.609 \cdot 10^{-4}$	0.0638
With stabilizers	$5.298 \cdot 10^{-3}$	0.734

Table 1.4: Roll resistance coefficient

Pitch and yaw resistance coefficients

Also in this case it is possible to consider the almost cylindrical geometry of the vehicle and thus perform just one test for both the coefficients (C_{My} and C_{Mz}). The fluid is rotated at a speed of 5 degrees per second. The following simulation results have been achieved (Figure 1.11):
$M_y = 1.5$ Nm
$C_{My} = 0.0253$

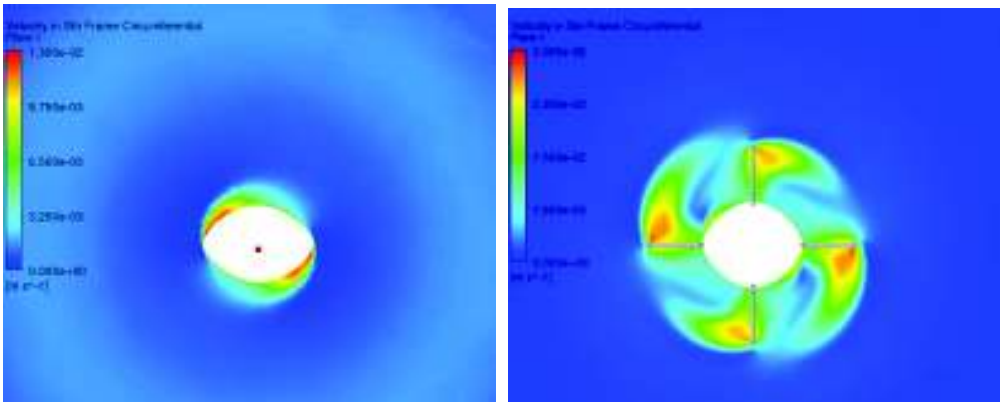

(a) Without stabilizers (b) With stabilizers

Figure 1.10: Comparison between the roll motion fields

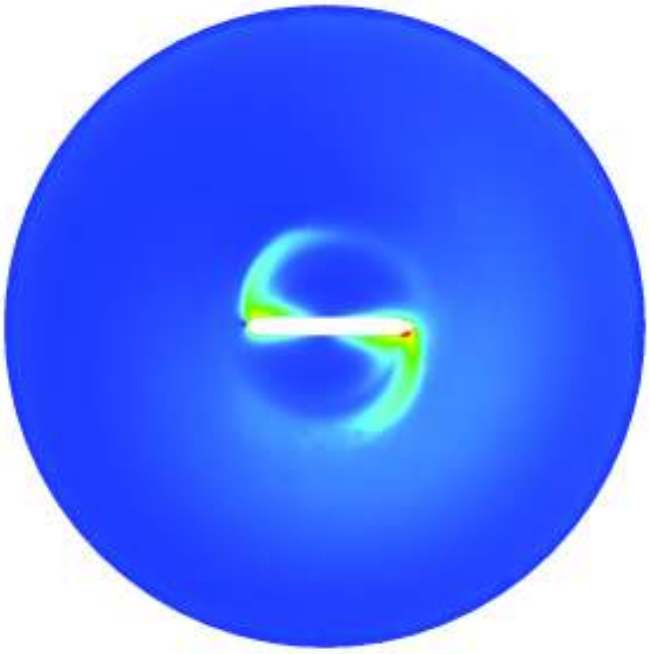

Figure 1.11: Speed field for pitch/yaw motions

1.4 Navigation control

The motion control is based on a PF (Path Following) strategy [11] that involves the separate construction of the geometric path and the dynamic assignment, emphasizing spatial localization as a primary task objective, while considering the dynamic aspect to be of minor importance, expendable if necessary. This clearly represents a more flexible and robust alternative than the TT (Trajectory Tracking) scheme that entails the simultaneous construction of the geometric path and the dynamic behaviour. The feedback for the controller can be generated by a pose estimation algorithm which is based on the information coming from a sensor layout composed of a DVL (Doppler Velocity Log), an IMU (Inertial Measurement Unit), a magnetometer, a pressure sensor (depth measurement) and an USBL system providing a position measurement with respect to a support surface vehicle whose position is measurable by means of the GPS (Global Positioning System).

The desired trajectory generation and the development of a control system that permits to the vehicle to follow it are problems that can be faced in some different ways. The chosen way mainly depends on the mission the vehicle has to perform and on the conditions that have to be complied with. Two different approaches, related to two different kinds of missions, have been investigated:

- Waypoint navigation: the desired trajectory is a broken line connecting the points (*waypoints*) where the vehicle stops to change its orientation. This type of motion is suitable for underwater exploration in which low speeds, high stability and positioning accuracy are required (e.g. a detailed optical inspection of a site);
- Path following navigation: this control strategy considers the spatial localization as the main target, while the vehicle dynamic behaviour as a secondary, and sacrificable if necessary, one. In the *path following* navigation, the chosen reference trajectories are constituted by straight sections and constant radius curves, on which a constant travelling speed is defined. This type of navigation is designed for a mission that requires long travelling distances at a higher speed, with a saving of power.

1.4.1 Waypoint navigation

This type of control is designed for the exploration phases, in which sensors have to, for example, collect images or make recognitions: for these operations the positions and the desired speeds must be obtained with accuracy at every moment.

Trajectory planning

In order to achieve a specific task by any autonomous system, it is necessary to consider the characteristics of the trajectory planning algorithms. The purpose of the trajectory planning is to generate reference inputs to the motion control system: the controller will ensure the execution of the planned trajectories. Usually, the user specifies a number of parameters to characterize the desired trajectory; the goal of the trajectory planning consists in generating a temporal sequence of values of an interpolating function (generally polynomial). Generally, as a minimum requirement, an autonomous system needs to move from an initial pose to a final one. The transition must be characterized by motion laws that require actuators to carry out forces which respect the constraint set of amplitude and do not excite resonant modes (frequently not modelled). It can be assumed that a path planning algorithm should have the points of the path, the path constraints, the constraints due to the system dynamics (in this case the vehicle) as inputs, and the trajectory of the vehicle itself as output, expressed as a time sequence of values, given in general by pose, speed and acceleration. In this section a simple point to point motion is adopted, by fixing only the extreme points of the path and the time of the transition.

In the waypoint navigation the vehicle must move from an initial configuration to a final one within a given time interval t_f. The particular path followed in this case is not of interest. The chosen approach presents polynomial mixed type time laws, as it is frequently used in the industrial practice; it allows to check immediately if speed and acceleration imposed by those laws of motion are coherent with the physical system. A trapezoidal speed profile is assigned; it imposes a constant acceleration in the starting phase, a constant cruise speed and a constant deceleration in the phase of arrival. The trajectory that follows is made up (in time) from a linear section connected by two parabolic sections in the neighbourhood of the start and end position.

As it can be seen from the profiles in Figure 1.12 the initial and final speeds are equal to zero and the sections with constant acceleration have equal durations, i.e. equal amplitude in the two sections. These choices imply the symmetry of the trajectory with respect to the midpoint $q_m = (q_f - q_i)/2$ and the average time $t_m = t_f/2$.

The trajectory must satisfy some constraints to ensure that the transition from q_i to q_f takes place in the defined time t_f. The speed at the end of the parabolic section must equal the constant speed of the linear one [15]:

$$\ddot{q}_c t_c = \frac{q_m - q_c}{t_m - t_c} \tag{1.38}$$

where q_c is the value assumed by the variable at the end of the parabolic section reached

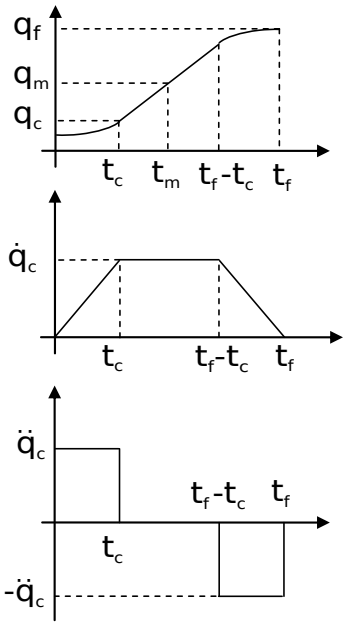

Figure 1.12: Position, speed and acceleration profiles

in time t_c with constant acceleration $\ddot{q}_c$. It has, therefore,

$$q_c = q_i + \frac{1}{2}\ddot{q}_c t_c^2 \tag{1.39}$$

$$\ddot{q}_c t_c^2 - \ddot{q}_c t_c t_f + q_f - q_i = 0 \tag{1.40}$$

Usually $\ddot{q}_c$ is assigned with the constraint $sgn(\ddot{q}_c) = sgn(q_f - q_i)$; thus, known t_f, q_i and q_f:

$$t_c = \frac{t_f}{2} - \frac{1}{2}\sqrt{\frac{t_f^2\ddot{q}_c - 4(q_f - q_i)}{\ddot{q}_c}} \tag{1.41}$$

from which the solution is obtained imposing $t_c \leq t_f/2$.

The acceleration is therefore subject to the constraint:

$$|\ddot{q}_c| \geq \frac{4|q_f - q_i|}{t_f^2} \tag{1.42}$$

when $\ddot{q}_c$ is chosen to meet the (1.42) with the equality sign, the trajectory does not exhibit the section with constant speed, but only sections of acceleration and deceleration (triangular velocity profile). Assigned q_i, q_f, t_f and an average speed of transition, (1.42) allows to impose an acceleration consistent with the desired trajectory; then getting t_c from (1.41) it is possible to compose the polynomial functions in sequence:

$$q(t)=\begin{cases} q_i+\frac{1}{2}\ddot{q}_c t^2 & \text{per } 0\le t\le t_c \\ q_i+\ddot{q}_c t_c(t-t_c/2) & \text{per } t_c\le t\le t_f-t_c \\ q_f-\frac{1}{2}\ddot{q}_c(t_f-t)^2 & \text{per } t_f-t_c\le t\le t_f \end{cases} \tag{1.43}$$

Lay down the acceleration in the parabolic section is not the only way to build trajectories with trapezoidal velocity profile. In addition to q_i, q_f, t_f, the cruising speed $\dot{q}_c$ can be defined, which is subject to the constraint:

$$\frac{|q_f-q_i|}{t_f}<|\dot{q}_c|\le\frac{2|q_f-q_i|}{t_f} \tag{1.44}$$

and given that $\dot{q}_c=\ddot{q}_c t_c$, through (1.40) t_c can be calculated, which is equal to:

$$t_c=\frac{q_i-q_f+\dot{q}_c t_c}{\dot{q}_c} \tag{1.45}$$

which allows to obtain the value of the acceleration,

$$\ddot{q}_c=\frac{\dot{q}_c^2}{q_i-q_f+\dot{q}_c t_c} \tag{1.46}$$

t_c and $\ddot{q}_c$ values allow to generate the above-outlined polynomial law sequence.

1.4.2 PID control with gravity compensation

Broadly speaking, the control problem is to determine the trend of the forces that the actuators must apply to ensure the fulfilment of the specifics and the execution of the desired operations. In the control of underwater vehicles, the complexity of the dynamics of motion has a massive influence on the performance of the control system. In this case it is appropriate to synthesize control algorithms that rely on a more detailed understanding of the model, i.e., it refers to a centralized control based on knowledge, partial or complete, of the laws ruling the motion of the vehicle. First the characteristics of a simple PID controller (*Proportional Integrative Derivative*) for a generic system are introduced: a generic system P(s) is considered to be controlled through a controller block C(s), as shown in Figure 1.13.

The transfer function of a PID controller is generally given by the following form:

$$C_{PID}(s)=K_P+\frac{K_I}{s}+K_D s=\frac{K_D s^2+K_P s+K_I}{s} \tag{1.47}$$

The variable $\vec{e}_r$ in Figure 1.13 is the error between the desired output and the true output of the system; this signal is the input of the PID controller, which generates an

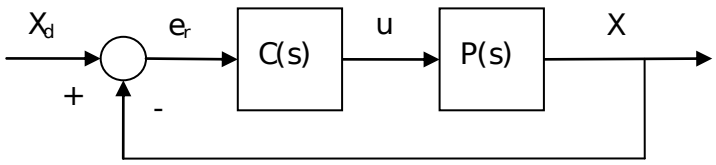

Figure 1.13: Feedback control scheme

output signal $\vec{u}$ made up of three components, proportional, integral and derivative:

$$\vec{u} = K_P \vec{e}_r + K_D \dot{\vec{e}}_r + K_I \int_0^t \vec{e}_r(T) dT \tag{1.48}$$

The proportional term has the effect of improving the readiness of the response and reducing, but not eliminating, the steady-state error; the integral part deleting steady-state error, but the transient response runs worse; the derivative action has instead the effect of increasing the stability of the system by improving the transient response.

Most of the AUVs use a series of PID type-SISO controllers where each controller is designed to manage a single degree of freedom of the vehicle [1]. This consideration implies that the matrices K_P, K_D e K_I, of the PID control law:

$$\vec{\tau}_{PID} = K_P \vec{e}_r(t) + K_D \dot{\vec{e}}_r(t) + K_I \int_0^t \vec{e}_r(T) dT \tag{1.49}$$

can be chosen diagonal and have to be positive-defined. Also in this case the variable $\vec{e}_r = \vec{\eta}_d - \vec{\eta}$ defines the error in the path. A standard PID control can be improved, as mentioned above, by the knowledge, even partial, of the dynamic model of the vehicle: in this case the gravity compensation is used. Its contribution is zero under conditions of static stability. In agreement with that, vector $\vec{\tau}_{PID}$ will change as follows:

$$\vec{\tau}_v = (J_b^n)^\top \vec{\tau}_{PID} + \vec{g}_{RB}(\eta) \tag{1.50}$$

this vector is then converted to rotational reference speed of the propellers.

1.4.3 Path following navigation

Waypoint navigation is very efficient for exploration missions, for which, e.g., moving with extreme precision can be necessary for sonar scans. Waypoint navigation, as defined in Subsection 1.4.1, is however characterized by some drawbacks; the main one

is the stopping and restarting at each waypoint that implies waste of time and energy. Therefore, it is convenient to define a different navigation strategy to be used when the waypoint navigation is not necessary. For this control strategy, of *path following* type, the main objective is to maintain the vehicle on a desired path, characterized by the continuity of the tangent in all its points [11]. A time law is not assigned, but a reference travelling speed is defined. The geometrical reference is the priority, whereas the dynamic reference is sacrificed if necessary to stay on the path.

Trajectory planning and motion control

In the path following control strategy, the only theoretical constraint to the generation of a continuous path is the continuity of its tangency. Considering a real vehicle with an own inertia and limitations on the propeller thrusts, a further constraint must be introduced: a minimum radius of curvature depending on the velocity that has to be maintained. The aim is therefore to find an optimal trajectory for the set purpose, i.e., the achievement of several points of interest without ever stopping and respecting the constraints. A line starting from the points allocated in the space has been generated: in particular linking these points with a broken line and connecting the "corners" with arcs of circumference. The resulting trajectory is a succession of straight lines and circular curves. Introducing the simplifying assumption of maintaining a constant speed along the whole trajectory, also the radius ρ of each arc of circumference will have to be constant.

The algorithm that generates the path is initialized with a matrix U containing the N coordinates of the points where the vehicle has to curve:

$$U = \begin{bmatrix} P_1 & P_2 & \dots & P_i & \dots & P_N \end{bmatrix} \qquad \text{where } P_i = \begin{bmatrix} x_i \\ y_i \\ z_i \end{bmatrix} \tag{1.51}$$

and should generate, in function of a scalar variable π that indicates the distance travelled on the trajectory, the location of each point of the trajectory on the inertial frame (identified by π), and a set of unit vectors: $\vec{T}$ tangent to the trajectory, $\vec{H}$ perpendicular to the vertical plane passing through $\vec{T}$, and $\vec{R}$ to complete the right-handed frame. To obtain these components it is necessary to parametrize the straight lines and circles with respect to a reference frame, which is identified through the unit vectors $\vec{i}$, $\vec{j}$ and $\vec{k}$ [15]. Since the path is based on N points, it is convenient to divide the trajectory in $N-1$ sections, each composed of a straight portion and the next turn (except for the last straight part). In Figure 1.14 a schematic illustration of the procedure is shown.

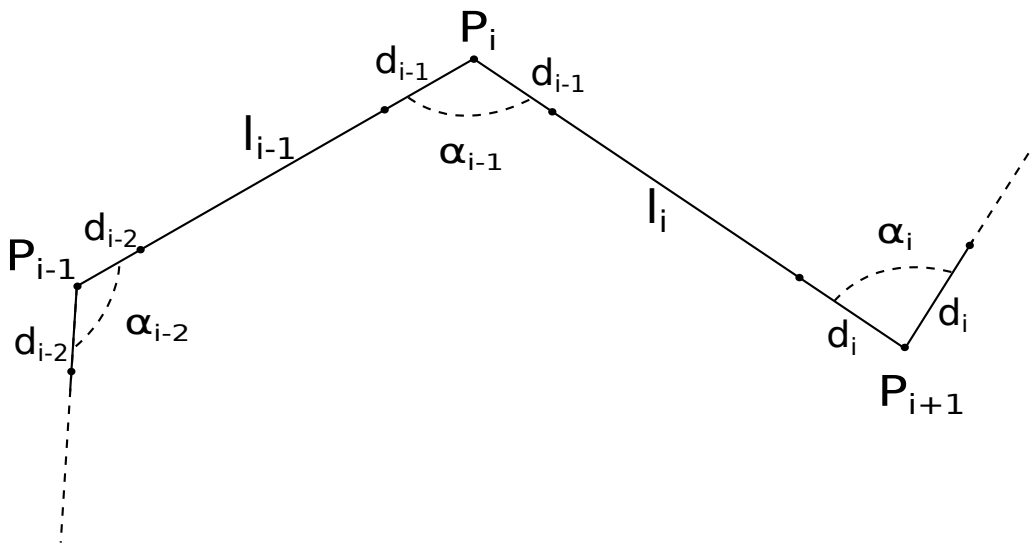

Figure 1.14: Simple scheme of the generation of the trajectory

First, the distance between two consecutive points is defined:

$$l_i = ||P_{i+1} - P_i|| \tag{1.52}$$

the first part of the section i will be straight, starting at the end of the previous curve and ending at the beginning of the next curve; the start and end points of the straight are calculated. To do this it is necessary to calculate the scalars d_{i-1} and d_i representing the distances from the corresponding point (in the first case P_{i-1}) at the beginning/end of the straight section, defined to ensure the continuity of the tangency. These values are functions of the angles α_i formed at the intersection of two straight sections:

$$\begin{aligned} \alpha_{i-1} &= \arccos\left(\frac{(P_i - P_{i-1})^\top (P_{i+1} - P_i)}{||P_i - P_{i-1}||||P_{i+1} - P_i||}\right) \\ \alpha_i &= \arccos\left(\frac{(P_{i+1} - P_i)^\top (P_{i+2} - P_{i+1})}{||P_{i+1} - P_i||||P_{i+2} - P_{i+1}||}\right) \end{aligned} \tag{1.53}$$

The two distances can be defined as:

$$d_{i-1} = \tan\left(\frac{\alpha_{i-1}}{2}\right)\rho \qquad\qquad d_i = \tan\left(\frac{\alpha_i}{2}\right)\rho \tag{1.54}$$

Initial position P_i^I and final P_i^F of the straight will be:

$$\begin{aligned} P_i^I &= P_i + (P_{i+1} - P_i)\frac{d_{i-1}}{l_i} \\ P_i^F &= P_i + (P_{i+1} - P_i)\left(1 - \frac{d_i}{l_i}\right) \end{aligned} \tag{1.55}$$

Now the segment can be parametrized as a function of π:

$$P(\pi) = P_i^I + \pi \frac{P_i^F - P_i^I}{l_i - d_i - d_{i-1}} \tag{1.56}$$

The three unit vectors, constant throughout the straight, can be written as:

$$\begin{aligned} \vec{T} &= \frac{P_{i+1} - P_i}{||P_{i+1} - P_i||} \\ \vec{H} &= -\frac{\vec{T} \wedge \vec{k}}{||\vec{T} \wedge \vec{k}||} \\ \vec{R} &= \vec{T} \wedge \vec{H} \end{aligned} \tag{1.57}$$

The second part of the stroke i consists in an arc of circumference in three dimensions, which has P_i^F as its starting point and P_{i+1}^I as the end point. The length r of the arc is given, by construction, by:

$$r = \alpha_i \rho \tag{1.58}$$

For the parametric description of the arc it is convenient to use a new reference frame $(\vec{i}', \vec{j}', \vec{k}')$ (Figure 1.15): the unit vector $\vec{k}'$ will be normal to the plane of the curve, the unit vector $\vec{i}'$ will be directed along the line between the circumference center C_i and P_i^F, the unit vector $\vec{j}'$ consequently. The description of these unit vectors on the inertial frame is:

$$\begin{aligned} \vec{k}' &= \frac{(P_{i+1} - P_i) \wedge (P_{i+2} - P_{i+1})}{||(P_{i+1} - P_i) \wedge (P_{i+2} - P_{i+1})||} \\ \vec{i}' &= -\vec{k}' \wedge \frac{P_{i+1} - P_i}{||P_{i+1} - P_i||} \\ \vec{j}' &= \vec{k}' \wedge \vec{i}' \end{aligned} \tag{1.59}$$

The rotation matrix between the inertial frame and the new frame will be then:

$$R_c^n = \begin{bmatrix} \vec{i}' & \vec{j}' & \vec{k}' \end{bmatrix} \tag{1.60}$$

The origin of the new frame will be just next to the center of circumference C_i:

$$C_i - O^n = (P_i^F - O^n) - \rho\, \vec{i}' \tag{1.61}$$

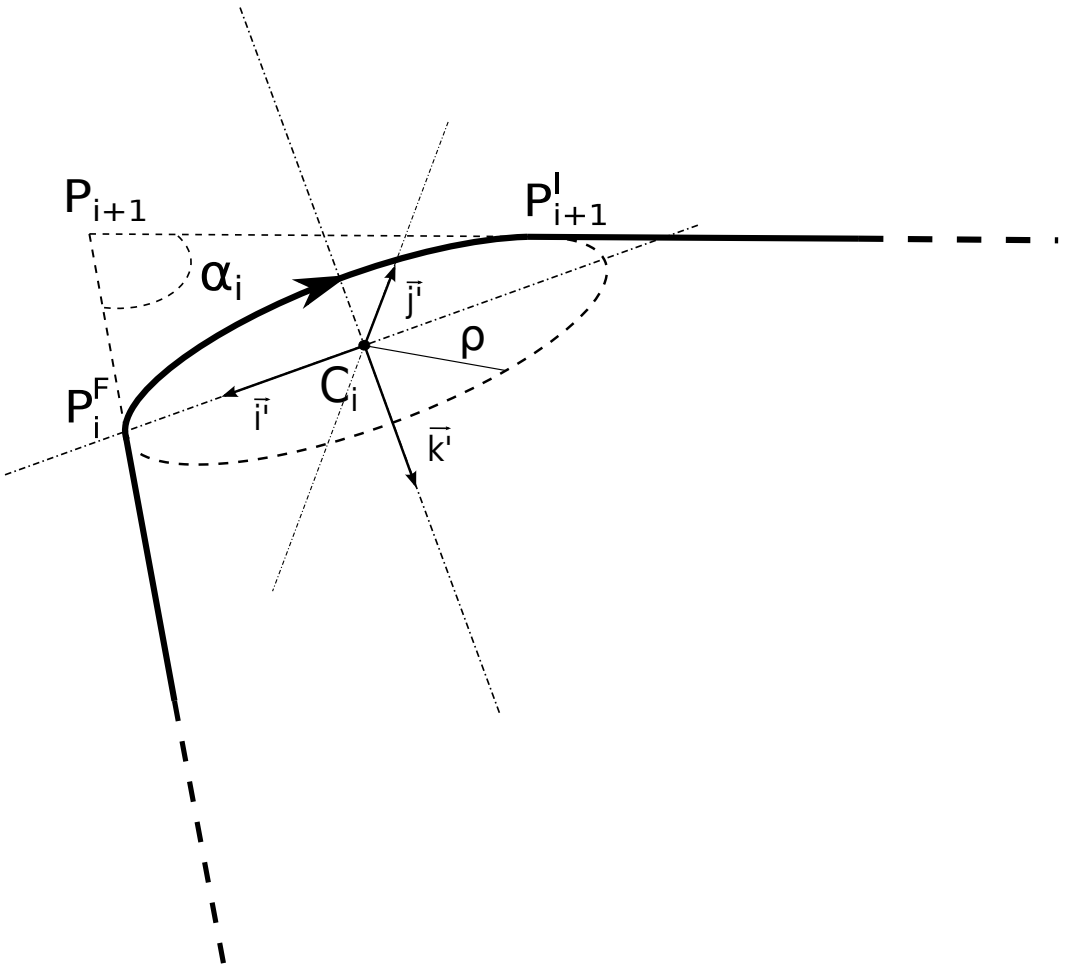

Figure 1.15: Tridimensional curve representation

where $O^n = \begin{bmatrix} 0 & 0 & 0 \end{bmatrix}^\top$ is the origin of the inertial frame. With the new reference frame it is simple to parametrize the curve as a function of the curvilinear abscissa π

$$P^c(\pi) = \rho \begin{bmatrix} \cos\left(\frac{\pi}{\rho}\right) \\ \sin\left(\frac{\pi}{\rho}\right) \\ 0 \end{bmatrix} \tag{1.62}$$

and then get back into a fixed coordinate system:

$$P(\pi) = C_i + R_c^n P^c(\pi) \tag{1.63}$$

At this point the unit vectors $\vec{T}$, $\vec{H}$, e $\vec{R}$ are calculated:

$$\begin{aligned} \vec{T}(\pi) &= R_c^n \begin{bmatrix} -\sin\left(\frac{\pi}{\rho}\right) & \cos\left(\frac{\pi}{\rho}\right) & 0 \end{bmatrix}^\top \\ \vec{H}(\pi) &= -\frac{\vec{T}(\pi) \wedge \vec{k}}{\|\vec{T}(\pi) \wedge \vec{k}\|} \\ \vec{R}(\pi) &= \vec{T}(\pi) \wedge \vec{H}(\pi) \end{aligned} \tag{1.64}$$

As previously said, for this control strategy the main objective is to maintain the vehicle on a desired path, characterized by the continuity of the tangent in all its points. A time law is not defined, but a reference travelling speed is assumed. The geometrical reference is the priority, whereas the dynamic reference is sacrificed if necessary to stay on the path. For reasons of brevity, the motion control strategy for path following navigation is not described here as all its details can be found in [11]: in this paper is also highlighted the suitability of this approach for under-actuated vehicles.

1.4.4 Sensors for underwater navigation

The complete or partial knowledge of the state of the dynamic system is mandatory for a closed-loop control system. In the software simulation the outputs of the dynamic model can be used (to have the desired feedback), but in the real dynamic system its state is not directly known. In practice, to have a good feedback the system has to be equipped with suitable sensors measuring part or the whole state of the dynamic system (e.g. the underwater vehicle, in this case). Unfortunately the sensors are not ideal, i.e. their measurements are affected by noise and errors. Generally speaking, expensive sensors have better accuracy, but it is important to have a reasonable trade-off between costs and performances: e.g. redundant measurements, sensor fusion techniques and good estimation algorithm can improve the feedback of the dynamic state, needed by the controller.

Different type of sensors are usually used for underwater navigation. In this section, the navigation sensors mounted on Typhoon are described: the sensors provide the inputs (measurements) exploited by the estimation algorithm (explained in the following). The sensor behaviours have been modelled, to achieve realistic results in simulation (results that preceded the experimental campaign at sea).

IMU

An Inertial Measurement Unit (IMU) is a device composed of a 3D accelerometer, and a 3D gyroscope. It provides a measure of the acceleration $\vec{f}^b = \begin{bmatrix} f_x^b & f_y^b & f_z^b \end{bmatrix}^\top$ and of the angular velocity $\vec{v}_2 = \begin{bmatrix} p & q & r \end{bmatrix}^\top$ of the vehicle, in the body reference frame. The accelerometer is sensitive to all the external forces acting on it, thus including both gravity and the centrifugal forces. The outputs of the IMU, typically working between 10Hz and 100Hz, can be used to calculate the position, the speed and the orientation of the vehicle, through Inertial Navigation Systems (INS) algorithms.

The main causes of errors for accelerometers and gyroscopes are: sensor noise, not constant scale factor between input and output, the non-perfect orthogonality among the sensor axes which involves a coupling factor between the three components of the measured quantity, the bias that is an offset output even in conditions of zero input [18]. The measurement equations of accelerometers and gyros can be written as:

$$\tilde{\vec{f}} = \vec{f} + \vec{e}_a = \vec{f} + \vec{b}_a + S_a\vec{f} + m_a\vec{f} + \vec{n}_a \tag{1.65}$$

$$\tilde{\vec{v}}_{2_{gyro}} = \vec{v}_2 + \vec{e}_g = \vec{v}_2 + \vec{b}_g + S_g\vec{v}_2 + m_g\vec{v}_2 + \vec{n}_g \tag{1.66}$$

where $\sim$ is the value measured by the sensor, subscript "a" indicates the errors related to the accelerometer and "g" the ones related to the gyroscope. As regards the rest of the adopted notation:

- $\vec{f}$ is the specific force (accelerometer output);
- $\vec{v}_2$ represents the angular speed;
- $\vec{b}$ is the sensor bias;
- S is the scale factor;
- m represents the error due to the non-perfect orthogonality among the sensor axes;
- $\vec{n}$ is the sensor noise, generally modelled as white noise with zero mean.

The bias is a deterministic source of error and generally consists of two parts: one constant part and a one tending to drift.

The integration of the signals provided by accelerometers and gyroscopes introduce errors on the position and on the speed unacceptable and increasing with time, according to the following relations:

Error linked to the gyro	Error linked to the accelerometer
$\delta\vec{v} = \frac{1}{2}\vec{e}_g t^2$	$\delta\vec{v} = \vec{e}_a t$
$\delta\vec{p} = \frac{1}{6}\vec{e}_g t^3$	$\delta\vec{p} = \frac{1}{2}\vec{e}_a t^2$

(1.67)

where $\delta\vec{v}$ and $\delta\vec{p}$ respectively represent the speed and position errors.

Magnetometer

A magnetometer is a device able to measure the modulus and the direction of the magnetic field in correspondence of its position and, in the absence of local magnetic phenomena, provides a measure of the Earth's magnetic field [19]. A 3D magnetometer $\vec{M}^b = [m_x^b, m_y^b, m_z^b]$ can be used to reset the drift of the orientation estimation (Roll, Pitch and Yaw angles). Different systematic errors can affect the measurement of this sensor according to:

$$\tilde{\vec{M}} = C_m C_{sf} C_{si} (\vec{M} + \delta\vec{M}) \tag{1.68}$$

where $\sim$ is the value measured by the sensor and:

- $\vec{M}$ represents the magnetic field;
- $\delta\vec{M}$ is the error due to the Hard Iron;
- C_{si} is the error due to the Soft Iron;
- C_{sf} is the scale factor;
- C_m is linked to the error of a non-perfect sensor alignment.

With "Hard Iron" are indicated the undesired magnetic fields in the proximity of the sensor, generally generated by ferromagnetic materials with permanent magnetic fields. The magnitude and direction of this kind of disturbance remains constant for each orientation of the sensor, thus it can be removed in a calibration phase.

With "Soft Iron" are instead indicated the distortions due to the interaction of the Earth's magnetic field with ferrous objects located in the proximity of the sensor. The magnetic field generated by these magnetic materials can be variable, as it depends on both the modulus and the direction of the external magnetic field.

Pressure sensors for depth measuring

The vehicle depth is calculated from a direct measurement of pressure through standard hydrostatic equations [20]. This sensor can be modelled according to [17]:

$$\tilde{z}_{prof} = z + b_z + n_z \tag{1.69}$$

where

- z is the real depth;
- b_z is the sensor bias;
- n_z is the sensor noise, typically modelled as white noise with zero mean.

Doppler Velocity Log

A Doppler Velocity Log (DVL) is an expensive sensor able to measure the linear speed of the vehicle in the body frame. The measure can be rotated on-line through the rotation matrix between the body frame and the fixed frame.

The actual speed measurements [17] can be modelled according to:

$$\tilde{\vec{v}}_{1_{DVL}} = \vec{v}_1 + \vec{b}_v + \vec{n}_v \tag{1.70}$$

where

- $\vec{v}_1$ is the actual speed expressed in the body frame;
- $\vec{b}_v$ is the sensor bias;
- $\vec{n}_v$ is the sensor noise, typically modelled as white noise with zero mean.

When the DVL is not able to receive the signal reflected from the bottom and only the relative velocity of the water is measured, the measurement is disturbed by underwater currents. In this case, the instrument must be used in conjunction to a real-time estimator of the current.

USBL

The Ultra-Short BaseLine (USBL) is a method of underwater acoustic localization based on the use of an acoustic transceiver (composed of a series of transducers) capable of communicating with a transponder. The adopted configuration in the THESAURUS project

is that the transceiver (USBL) is located on a surface support vehicle (e.g. one of the Typhoon vehicles or a support ship). The transponder is instead an acoustic modem rigidly mounted on board of one of the AUVs navigating underwater.

The working principle is based on the transmission of an acoustic message, containing the time of sending by the transponder, that is received from the USBL head. By the measurement of time of flight the distance between the two vehicles can be evaluated. The position of the underwater AUV, with respect to a reference frame located in the USBL head, can be calculated on the basis of the phase difference the acoustic signal reaches the various transducers (*differencing phase*).

The output signal provided by the sensor is composed of 3 parts: the distance R between the transceiver and the transponder, the relative angle ϕ on the horizontal plane and the relative angle θ on the vertical plane. These three measures define a spherical coordinate system; to obtain the position in Cartesian coordinates the following transformation can be used:

$$\vec{\eta} = \begin{bmatrix} R\sin\theta\cos\phi \\ R\sin\theta\sin\phi \\ R\cos\theta \end{bmatrix} \tag{1.71}$$

Defining e_R, e_ϕ and e_θ as the errors of the related measurements, it is possible to express an actual USBL output according to:

$$\vec{\eta}_{USBL} = \begin{bmatrix} (R+e_R)\sin(\theta+e_\theta)\cos\left(\phi+e_\phi\right) \\ (R+e_R)\sin(\theta+e_\theta)\sin\left(\phi+e_\phi\right) \\ (R+e_R)\cos(\theta+e_\theta) \end{bmatrix} \tag{1.72}$$

It is worth to note that the position error (in the Cartesian system) is not constant but depends linearly on the distance between the vehicle and the support vehicle (on surface).

1.4.5 EKF continue-discrete model-based

Non-linear estimation algorithms are generally more complex and require more computational resources than the linear ones. The dynamic model of the vehicle is described by continuous equations, hard to be discretized because of their intrinsic high non-linearity. Data coming from the sensors are instead sampled. For this reason, an Extended Kalman Filter (EKF) continuous-discrete has been chosen. It is worth to note that at the moment the EKF has been used only in the simulation environment; experimental tests and post-processing analyses are on-going, as explained in the results section of these chapter.

In order to use the filter, the dynamic model of the vehicle has been rewritten as fol-

lows:

$$\begin{aligned} \dot{\vec{x}}(t) &= \vec{f}(\vec{x}(t), \vec{u}(t)) + \vec{w}(t) \qquad & \vec{w}(t) &\sim N(0, Q(t)) \\ \vec{z}_k &= H\vec{x}_k + \vec{v}_k & \vec{v}_k &\sim N(0, R_k) \end{aligned} \tag{1.73}$$

Choosing as input $\vec{u}(t) = \vec{\tau}(t)$, the state $\vec{x} \in R^{12}$ and observations $\vec{z} \in R^{13}$ (obtained by: DVL, gyroscopes, USBL, IMU and depth sensor) are defined as:

$$\vec{x} = \begin{bmatrix} \vec{v} \\ \vec{\eta} \end{bmatrix} \qquad \vec{z} = \begin{bmatrix} \tilde{\vec{v}}_{1_{DVL}} \\ \tilde{\vec{v}}_{2_{gyro}} \\ \tilde{\vec{\eta}}_{1_{USBL}} \\ \tilde{\vec{\eta}}_{2_{IMU}} \\ \tilde{z}_{prof} \end{bmatrix} \tag{1.74}$$

with $\vec{x}$ composed of $\vec{v}$, the linear and angular velocities in body fame, and $\vec{\eta}$, the linear and angular coordinates in fixed frame. Omitting the time dependence t for a simpler notation:

$$\vec{f}(\vec{x}, \vec{u}) = \begin{bmatrix} M^{-1}\left(\vec{\tau} - (C(\vec{v}) - D(\vec{v}))\vec{v} - \vec{g}(\vec{v})\right) \\ J(\vec{\eta})\vec{v} \end{bmatrix} \tag{1.75}$$

H is constant:

$$H = \begin{bmatrix} I_{3\times3} & 0_{3\times3} & 0_{3\times3} & 0_{3\times3} \\ 0_{3\times3} & I_{3\times3} & 0_{3\times3} & 0_{3\times3} \\ 0_{3\times3} & 0_{3\times3} & I_{3\times3} & 0_{3\times3} \\ 0_{3\times3} & 0_{3\times3} & 0_{3\times3} & I_{3\times3} \\ 0 \quad 0 \quad 0 & 0 \quad 0 \quad 0 & 0 \quad 0 \quad 1 & 0 \quad 0 \quad 0 \end{bmatrix} \tag{1.76}$$

Q matrix represents the variance of the process, it is diagonal and its components are the parameters of the time-invariant filter: these parameters are set depending on the reliability of the implemented model. R matrix depends on the variance of the measurement error, it is diagonal and consists of the variances of the sensor errors. The purpose of the filter is to generate estimates $\hat{\vec{x}}_{k|k}$ of the status at each step k. These ones are generated by a continuous prediction model-based filter and by a discrete update based on the measures. Assuming known the initial condition, the filter is initialized with:

$$\hat{\vec{x}}_{0|0} = \vec{x}(t_0) \qquad P_{0|0} = P(t_0) \tag{1.77}$$

Prediction

The prediction is the continuous part of the filter. Through the equations

$$\dot{\hat{\vec{x}}}(t) = f(\hat{\vec{x}}(t), \vec{u}(t)) \qquad \text{with} \qquad \hat{\vec{x}}(t_{k-1}) = \hat{\vec{x}}_{k-1|k-1} \tag{1.78}$$

$$\dot{P}(t) = F(t)P(t) + P(t)F(t)^\top + Q \qquad \text{with} \qquad P(t_{k-1}) = P_{k-1|k-1} \tag{1.79}$$

where

$$F(t) = \left.\frac{\partial \vec{f}}{\partial \vec{x}}\right|_{\hat{\vec{x}}(t),\vec{u}(t)} \tag{1.80}$$

it is possible to determine the evolution of the status prediction $\hat{\vec{x}}(t)$. $\hat{\vec{x}}(t)$ can be sampled as $P(t)$ as follows:

$$\hat{\vec{x}}_{k|k-1} = \hat{\vec{x}}(t_k) \tag{1.81}$$

$$P_{k|k-1} = P(t_k) \tag{1.82}$$

Update

The update phase of the filter uses observations $\vec{z}_k$ to improve the prediction $\hat{\vec{x}}_{k|k-1}$ obtaining the estimated $\hat{\vec{x}}_{k|k}$ according to the equations:

$$K_k = P_{k|k-1}H^\top \left(HP_{k|k-1}H^\top + R_k\right)^{-1} \tag{1.83}$$

$$\hat{\vec{x}}_{k|k} = \hat{\vec{x}}_{k|k-1} + K_k\left(\vec{z}_k - H\hat{\vec{x}}_{k|k-1}\right) \tag{1.84}$$

$$P_{k|k} = (I - K_k H)\,P_{k|k-1} \tag{1.85}$$

Note that the EKF filter does not use directly the measures of the accelerometer, as it was deemed too noisy for the position estimation. In the case in which data from one or more sensors are not available for a period, the algorithm uses the last measure available, but it gives a high value to the corresponding coefficient in the H matrix: the measure, thus, will be characterized by a low weight in the estimation process.

1.4.6 Simulation results

In this section the results of the simulations, based on the models and algorithms described above, are presented. For reasons of brevity, here are reported the results based on path following navigation. Many factors that influence the vehicle dynamics have been modelled, thus the results are very useful to understand the capabilities and the possible control problems for the AUV (before the performed experimental campaign). They are also a tool allowing a pre-calibration of all the control parameters. In the presented simulations the following parameters were used: total length of the vehicle $l = 3$ m, diameter

of the vehicle $d = 0.3$ m, water density $\rho = 1030$ kg/m^3. The estimation algorithm EKF requires the knowledge of the dynamic model of the vehicle. Despite the extensive study of the AUV dynamics, a model cannot reproduce exactly the real behaviour of the vehicle. In the performed simulations the problem of using the same dynamic model of the vehicle both to simulate the behaviour of the real vehicle and for the equations of the EKF prediction algorithm arises; this would certainly lead to have better results in the simulation compared to those that would be obtained during the experimental tests. To produce results closer to reality, the dynamic elements (e.g. masses, inertia, etc.) of the matrices of the prediction equations were characterized by a 10 % degree of uncertainty, considering these as unavoidable modelling errors. The trajectories used in the tests are designed to reproduce a typical mission of immersion and exploration of the seabed. These pathways are significant, since, composed of straight sections along different directions alternating with curves on several planes, they stress the vehicle dynamics in general conditions.

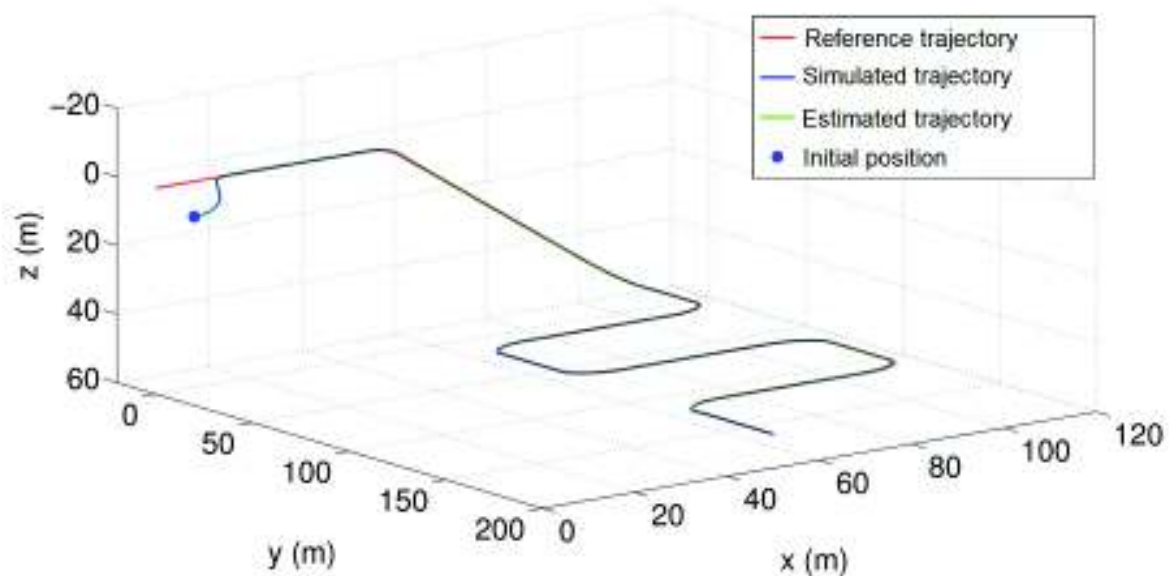

Figure 1.16: Trajectories comparison

Finally, further simulations are described, in which it is assumed that the measure of the DVL sensor is not available; this may occur for instance if the vehicle is far away from the bottom or if a failure occurs. The DVL is a sensor of considerable importance; the estimation without its measurement is worse. However using EKF, even if the estimation error is greater, the stability of the control system is not compromised (Figure 1.20).

To summarize, two different control strategies have been simulated in the Matlab-Simulink^{TM} environment. The former type of navigation is called *waypoints* and it allows the vehicle to move with a higher accuracy on straight lines connecting different important monitoring points. The vehicle stops on these points, then rotates and then proceeds to the next point. The latter is called *path following navigation* and it allows to follow a

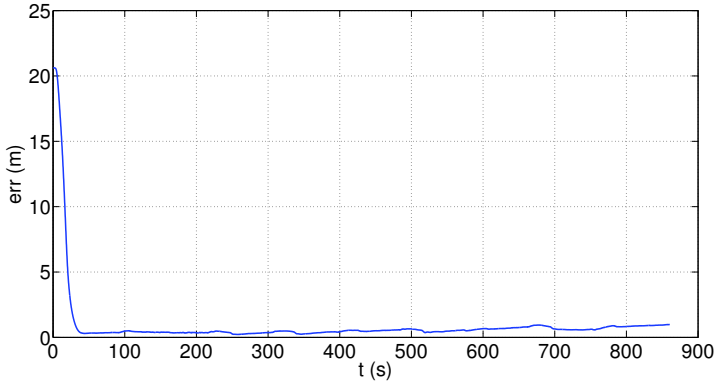

Figure 1.17: Positioning error norm against time

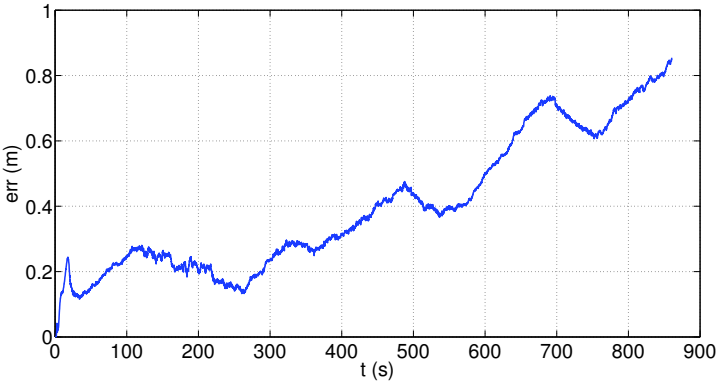

Figure 1.18: Estimating error norm against time

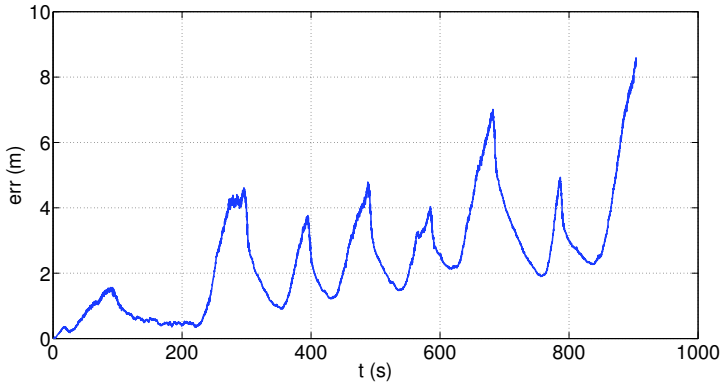

Figure 1.19: Estimation error of EKF without DVL

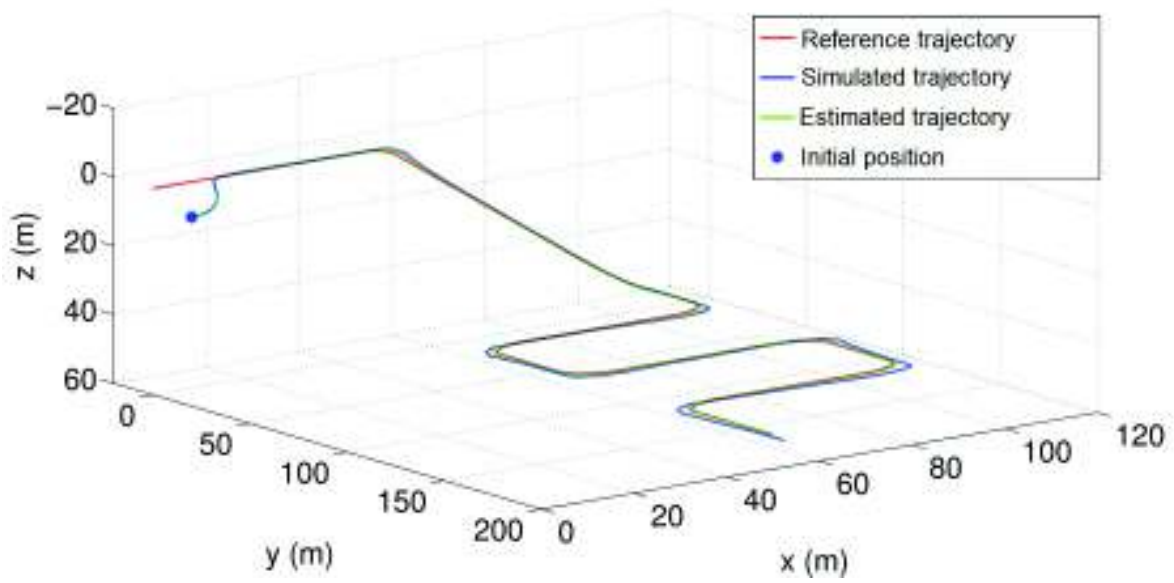

Figure 1.20: Trajectories comparison without DVL

wide variety of underwater trajectories. This second kind of navigation strategy is more suitable for the moving phase where no stops are required and the achieved results have shown that this strategy is robust as regards possible disturbances, e.g. wrong initial positioning of the vehicle, out of the desired trajectory. As regards the vehicle localization an Extended Kalman Filter (EKF) continuous-discrete has been chosen. The algorithm permits to estimate the pose of the vehicle and its speed and acceleration. This allows to locate the AUV during its missions, to geo-reference any archaeological findings and, not least, to provide the on board logic with the necessary feedbacks to control the vehicle.

1.5 Typhoon class vehicles

In the framework of the THESAURUS project a class of AUVs, called Typhoon, able to cooperate in swarms to perform navigation, exploration and surveillance of underwater archaeological sites has been developed. The project specifications are quite ambitious: the low cost vehicles have to operate with a maximum depth of 300 meters, an autonomy ranging from 8 to 12 hours is required and a maximum speed of 5-6 knots has to be achieved. Briefly, the Typhoon class AUV is a low cost vehicle with remarkable performances and power on board. In particular, it is worth to note that the depth specification is very significant for archaeological interests: the depth of 300 m is prohibitive for usual diver operations and it is also higher compared to the depth specification of many commercial low-cost AUVs. The total carried payload is quantified in about 30-40 kg and the cost of the vehicle is relatively limited.

A first fleet of three different underwater vehicles, cooperating in a single team, has been developed, as visible in Figure 1.21 ([25] and [41]). The three vehicles can be characterized as follows:

Vision Explorer A vehicle equipped with cameras, laser and structured lights for an accurate visual inspection and surveillance of archaeological sites. Visual inspection involves a short range distance (few meters) between the vehicle and the target site, and the capability of performing precise manoeuvring and hovering;

Acoustic Explorer Preliminary exploration of extended area to recognize potentially interesting sites involves the use of acoustic instruments, such as side-scan-sonar. This kind of vehicle can perform long range, extended missions. Consequently, navigation sensors able to compensate the drift of the inertial sensors, such as a DVL (Doppler Velocity Log), have to be installed on board;

Team Coordinator A vehicle with extended localization and navigation capabilities is used to coordinate the team. This vehicle periodically returns to surface providing the GPS positioning and, more generally, detailed navigation information that can be shared with other vehicles of the team. When the mission area is quite defined and a surface vehicle or a buoy are available, coordination and data transmission are performed by this dedicated device. On the other hand, when a different operating scenario is required, one or more vehicles of the team could periodically interrupt their mission performing the activity of team coordinator.

Different mission profiles should correspond to different vehicle layouts suitable and optimized for a specific task; however, in accordance with the project requirements, a hybrid design, able to satisfy different mission profiles, has been preferred, to reduce the engineering and production costs and to assure vehicle interchangeability. Each vehicle of the team can be customized for different mission profiles; so the team composition can be altered, e.g. two vehicles may be equipped for the visual inspection of a site. Since each vehicle differs only in terms of sensor layout and payload, the naval and the electromechanical design was focused on a common vehicle class. For instance, for an individual mission in which both acoustic and visual inspection of an archaeological site are required using a single vehicle the instrumentation layout described in Figure 1.22 can be easily assembled.

Following extensive engineering tests, that took part in the summer 2013 within the THESAURUS project activities, one of the Typhoon vehicle, operated by the ISME groups of the Universities of Florence and Pisa, participated in the CommsNet13 experiment,

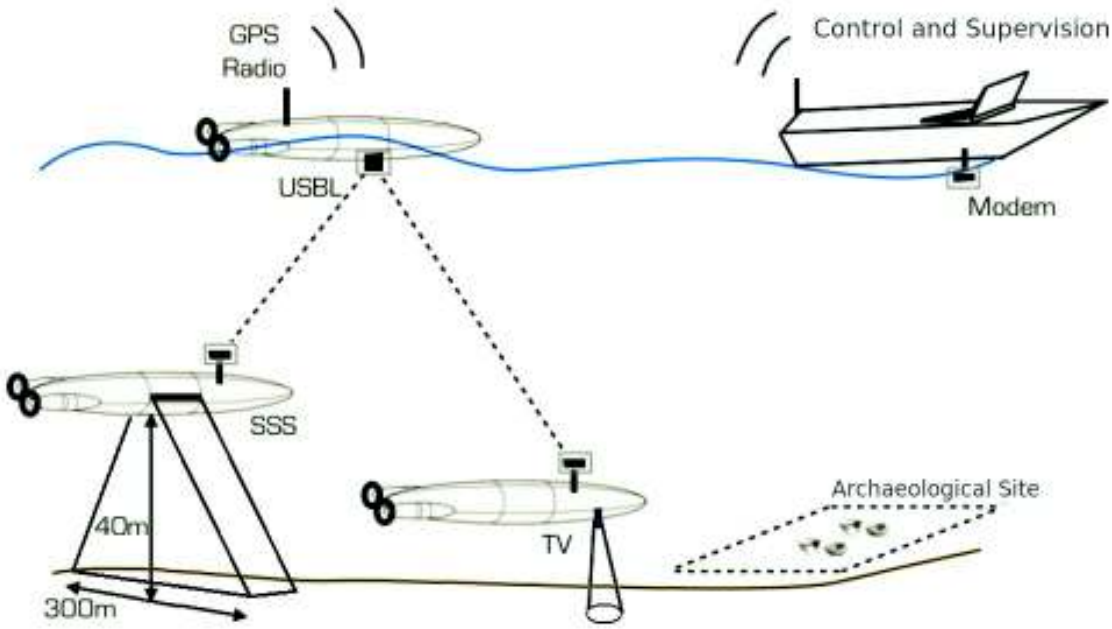

Figure 1.21: Typhoon AUVs of the swarm

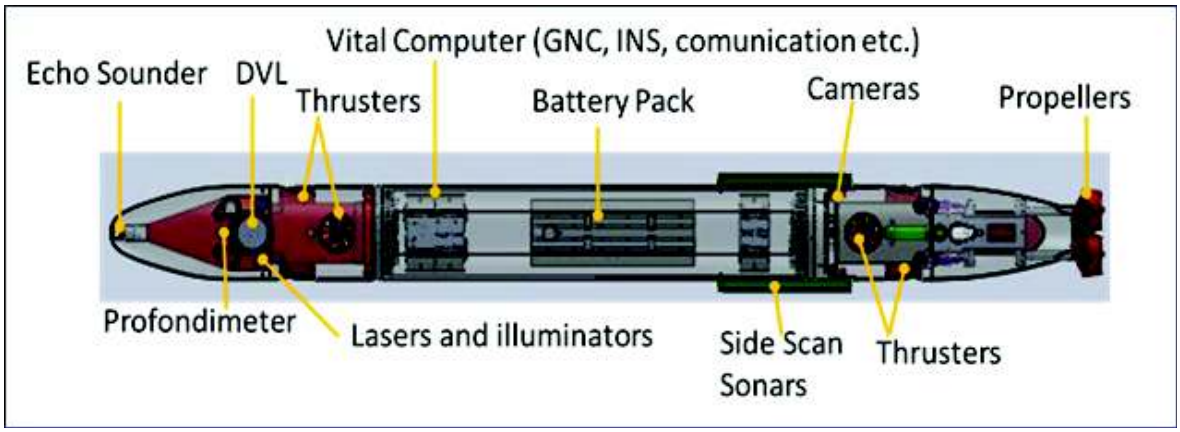

Figure 1.22: Example of Typhoon vehicle, customized for both acoustic and visual inspection of a site

Figure 1.23: Typhoon AUV: CAD design

organized by NATO CMRE in September 2013. This experiment included among its objectives the evaluation of on board acoustic USBL systems for navigation and localization of autonomous underwater vehicles. The related results are reported in the last section of this first chapter.
Moreover, in the following, Typhoon vehicle is described in more detail.

1.5.1 Typhoon Hardware

Typhoon vehicle is a middle-sized class AUV, whose features are comparable with other existing vehicles, such as Remus series from Kongsberg. Considering the vehicle sizes (length of about 3600 mm, external diameter of about 350 mm, weight of 130-180 kg according to the carried payload) and the expected performances (maximum reachable depth of about 300 m, at least 10 hours of autonomy and a maximum speed of 5-6 knots) the vehicle can be considered an intermediate one compared to the smaller Remus 100 and the bigger Remus 600. In Figure 1.23 and Figure 1.24 the Typhoon CAD design and its final built version can be seen.

Compared to existing commercially available vehicles, Typhoon presents some innovative features which greatly contribute reducing the production and maintenance costs:

- The extended use of low cost corrosion resistant materials: thanks to the use of composite material such as fibreglass, the production cost of the hull is quite low. Also the maintenance is quite simple;

- Modular mechanical design with commercial components: the use of low cost commercial Lithium-Polymer batteries contributes to reduce the costs. The actuators and the propellers of the propulsion system are completely modular and interchangeable. Both propulsion, and manoeuvring thrusters are actuated with the same motor and drive system: a standard actuation unit with a 200 W brushless motor and drive directly fed by the 48 V provided by the batteries and controlled through an

Figure 1.24: Typhoon AUV: final version

industrial CAN bus, see [13]. The calibration of the pitch static attitude can be also performed moving the accumulators whose axial position is controlled by a screw system;

- Use of fast prototyping techniques: the vehicle is easy customizable since many components and accessories are built using ABS plastic material, shaped using a 3D printer of the MDM Lab. This way, many components may be easily customized and rebuilt in few hours. Moreover, the prototyping techniques have also greatly accelerated the production of the components.

On board equipment and payload

Since every vehicle can be customized to manage different payloads and mission profiles the system was designed by dividing the on board subsystems in two main categories [41], as shown in Figures 1.25 and 1.26:

- Vital Systems: all the navigation, communication and safety related components and functions of the vehicle are controlled by an industrial PC-104, called Vital PC, whose functionality is continuously monitored by a watchdog system. Most of the

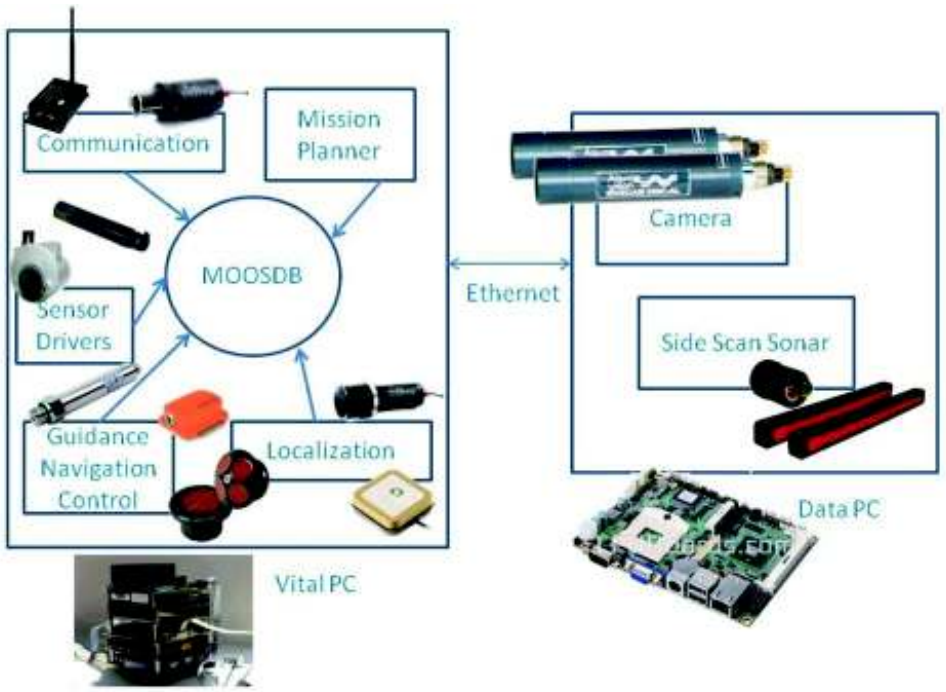

Figure 1.25: Vital instruments installed on Vital PC and optional payloads managed by Data PC

code implemented on the Vital PC is quite invariant with respect to the mission profiles and payloads, assuring a high reliability of the system;

- Customizable Payloads: all the additional sensors and functions related to variable payloads are managed by one or more Data PC. In particular, the Data PC also manages the storage on mass memories (conventional hard discs or solid state memories) and the data coming from the connected sensors. This way, all the processes introduced by additional payloads are implemented on a platform which is also physically separated from the vital one; from an electrical point of view the two parts are protected independently through fuses and relays.

In Figure 1.26 a simplified scheme of the electric plant is shown: considering the size of the vehicle and the characteristics of the propulsion system, a 48 V DC bus was chosen for both propulsion and energy storage system. To fed other instruments and sensors 24V DC, 15V DC and 12V DC voltages are provided by suitable DC-DC converters.

The on board integration utilizes MOOS (Mission Oriented Operating Suite) as software infrastructure [30]. MOOS is a publish/subscribe system for inter-process communication (IPC), which supports dynamic, asynchronous, and distributed communication. Its basic functioning, usual in all pub/sub systems, relies on a dispatcher, which is respon-

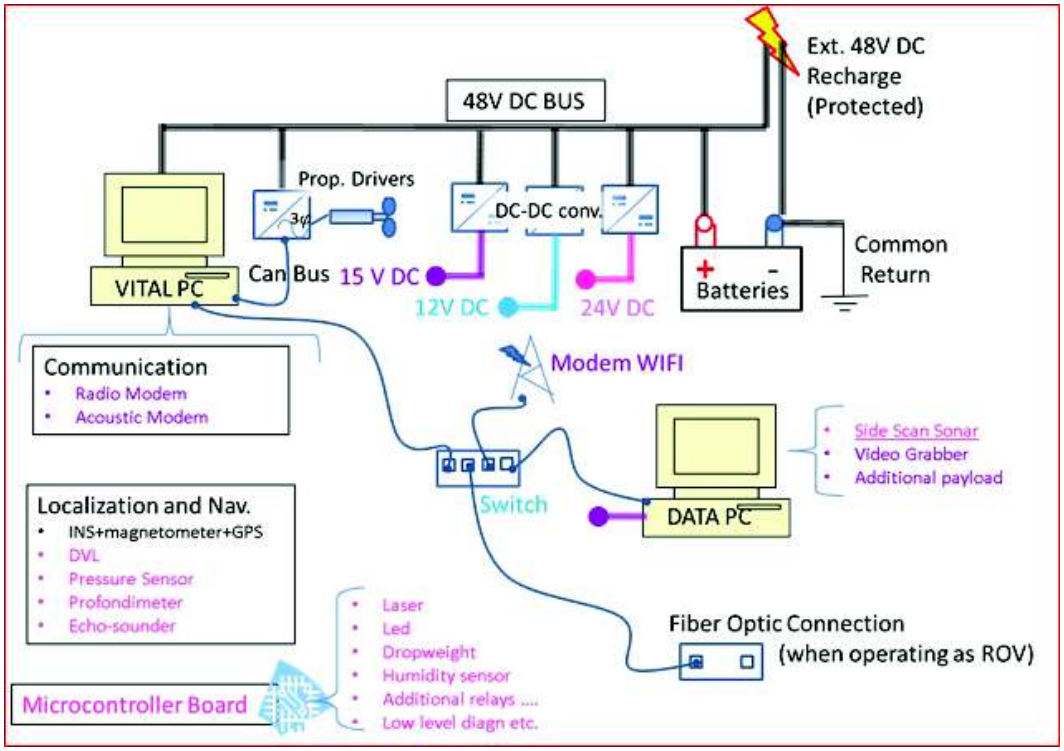

Figure 1.26: Simplified scheme of Typhoon electric/functional plant

sible for routing messages from publishers to subscribers. The messages are routed based on their topics, which is an information descriptor contained in the messages themselves. In MOOS the dispatcher is represented by a central database (called MOOSDB).

For reason of brevity here is only reported a list of the on board sensors and payloads:

- Inertial Measurement Unit (IMU) Xsens MTi: device made up of a 3D gyroscope, 3D accelerometer and 3D magnetometer furnishing dynamic data at a maximum working frequency of 100 Hz. The device measures the orientation of the vehicle in a 3D space in a accurate way thanks to an estimate inner owner algorithm;

- Doppler Velocity Log (DVL) Teledyne Explorer: sensor measuring the linear speed of the vehicle, with respect to the seabed or with respect to the water column beneath the vehicle. Moreover, if it detects the seabed it is also able to measure the distance from it (like an altimeter);

- Echo Sounder Imagenex 852: single beam sensor, mounted in the bow of the vehicle and pointing forward. It can measure the distance from the first obstacle(s) placed in front of the vehicle;

- STS DTM depth sensor: digital pressure sensor used to measure the vehicle depth;

- PA500 altimeter: device measuring the distance between the vehicle and the seabed;
- Side Scan Sonar by Tritech: device used for the acoustic survey of the seabed.

Accumulators and Energy Management System

From preliminary studies on the vehicle hull it has been possible to approximately evaluate the drag coefficients of the vehicle and to roughly estimate the needed amount of energy: the required power depends on the efficiency of the propellers, motors and transmission system. The power needed by the propulsion on board systems and payloads was approximately known (about 350 W), so, considering a mission duration of about 8-10 hours, it was possible to calculate the needed energy in about 3-3.5 kWh. In particular the value of 350 W was calculated considering the sum of the following contributions:

- Propulsion power: about 100-200 W, depending on the mission profile and speed;
- Vital navigation functions: about 50-60 W is the estimation of power consumption due to on board vital instruments that have to be fed to assure the minimal navigation and localization functions (vital PC, depth and inertial sensors, magnetometer, etc.);
- Hotel load: a continuous/mean contribution of about 100 W is considered. This value is quite sensitive to the mission profile, especially considering the multi-role capabilities of the vehicle: e.g. for visual inspection of the site higher peak consumptions of power due to the illumination of the target should be considered, while for prolonged acoustic inspections the power demand should be more continuous.

As the installed power was quite high it was decided to elevate the nominal voltage of the accumulators to 48 V, which represents a good trade-off among the different technical issues, such as the reduction of the electrical losses and the troubles related to insulation and protection of low voltage equipments (generally easier to be assembled and found with low cost commercial components). In order to maximize the capacity of the energy storage system, Li-Po (Lithium-Polymer) batteries, which have higher energy capacities [34] compared to other kinds of cheaper commercially available accumulators, as visible in Figure 1.27, have been chosen. As shown in Figure 1.27 the design of Li-Po batteries may be optimized to satisfy different Power-Energy specifications:

- HED (High Energy Density): accumulators designed to maximize Energy Density corresponding to minimal encumbrances and weights;

- HP (High Power) and UHP (Ultra High Power): accumulators suitable for higher currents.

Typhoon AUV does not require high currents, so, theoretically, High Energy Density accumulators may be the best choice; however, for a reliable and practical use, HP (High Power) Li-Po batteries support higher charging currents which make easier and faster the vehicle use and its maintenance. Besides, from a commercial point of view, HP Li-Po batteries are widely diffused and available since they are used for many applications, such as electric cars and sport vehicles; at the end, they were preferred to the HED ones. The chosen layout involves the use of two packs of batteries whose features are visible in Table 1.5 for a total power of 3.84 kWh which is enough in conformity with the specifications, even considering a performance degradation of 10% due to ageing or to incomplete/fast recharge. Since a low amount of power, corresponding to less than 10-30% of the total stored energy is required by low voltage utilities, additional DC-DC converters are added to the power system, according to the needs of the different installed components, as visible in the scheme of Figure 1.26.

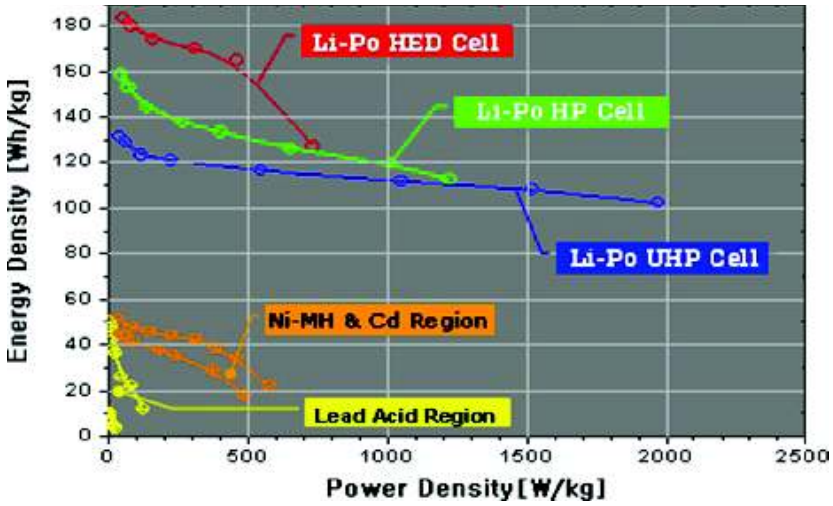

Figure 1.27: Li-Po batteries performance compared to different accumulator technologies

Table 1.5: Main features of a single battery pack

Cell Producer	Kokam assembled by Egraftech	*Max Discharge Current*	30 A
Nominal Voltage	48,1 V (3.7 V*13)	*Max Charge Current*	10 A
Cut Off Voltage	35,1 V(2.7 V*13)	*Current Capacity*	40 Ah
Maximum Voltage	54,6 V (4.2 V*13)	*Total Encumbrances*	mm 230x260x150(h)
Layout	13 Cells Series Connected	*Total Weight*	About 14-15 kg
BSM	On Board		

Propulsion system

Many AUVs described in bibliography are equipped with depth control buoyancy units (e.g. bladders) able to change the buoyancy of the vehicle and with mechatronic devices able to change the relative position of the centres of gravity and buoyancy, in order to modify the vehicle orientation [35], [36]. However in this project a vehicle with a neutral behaviour has been preferred, which complies with two conditions:

- the mean vehicle density ρ_v has to be approximately equal to the salt water one ρ_w (1.86);
- vertical alignment of the buoyancy and the gravity centres has to be assured; a negative value of z_b is typically used to stabilize the vehicle against roll motions (1.87),

$$\frac{1}{V}\int \rho \, dv = \rho_v \approx \rho_w \tag{1.86}$$

$$x_b = y_b = 0; \quad z_b \leq 0 \tag{1.87}$$

where ρ is the local density and x_b, y_b, z_b are the coordinates of the centre of buoyancy compared to a body reference system placed on the centre of mass of the vehicle.

So in case of Typhoon the vehicle movements are given by the propulsion system: in Figure 1.28 a simplified scheme of the proposed layout is shown.

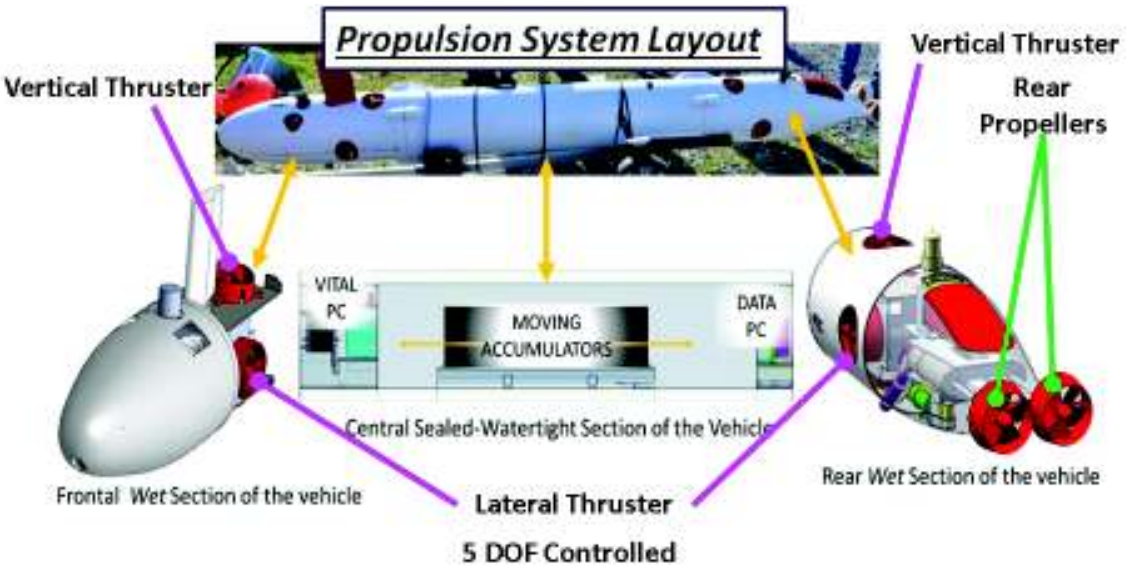

Figure 1.28: Propulsion system design

Linear motions along x, y, z directions, pitch and yaw rotations are directly controlled by a system of actuators composed of two main propellers (longitudinal) and four thrusters

(two vertical and two lateral). Moreover, as previously said, the position of the accumulators can be modified to control the vehicle pitch.

Rear Propeller design and optimization

According to the vehicle speed and manoeuvrability specifications, as the geometry of the hull and the corresponding drag coefficients were approximately known, it was possible to calculate a maximum power requirement for each actuator of about 200 W. According to the hull sizes, the chosen diameter for the lateral and vertical thrusters was 118 mm and 120 mm for the rear propellers. Then the design is optimized as to the shape of the profiles, and in particular to the ratio between the pitch p and the diameter d of the propeller. The rear propellers are ducted with a 19A nozzle [13]. The nozzles are adopted to protect each rear propeller from dangerous contacts with seaweeds, or other suspended solid bodies, and to increase the delivered thrust. For standardized propeller and nozzle series, in literature the curves where the steady state behaviour of the system is described in terms of dimensionless coefficients are available: for the design of the Typhoon these curves have been used, applying the similitude principle. In Figure 1.29, an example of these curves, available in bibliography [13], is shown. The dimensionless coefficients $K_t(J)$ (1.88), $K_q(J)$ (1.89) and $\eta(J)$ (1.90) are expressed as functions of the advance coefficient J, as defined by (1.91).

$$J = \frac{V_a}{nd} \tag{1.88}$$

$$K_t = \frac{T}{\rho n^2 d^4} \tag{1.89}$$

$$K_q = \frac{Q}{\rho n^2 d^5} \tag{1.90}$$

$$\eta = \frac{K_t J}{K_q 2\pi} \tag{1.91}$$

where n = propeller speed [Hz]; ρ = density [kg/m^3]; Q = torque [Nm]; T = thrust [N]; d = propeller diameter; V_a = advance speed (relative speed between the vehicle and incoming fluid); the adopted symbols are taken from bibliography [13].

Under the hypothesis of constant known drag coefficient C_{DX} of the vehicle, steady state resistances to a longitudinal motion are roughly proportional to V_a^2 , as stated by (1.92):

$$X = \rho \frac{\pi}{4} D^2 C_{DX} V_a^2 = k_x V_a^2 = k_x J^2 n^2 d^2 \tag{1.92}$$

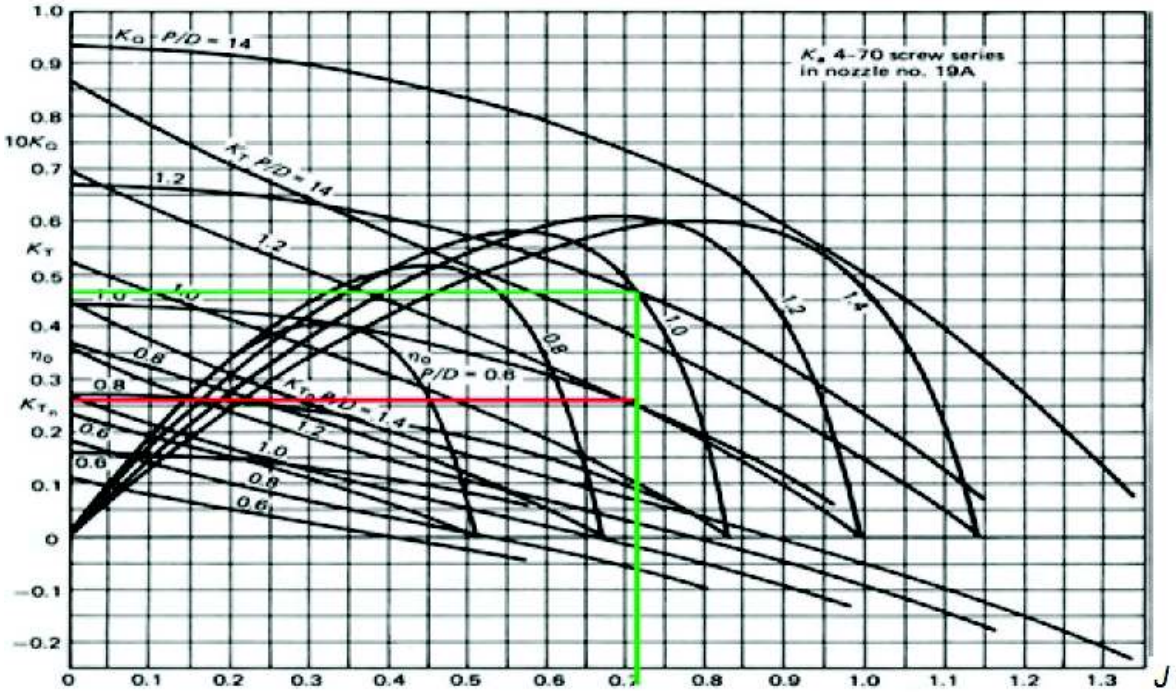

Figure 1.29: Examples of $K_t(J)$, $K_q(J)$ and $\eta(J)$ curves considering the contribution of the nozzle [13]

In steady state conditions the equilibrium between longitudinal drag forces and propeller thrusts has to be verified; considering a known number n_{prop} of identical propellers working in parallel (2 in the Typhoon application) with known $K_t(J)$, $K_q(J)$ and $\eta(J)$ curves, the equation (1.93) can be obtained:

$$X(J) = k_x J^2 n^2 d^2 = K_\eta n_{prop} K_t(J) \rho d^4 n^2 \tag{1.93}$$

where K_η is an additional efficiency coefficient (rigorously minor than one) that should be introduced to consider further dissipative effects due to the perturbation of the inlet velocity field caused by the vehicle hull passage (including vortex shedding effects). Solving the balance (1.93), a solution J is calculated.

J_* is the steady state value of the advance coefficient considering the mutual interaction between the propeller behaviour and the vehicle drag resistances. Since the value of J_* is approximately invariant as to advance speed V_a also the corresponding values of $K_t(J_*)$, $K_q(J_*)$ and $\eta(J_*)$ are assigned and can be calculated. As a consequence, for a known propeller-vehicle coupling, in order to maximize its efficiency, the system has to be optimized to comply with condition (1.94):

$$\eta(J_*) \approx \eta_{opt} = \eta(J_{opt}) \tag{1.94}$$

where J_{opt} represents the optimal propeller advance coefficient corresponding to the maximum efficiency η_{opt}. As shown in Figure 1.29, the behaviour of the thrust coefficient $K_t(J)$ is described by monotonically decreasing curves, often approximated as linear functions, of the advance coefficient J:

$$K_t(J) \approx K_{tb}\left(\frac{J_{null}-J}{J_{null}}\right) = K_{tb}\left(\frac{\frac{p}{d}k_{null}-J}{\frac{p}{d}k_{null}}\right) \tag{1.95}$$

where J_{null} represents the no-load advance coefficient related to the delivered thrust of the propeller equal to zero; $K_{tb} = K_t(0)$ is the value of the thrust coefficient calculated for an advance coefficient equal to zero (Bollard Thrust). J_{null} is approximately proportional to the propeller p/d ratio, through a coefficient k_{null} close to 1:

$$J_{null} \approx k_{null}\frac{p}{d} \tag{1.96}$$

K_{tb} value, for propellers of the same series, is an increasing monotonic function of p/d ratio. Merging the steady state equilibrium described by (1.93) with the linearised propeller model (1.95), equation (1.97) is obtained. Since it is a second order polynomial function, it can be easily solved as to J: the only physically admissible solution is J_* that, with the over-mentioned simplifying hypotheses, is almost invariant both as to the advance and the rotational speed, V_a and n.

$$k_x J^2 + \frac{n_{prop}K_\eta K_{tb}\rho d^2}{\frac{p}{d}k_{null}}J - \eta_{prop}K_\eta K_{tb}\rho d^2 = 0 \tag{1.97}$$

According to equations (1.93) and (1.97), the performances of a propeller are rigidly customized and optimized for a known vehicle and mission role. Due to the high numbers of installed actuators (two rear propellers and four manoeuvring thrusters), the adoption of propellers with variable p/d ratio was not considered a practicable solution. To easily produce a wide variety of low cost propeller profiles (to be tested or substituted according to the chosen mission program), the propellers have been produced by fast prototyping techniques allowing to pass from the sketch to a plastic prototype in a few hours.

The profiles were first designed using specialized tools available online, such as Maritime Propeller Geometry, or by reconstructing blade sections from the data in bibliography [13]. The propeller design has been slightly modified to easily create a prototype through the Stratasys Dimension 3D printer of the MDM Lab. A high number of blades (5) was chosen to improve the mechanical endurance and the reliability of the propeller. An example of propeller prototype is shown in Figure 1.30.

Figure 1.30: Propeller example: from CAD design to fast prototyping

In order to reduce the mechanical losses and the high frequency noise arising from a mechanical gearbox transmission, the rear propellers are actuated by direct drive permanent magnet brushless motor, controlled by a driver able to perform both speed and torque control fed at 48 V. The motor case is filled with dielectric oil, which protects the motor from salt water and assures an automatic internal compensation of the external hydrostatic pressure due to the sea depth. The external pressure is transmitted to the dielectric oil through a flexible pipe; consequently, the external hydrostatic pressure is almost entirely balanced by the internal one, preserving the case of the motor from excessive structural stresses. The presence of the lubricating oil and of the surrounding water environment drastically influences the performances of the motor: a liquid cooled motor can tolerate a drastic increase of the performances due to the improved thermal behaviour. For instance, a standard PM brushless motor with a continuous nominal power of $100-200$ W can tolerate continuous operations involving almost $150-200\%$ in terms of currents and even $200-400\%$ in terms of absorbed power. Thus, Typhoon motors are reliable and able to reach over performances, only limited by the motor drivers and by autonomy considerations (accumulator size). The assembled actuator composed of the motor and the propeller was tested in the swimming pool of the MDM Lab using the experimental layout described in Figure 1.31, both in single and double configuration (Figure 1.32). Aims of this test were both the calculation of the K_{tb} of the propeller and a preliminary analysis of the actuator performances and efficiency. In Figure 1.33 and Figure 1.34 some results concerning the bollard thrust tests are shown considering three similar propellers with different p/d ratio: in Figure 1.33it is quite easy to find the interpolating parabola describing the trend of the identified K_{tb} of the propeller.

Looking at thrust power curves of Figure 1.34 it is also clearly visible the linear behaviour of the thrust as to the required power. In both cases the testing results are confined to a maximum delivered power of 200 W which is the target one; however, as previously said, the system has successfully worked over $400-500$ W continuously (limitation due to the adopted motor drive).

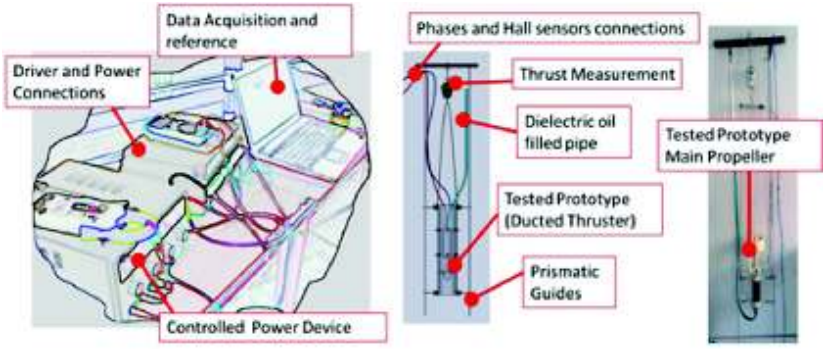

Figure 1.31: Experimental layout for the evaluation of the propeller bollard thrust

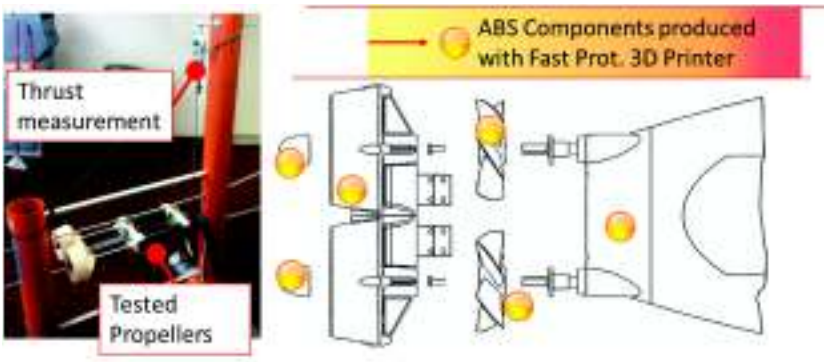

Figure 1.32: Testing device for bollard thrust measurement (left side) and corresponding solution on the vehicle (right side)

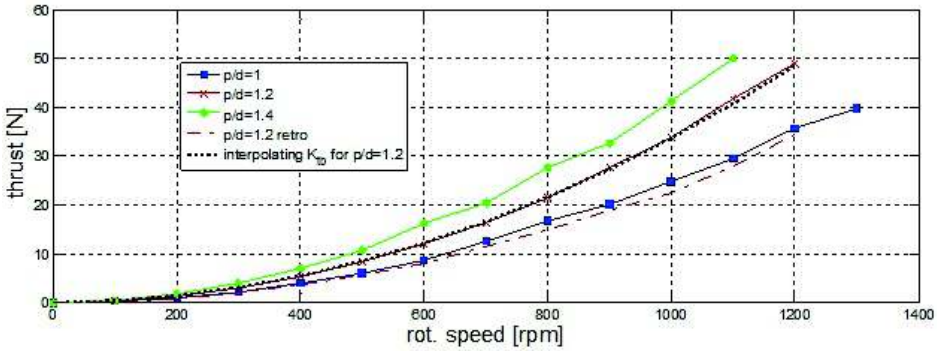

Figure 1.33: Thrust vs. speed curves (bollard thrust) for 5 blades Kaplan propellers with an area ratio of 0.9

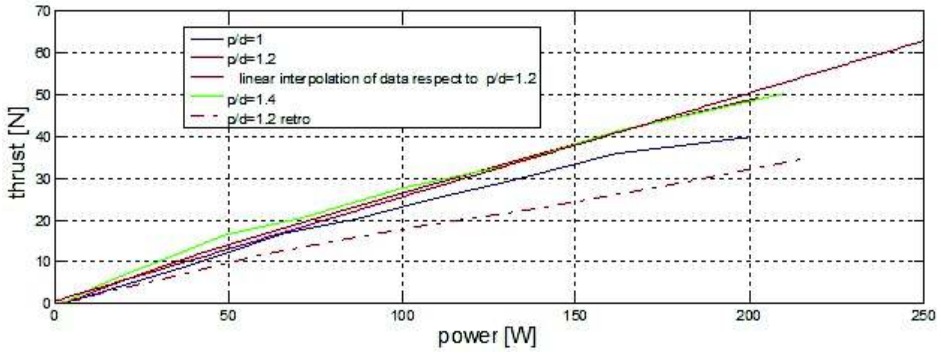

Figure 1.34: Thrust vs. power curves (bollard thrust) for 5 blades Kaplan propellers with an area ratio of 0.9

Manoeuvring Thrusters

As concerns the design of the manoeuvring thrusters the followed approach is slightly different. In particular, if the intermittent use of the thrusters is considered, the optimization of their efficiency is less important than having a compact modular design, shown in Figure 1.35: a lighter motor with a gearbox is preferred. In the propeller design, a higher attention is given to the four quadrant operations: the response of the propeller has to be optimized to be quite insensitive to the sign of the rotating speed. As a first consequence, the typical accelerating nozzle and the design criteria of the blade profiles, suitable to optimize the efficiency in a preferential rotation sense, cannot be adopted. Moreover, the thrusters are used to control the lateral, vertical and turning motions of the vehicle; the hydrodynamical resistances associated to a pure lateral motion of the vehicle are far higher compared to the longitudinal ones (one-two orders of magnitude, according to the vehicle shape). The design of the thrusters, suitable to operate taking into account the four quadrant operations, is an important engineering topic and many references can be found in literature [13] [42] [14] [43]. The use of lower p/d ratio for thruster blades, compared to the longitudinal propeller ones, is highly recommended. Typically, the proposed blade profiles are symmetric and their shapes are designed using simple elliptic or parabolic profiles; this geometry is further simplified considering limitations and constraints deriving from the adopted fast prototyping technology (mechanical tolerances, general workability and mechanical properties of the used material). This is shown in Figure 1.36, where a profile suggested in literature is compared to the one really adopted for the Typhoon thrusters.

To verify the performances of the designed thruster profiles for the four quadrant operations, many experimental tests were performed in the pool of MDM Lab: one of the main aim of these tests was the evaluation of the sensitivity of the measured bollard thrust as to the propeller sense of rotation. In Figure 1.37 some experimental results are shown: the three tested propellers have the same number of blades (seven) and similar profiles,

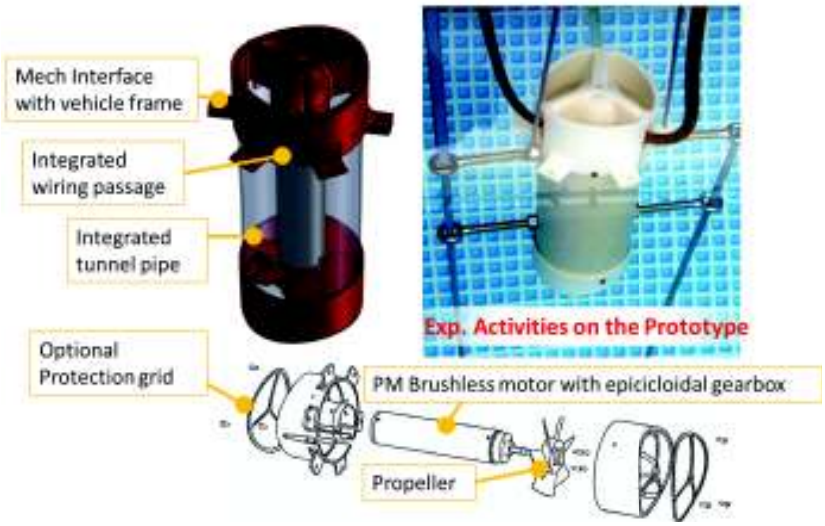

Figure 1.35: Modular thruster designed for Typhoon vehicle

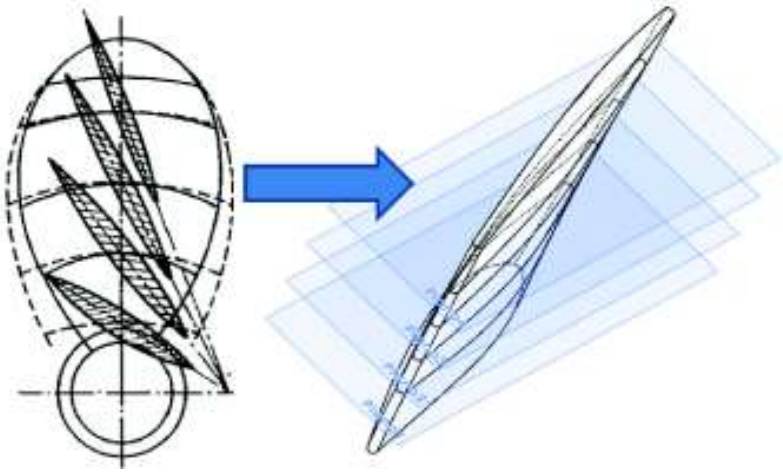

Figure 1.36: Symmetric blade profiles suggested for four quadrant operations and the corresponding profile adopted for Typhoon thruster

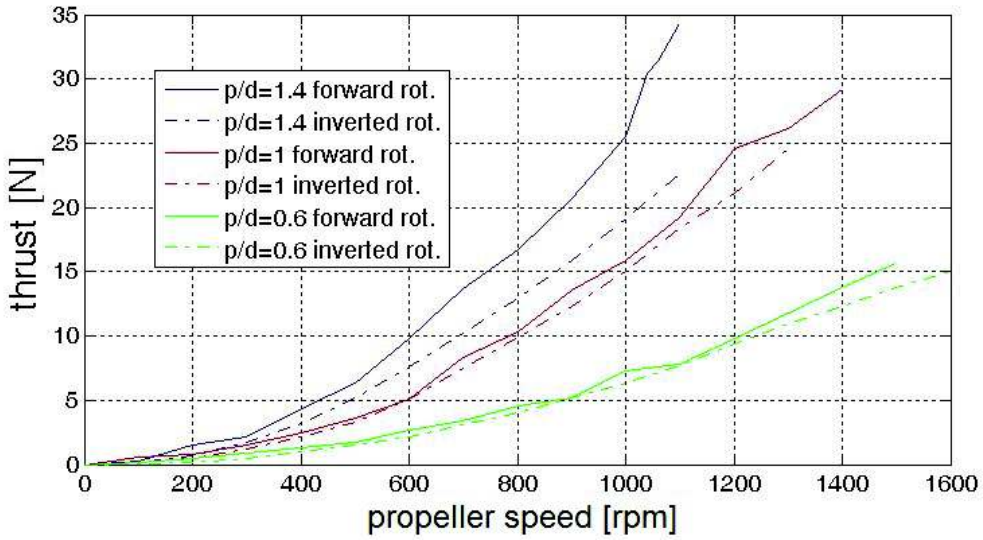

Figure 1.37: Measured bollard thrust with different rotation sense and p/d ratio of the propellers

but different p/d ratios; as clearly visible from the experimental results, the profiles with a lower p/d show a more symmetric behaviour (as to the sense of rotation).

1.6 Experimental results

The CommsNet13 experiment took place in September 2013 in the La Spezia Gulf, North Tyrrhenian Sea. Organized and scientifically led by the NATO S&T Org. Ctr. for Maritime Research and Experimentation (CMRE, formerly NURC), with the participation of several research institutions, the experiment included among its objectives the evaluation of on board acoustic USBL systems for navigation and localization of Autonomous Underwater Vehicles (AUVs). The ISME groups of the Universities of Florence and Pisa jointly participated to the experiment with one “Typhoon” class vehicle (the 300 m depth rated AUV with acoustic communication capabilities originally developed by the two groups for archaeological search). The CommsNet13 Typhoon, equipped with an acoustic modem/USBL head, navigated within the fixed nodes acoustic network deployed by CMRE. This allows comparison between inertial navigation, acoustic self-localization and ground truth represented by GPS signals (when the vehicle was at the surface). In this section the experiment is described and the results achieved with Typhoon are shown: the results show that the acoustic USBL self-localization is effective, and it has the potential to improve the overall vehicle navigation capabilities.

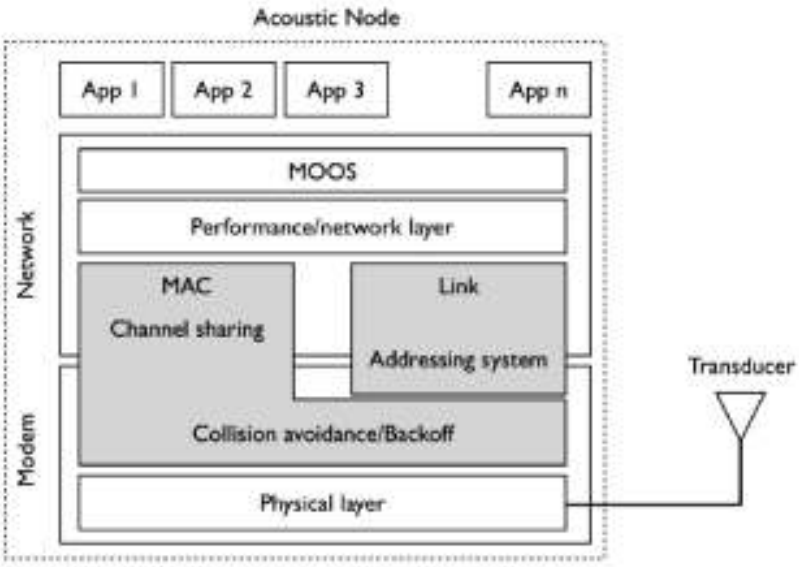

Figure 1.38: Layered structure of the underwater acoustic network

1.6.1 Acoustic Communication

The acoustic communication system has been designed having in mind an operation with a team of Typhoon vehicles. To this aim, the vehicles have to establish a communication network based on a time-sharing bi-directional/broadcast communication scheme. The goal is to create a flexible structure capable of ensuring low-delay communication and the reliable transmission of specific messages necessary for the safety of the swarm and for exploration missions. The network is composed of a few layers, as shown in Figure 1.38, and it does not include most of the complexity typically present in terrestrial networks. The implemented networking system has already been described in [44]. Its main features are reported here for self-consistency. The bottom layer is represented by the EvoLogics acoustic modem/USBL, which manages the physical transmission of the signal into the water. The adopted communication mode provided by the modem, namely instant messaging, does not require connection establishment procedures, allows for broadcast messaging and permits a message maximum size of 64 bytes. The modem also implements collision avoidance techniques (Medium Access Control - MAC) and provides basic network functionalities, including an addressing system that can be exploited at the link layer. The medium access control is completed through a channel time division mechanism: time is divided into slots and each nodes is assigned a slot where it has to concentrate all its communication burden. The network link layer is composed of a combination of the modem networking features and of the MOOS (Mission Oriented Operating Suite) framework, [30]. MOOS is a publisher/subscriber system for inter-process communication through message exchange. Messages are associated to

an information descriptor, called topic, contained in the messages themselves. Publishers send their messages to a dispatcher, represented by a central database (MOOSDB), which is responsible for forwarding messages to the subscribers based on their topic. Subscribers have to preliminary declare their interest in specific topics by issuing subscription to the dispatcher itself. Within this setting, each acoustic node is equipped with a process that handles the communication with the acoustic device: when a new message is received from the modem, it publishes the information in the INBOX topic, while during a transmission, it reads a message from the OUTBOX topic and forwards it to the modem for the physical transmission. To increase the throughput of the network and the probability that an important message is transmitted as soon as possible, messages are organized in a priority queue. More specifically, four classes of messages have been identified, each of which associated with a decreasing priority; among them, localization messages, periodically exchanged between the vehicles to have USBL updates or range measurements, are relevant to the aim of CommsNet13 experiment. To avoid an indefinitely growth of the queue when an application generates data at a higher rate than the acoustic channel can support, at each step the messages are filtered on the basis of the time slot duration and those that cannot fit into the available time are discarded. Moreover, the organization of the queue is performed both during the non-communication periods and the communication time slot available to the vehicle; this way, the network supports real-time data delivery, meaning that the data are produced, organized and then transmitted during the communication period of the node. The highest layer, namely the application layer, utilizes MOOS as software infrastructure. An application which wants to join the network, has only to publish in the topic OUTBOX the data to be sent acoustically towards the desired nodes and to register to the topic INBOX to be notified when new acoustic messages are received. This way, the network becomes completely transparent from the application point of view.

1.6.2 Experiment Description

The CommsNet13 experiment has been organized by the NATO Centre for Maritime Research and Experimentation (CMRE, formerly NURC) with the main objective to test the performance of several acoustic communication and localization systems using underwater networks. Several teams from different institutions, each one interested in testing different systems, have been involved in the experimentations, held with the support of NRV Alliance. CommsNet13 took place from Sept. 9^{th} to Sept. 22^{th} 2013 in La Spezia and was originally planned in the west area of Palmaria island, Gulf of La Spezia, North Tyrrhenian Sea, where CMRE has a permanent testbed for underwater networking and communication purposes (LOON - Littoral Ocean Observatory Network). In Comm-

sNet13, the LOON installation consisted of four EvoLogics modems, placed on the seabed and cable-connected to the shore so that they could be continuously operated and monitored. The LOON modems are compatible with those installed on board the Typhoon, so that the vehicle could use its USBL modem to estimate its relative position with respect to the fixed LOON installation. Hence, the role of the Typhoon in this experimentation was to perform both surface and underwater navigation in autonomous modality, while trying to localize itself or the other nodes of the network using the USBL measurement. In the first week, due to adverse sea and weather conditions, a preliminary test was carried out within the La Spezia harbour using re-deployable, battery operated, EvoLogics modems as fixed nodes. In the second week, the trial was carried out in the open sea close to the LOON area. The operating groups have worked in parallel as much as possible, but most of the trials were carried out in series to not interfere the one with the others. Due to the weather constraints and to the time-division nature of the experiment, it was possible to do a limited number of runs, all using the Typhoon mounting the USBL head. In the following section, the results as obtained in some of the runs will be illustrated.

1.6.3 Results at CommsNet13

The results of the Typhoon trials that took place on Sept. 12^{th} and Sept. 22^{th} 2013 are now reported. In the first one, Typhoon has executed an autonomous mission within the La Spezia harbour, consisting in the repetition of a triangle-shaped path with vertices placed in the waypoints WP1, WP2 and WP3. In this area, some battery-operated modems were deployed to build an ad-hoc installation of fixed nodes: using them the vehicle could localize itself using its on board USBL. In the second one, Typhoon was supposed to autonomously travel along a path on the LOON area, localizing itself with respect to the LOON submerged modems by means of the on board USBL modem. The reference path for the mission was defined by three waypoints respectively called Janus1, M2 (position of the second one of the four LOON modems) and Typhoon1. In both runs, the absolute position of the fixed nodes is known, so the relative localization with respect to them allows to deduce a measure of the absolute position of the Typhoon. In Table 1.6 the waypoints

Table 1.6: Definition of the mission Waypoints

Date	Waypoint	Latitude (°)	Longitude (°)
Sept. 12^{th}	WP1	44.095000	9.862050
	WP2	44.094300	9.859420
	WP3	44.093750	9.861580
Sept. 22^{th}	Janus1 (J1)	44.031890	9.830962
	M2	44.032116	9.828285
	Typhoon1 (T1)	44.030610	9.829312

of the two missions are defined. In the Sept. 12^{th} run, Typhoon began the autonomous mission from waypoint WP1, then it had to repeat the reference path for two times, both on surface. Navigation was performed on the basis of GPS measurements, so that they can be used in post-processing as a ground-truth to evaluate the accuracy of USBL fixes. In the Sept. 22^{th} run, Typhoon reached J1 from the deployment point, then it travelled three times along the triangle J1-M2-T1-J1: the first and the third times on the surface whereas the second time at a depth of 5 meters surfacing on each waypoint and every two and a half minutes to reset the drift in the position estimation through a GPS fix. The paths were both covered with a reference speed of 0.7 m/s. The two triangles are between 550 m and 600 m long; the detailed subdivision of the paths is reported in Table 1.7. Tolerance on waypoints, to consider them achieved, was always set to 20 m. A direct comparison of

Table 1.7: Lengths of the path segments

Date	Segment	Length (m)
Sept. 12^{th}	WP1-WP2	225
	WP2-WP3	183
	WP3-WP1	144
	Total	552
Sept. 22^{th}	J1-M2	216
	M2-T1	186
	T1-J1	194
	Total	596

raw navigation data (GPS, USBL and dead reckoning) is given in Figure 1.39, where all the significant mission variables are shown. Moreover, as concerns the part of the Sept. 22^{th} Typhoon experiment conducted on the LOON an image by Google Earth is displayed in Figure 1.40.

In the plots, the following elements are represented:

Magenta diamonds Waypoints, identified by their short name;

Continue blue line It represents the travelled path estimated through the GPS measurements in Figure 1.39(a) and dead reckoning algorithm based on orientation measurements from IMU, a forward speed calculated as function of the longitudinal propeller thrust and GPS fixes in Figure 1.39(b);

Red circles In Figure 1.39(b), they represent GPS fixes. They are dense around the points of surfacing and absent when Typhoon antenna was underwater;

Red downward-pointing triangle Points of the estimated path corresponding to the moment when Typhoon was able to localize one of the LOON modems;

Black upward-pointing triangle Typhoon estimated position on the basis of the acoustic fixes from the USBL modem.

Downward-pointing triangles and Upward-pointing triangles are associated through a progressive numeration. The amount of acoustic fixes obtained during the two missions is respectively 19 and 10, received with an average period of 69 s in the first trial and 119 s in the second one. In Table 1.8 the navigation errors between the position estimated through the measurements of the navigation sensors and the corresponding one based on the USBL fixes are reported for both trials. Since the navigation of the Sept. 12^{th} trial was entirely based on GPS measurements, the errors obtained from this run are particularly relevant to quantify the reliability of the USBL-based position estimate with respect to the effective navigation position. The position estimation error accumulated during

Table 1.8: Error between estimated position and USBL fixes

Sept. 12^{th}				Sept. 22^{th}	
Fix	Error (m)	Fix	Error (m)	Fix	Error (m)
1	2.35	11	8.48	1	18.89
2	2.27	12	2.15	2	27.41
3	3.38	13	5.94	3	14.42
4	8.18	14	8.44	4	19.26
5	3.04	15	4.26	5	24.85
6	13.23	16	9.83	6	7.89
7	2.91	17	11.55	7	14.91
8	1.89	18	1.32	8	21.76
9	3.11	19	1.16	9	12.20
10	5.09			10	12.49

the underwater navigation of the Sept. 22^{th} mission can be evaluated as the distance between the first fix after surfacing and the last estimated position before it. Typhoon surfaced five times during the analysed part of the mission; for each of these, the value of the accumulated drift is reported in Table 1.9.

Table 1.9: Error of the dead reckoning position estimation with respect to GPS fixes

Surfacing	Accumulated drift (m)
1	13.99
2	22.39
3	35.05
4	19.59
5	24.36

While the errors reported in Table 1.8 and Table 1.9 are to be expected considering the

navigation sensors employed, it is clear that the combination of acoustic and on board sensor navigation offers the opportunity to improve navigation capabilities. This processing is currently on-going and it will be reported in the near future.

To summarize, in this section the contribution of the Typhoon AUV, developed in the framework of the THESAURUS project, to the CommsNet13 experiment, organized by NATO S&T Org. Ctr. for Maritime Research and Experimentation (CMRE, formerly NURC), held with the support of NRV Alliance, has been described. Typhoon AUV, at its first experimental experience after the end of the THESAURUS project, proved to be able to perform the required tasks completely autonomously, playing a fundamental role for the CommsNet13 experiment. Raw navigation and acoustic localization data logged from the on board sensors during a part of one of the missions performed by Typhoon during the two weeks of experimentation are here reported. The logged data will be used for a systematic post-process activity in order to investigate and test navigation data fusion procedures in order to improve localization accuracy with respect to the raw data reported here. Finally, Figure 1.41 shows Typhoon AUV during a surface phase of one of the missions performed in the Ligurian Sea in front of Porto Venere during CommsNet13.

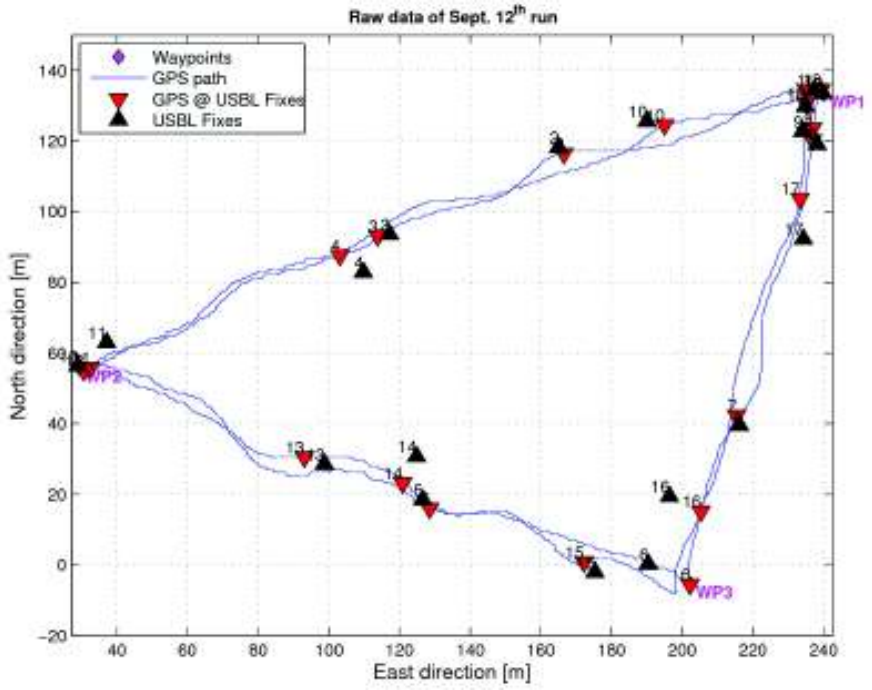

(a)

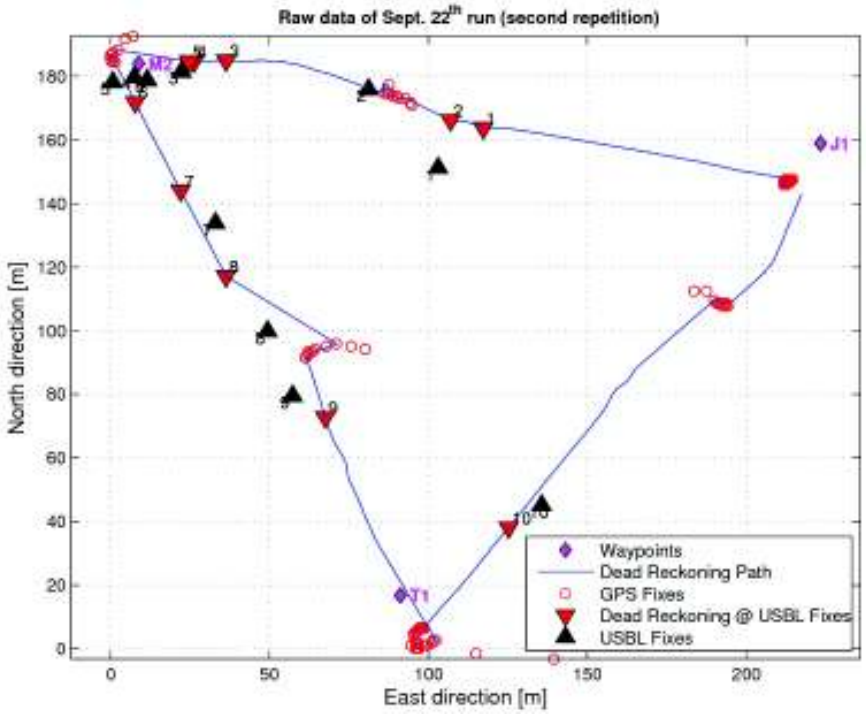

(b)

Figure 1.39: Matlab plot of the two experiments. In Figure 1.39(a) is represented the Typhoon run of Sept. 12^{th} executed in La Spezia harbour, while in Figure 1.39(b) is illustrated part of the Sept. 22^{th} Typhoon experiment conducted on the LOON

Figure 1.40: Part of the Sept. 22^{th} Typhoon experiment conducted on the LOON: image from Google Earth

Figure 1.41: Typhoon AUV during CommsNet13 experiment

Chapter 2

Nemo ROV

2.1 State of the art of ROVs

A remote-control submarine, commonly called ROV (Remotely Operated underwater Vehicle), is a mobile robot piloted at distance and used in underwater applications; these devices are widely used and suitable for different scenarios. One of the first ROVs of historical importance is called Argo, (Figure 2.1): it was born in 1985 and brought to the finding of the "Titanic" wreck. Argo has a series of cameras allowing it to shoot photos and tape videos in a panoramic size. It has a poor hydrodynamic layout and illumination is given by glow-lamps. The main problem was its insufficient manoeuvrability from the surface.

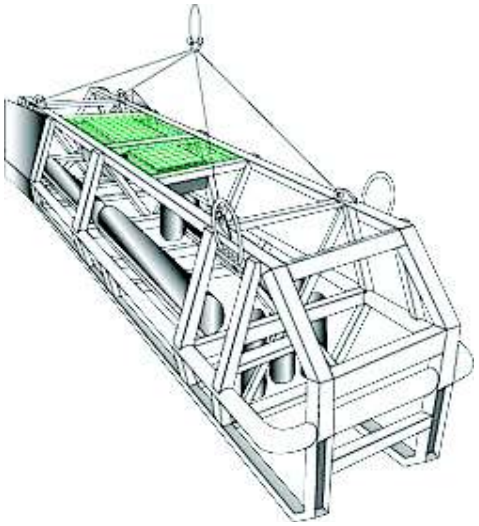

Figure 2.1: Argo

Since 1985 many things have been changed and the ROVs have become more and more advanced. At the same rate with the progressive technological development of these vehicles, the market of the specialized component industry is fast-increasing: there are for

instance mechanical builders satisfying the requests of the hyperbaric technology (e.g. watertight containers, hydraulic or electrical propellers, underwater cables, connectors, etc.) and sensor producers (acoustic, optic, chemical, physical). It is growing too the number of specialized companies in technical subsystems such as: acoustic positioning equipments, localization systems, robotic arms or other tools able to face complex underwater operations with remarkable accuracy. In the half of the nineties the Department of Marine Robotics of the CNR in Genova (CNR-IAN), realized Romeo (Figure 2.2(a)), with its following utilization, between 1997 and 2006, in different projects funded by the National program Programma Nazionale di Ricerche in Antartide (PNRA). The aim is to gather data, samples and images about the biological activities beneath the frozen blanket, supporting the experimentation of acoustic instruments in polar environment.

A ROV allows to investigate areas inaccessible to the human being or dangerous for himself: it can be sent where the hydrostatic pressures are very high and work in areas polluted by hydrocarbons, such as in case of Super Achille (Figure 2.2(b)) used for the search of the ghost ship known as "poison ship" containing dangerous toxic substances or such as Pluto Plus (Figure 2.2(c)) belonging to the Italian Navy used in mined areas. Moreover, a ROV can survey hardly accessible wrecks, such as Pollux (Figure 2.2(d)) used for the archaeological search of the Polluce wreck, placed at a depth of 103 m since 1841, or such as Pluto Palla (Figure 2.2(e)), which on June 17th, 2012, photographed for the first time the wreck of the military battleship Roma. Thanks to these vehicles many new animal species living in the depth of the sea have been discovered: in 2006 the Istituto Nazionale di Oceanografia e di Geofisica Sperimentale - OGS presented Prometeo (Figure 2.2(f)) allowing to identify particular animal species in the seabed of the gulf of Trieste.

Each vehicle is planned to perform particular tasks and on the basis of these, the vehicle structure can deeply change. In order to contextualize Nemo ROV, i.e. the ROV prototype described in this chapter, a possible classification of the ROVs [32] is here given considering weight, maximum reachable depth or power supply on board:

- *micro* - very small in size and weight: they can weigh about 3 kg (e.g. Figure 2.3);
- *mini* - they weigh about 15 kg, one person can carry the complete ROV system in a small boat (e.g. Figure 2.4);
- *general* - equipped with engines of about 5 hp, they can include a sonar and they are usually used to carry out explorations (e.g. Figure 2.5). The typical operating depth is equal 1000 m, even if exist models to reach greater depths (up to 7000 m);
- *light work class* - equipped with engines of about 50 hp, they can mount a manipulator and have a maximum depth of operation of about 2000 m (e.g. Figure 2.6);

(a) Romeo

(b) Super Achille

(c) Pluto Plus

(d) Pollux

(e) Pluto Palla

(f) Prometeo

Figure 2.2: ROV examples

Figure 2.3: GNOM Baby

Figure 2.4: Observer

Figure 2.5: Perseo GT

Figure 2.6: Comanche

- *heavy work class* - equipped with engines up to 220 hp, they can install up to two manipulators and work up to a depth of about 3500 m (e.g. Figure 2.7);

Figure 2.7: Quantum

- *trenching/burial* - equipped with engines between 200 and 500 hp. They can work up to a depth of 6000 m.

Sometimes micro and mini classes are grouped in *eyeball class* to distinguish the ROVs of just observation to the ones able to make interventions too.

2.2 Exploration of Costa Concordia wreck: Nemo ROV design

On the evening of January 13th 2012 “Costa Concordia” ship, which was cruising in the Mediterranean Sea, at 21.42 crashed into the smallest rock of “Le Scole” placed about 500 m from the harbour of the Isola del Giglio (Figure 2.8).

The collision provoked a break of 70 m in the hull (Figure 2.9) bringing a partial sinking of the ship (Figure 2.10) and causing 30 dead people, two missing and several injured.

Since then, state agencies and specialized companies are working by combined operations, initially to perform the activities of search and rescue, later for the security of the wreck and finally for the raising of the wreck itself. On request of the Italian Dipartimento della Protezione Civile (DPC) della Presidenza del Consiglio dei Ministri (Figure 2.11), the research group of Professor Nicola Casagli of the Department of Earth Science of the University of Florence, Center of Jurisdiction of the Protezione Civile itself, has coordinated the activities of monitoring and control of the ship stability.

Such activities are carried out strictly coordinated with the mission technical structure of the Protezione Civile, with operating forces (Vigili del Fuoco, Capitaneria di Porto, Marina Militare) with the Centri Funzionali Centrali of DPC and of Regione Toscana, with

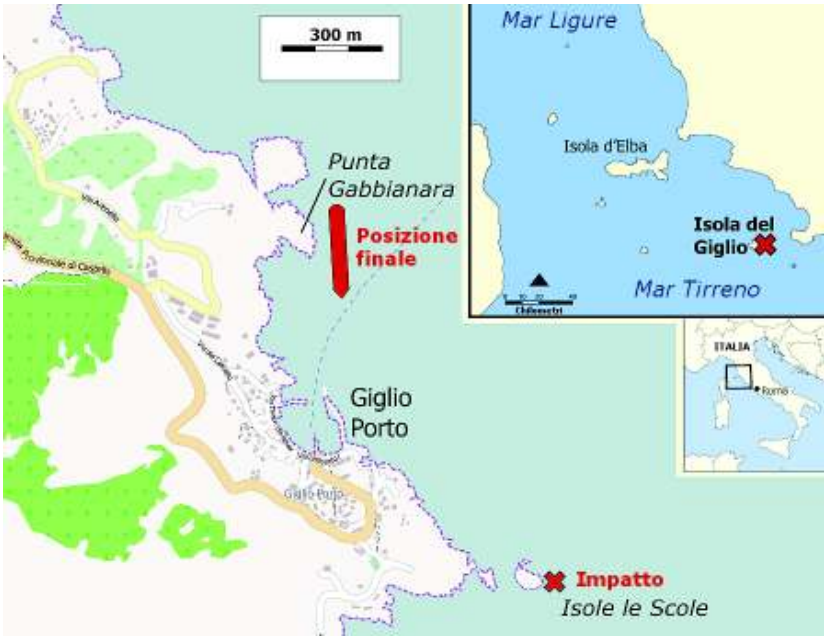

Figure 2.8: Site of the partial sinking of Costa Concordia ship

Figure 2.9: Break in the Costa Concordia hull (photo by Francesco Mugnai)

Centri di Competenza (CNR-IRPI, ASI), research institutions (EC-JRC-IPSC, OGS, Fondazione Prato Ricerche, Politecnico di Milano) and specialized companies.

The monitoring system was fit up in January 18th 2012, the same day of the request for assistance arrived from the Protezione Civile and it was fully operating since the following day. The fit up monitoring net allows to measure in real time the deformation of the whole hull, with high accuracy (mm rate). The system is an early warning instrument in support of all activities being carried out on the wreck. The ship was constantly slowly moving with acceleration phases caused by the weather-sea conditions. In such a circumstance it has been observed that in the emergency phases associated to a shipwreck, the underwater

Figure 2.10: Wreck view from Punta Gabbianara (photo by Francesco Mugnai)

PROTEZIONE CIVILE
Presidenza del Consiglio dei Ministri
Dipartimento della Protezione Civile

Figure 2.11: Protezione Civile logo

inspection, search and raising activities are strictly limited by the safety conditions of the operators. The ship deformations, the activities linked to the raising of the ship itself, arranged with the safety conditions of the scuba-divers may be critical. The employment of a versatile and handy underwater robot is consequently fundamental to reduce the exposure to risk to the underwater operators. Nemo ROV project, ordered by the Risk Office of the Protezione Civile, was born in this context and was conceived to operate in extreme local conditions on the basis of the expertise developed by the Department of Earth Science of the University of Florence in monitoring activities.

The specific goal of Nemo, a mini-ROV, is to have a detailed vision of the areas which are hardly accessible by divers and experts. Particularly the submarine, remotely piloted, has to operate as a robotised camera and be able to scan the wreck inside areas too. The second specification identifies with the very reasonable dimensions of the vehicle and the high control accuracy of its movements in restricted environments. Besides, the ROV must be simple to be driven in order to allow a general user to employ it promptly. The prototype was carried out thanks to the collaboration between the Department of the Earth Sciences and the Mechatronics and Dynamic Modelling Laboratory (MDM Lab) of the Department of Industrial Engineering of the University of Florence (Figure 2.12).

In this brief chapter previously the mechanical and electrical plan of Nemo ROV is shown and subsequently the control architecture of the vehicle is illustrated; the treatment is completed with the results obtained in water, in the swimming pool tests and in the sea.

Figure 2.12: Institutions that developed Nemo ROV

2.3 Theoretical basis

To succeed in piloting a ROV it is necessary to plan a system based on definitions, physical laws and control methods able to guarantee the correct orientation and handling of the underwater robot. Here are introduced the theoretical concepts which are on the basis of propulsion and control system of Nemo ROV.

First of all, as already shown in chapter 1, it is advisable to set out two different reference frames (Figure 2.13):

- "Body frame" O_b-$x_b y_b z_b$, fixed for the ROV as a frame of reference with origin O_b placed in the center of mass of the vehicle, with axes lined up to the axes of the vehicle itself. In particular, x_b axis heads in front of the vehicle, z_b axis is vertical and downward and y_b axis is defined to form a right-handed triplet with the other axes;
- "Fixed frame" O-xyz, inertial frame of reference, defined for the analysing scenario as the frame with origin O in the center of mass of the surface support vehicle and axes lined up with the ones of a NED (North-East-Down) system. More specifically x axis heads north, y axis east and z axis down.

Let's consider the motion study of an underwater vehicle, having six degrees of freedom: six are the coordinates necessary to fix univocally the position and orientation of a rigid body in the space. According to SNAME notation (1950) the following coordinate vectors are fixed:

$$\begin{aligned}
&\vec{\eta} = [\vec{\eta}_1^T\ \vec{\eta}_2^T]^T, && \vec{\eta}_1 = [x\ y\ z]^T, && \vec{\eta}_2 = [\phi\ \theta\ \psi]^T;\\
&\vec{\nu} = [\vec{\nu}_1^T\ \vec{\nu}_2^T]^T, && \vec{\nu}_1 = [u\ v\ w]^T, && \vec{\nu}_2 = [p\ q\ r]^T;\\
&\vec{\tau} = [\vec{\tau}_1^T\ \vec{\tau}_2^T]^T, && \vec{\tau}_1 = [X\ Y\ Z]^T, && \vec{\tau}_2 = [K\ M\ N]^T;
\end{aligned} \tag{2.1}$$

where $\vec{\eta}$ represents the position and orientation vector in fixed frame, $\vec{\nu}$ indicates the linear and angular speeds expressed in body frame and $\vec{\tau}$ identifies forces and moments applied to the vehicle, expressed in body frame. As regards the nomenclature:

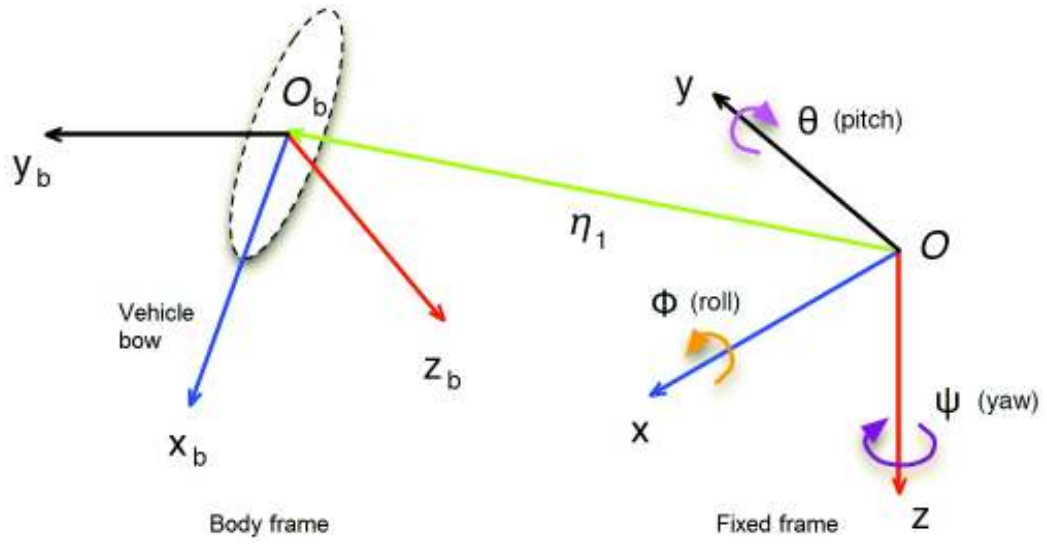

Figure 2.13: Reference frame representation

- ϕ around x axis: roll motion;
- θ around y axis: pitch motion;
- ψ around z axis: yaw motion.

As usual, variables ϕ, θ and ψ correspond to a minimum representation of the orientation through a triplet of Euler angles, expressed in the fixed frame, RPY angles [15].

2.3.1 Equations of motion

The generic motion of a rigid body in an underwater environment [1] can be described in body frame, as a function of the equations of motion (2.1):

$$M\dot{\vec{v}} + C(\vec{v})\vec{v} + D(\vec{v})\vec{v} + \vec{g}(\vec{\eta}) = \vec{\tau},$$

with

- M mass and added mass matrix;
- C matrix considering the centrifugal and Coriolis effects;
- D matrix considering the viscous effects of hydrodynamic damping;
- $\vec{g}$ vector considering the gravity and buoyancy effects.

Considering a typical vehicle activated by propeller engines, vector $\vec{\tau}$ depends on various parameters such as: water density, the length and the diameter of the duct containing

the propeller, the diameter of the propeller itself. For simplicity, it is decomposed into B matrix identifying the position and the orientation of the propellers with respect to the body frame and $\vec{u}$ vector identifying the forces applied by every single propeller along its main axis. Assuming such simplifications [33] the terms of B are constant and depending from the position of the propellers.

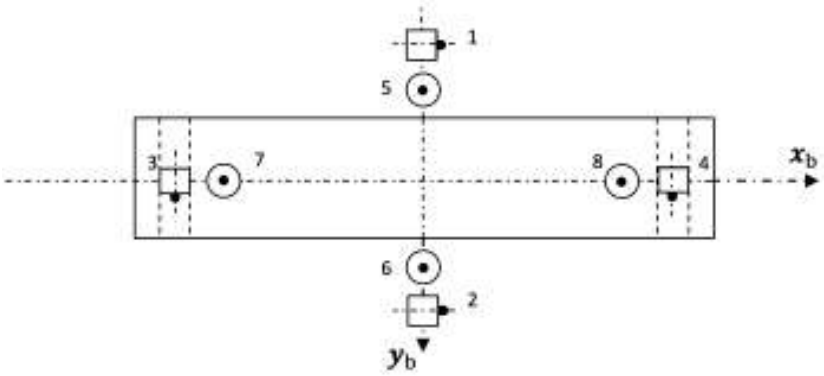

Figure 2.14: Vehicle scheme with 8 propellers: top view

For instance, with a vehicle with 8 propellers placed as in Figure 2.14 the relationship between $\vec{\tau} \in \mathbb{R}^6$ and $\vec{u} \in \mathbb{R}^8$ is the following one:

$$\vec{\tau} = \begin{bmatrix} X \\ Y \\ Z \\ K \\ M \\ N \end{bmatrix} = B\vec{u} = \begin{bmatrix} 1 & 1 & 0 & 0 & 0 & 0 & 0 & 0 \\ 0 & 0 & 1 & 1 & 0 & 0 & 0 & 0 \\ 0 & 0 & 0 & 0 & 1 & 1 & 1 & 1 \\ 0 & 0 & 0 & 0 & l_1 & -l_1 & 0 & 0 \\ 0 & 0 & 0 & 0 & 0 & 0 & -l_2 & l_2 \\ -l_3 & l_3 & l_4 & -l_4 & 0 & 0 & 0 & 0 \end{bmatrix} \begin{bmatrix} u_1 \\ u_2 \\ u_3 \\ u_4 \\ u_5 \\ u_6 \\ u_7 \\ u_8 \end{bmatrix} \tag{2.2}$$

where $B \in \mathbb{R}^{6\times 8}$ is said control matrix of the propellers, l_i with $i = 1,2,3,4$ are the distances of the propeller axes from the origin of the axes. In practice, $\vec{\tau}$ values are calculated by suitable controllers and exploiting (2.2), the thrusts to be given as inputs to the engines are obtained. One of the most used method to control a certain quantity is PID algorithm [1], whose structure is here briefly mentioned.

2.3.2 PID controller

As described in [29], the structure of a PID is introduced on the basis of empirical considerations according to which it is advisable $\vec{\tau}_c$ control variable is produced as the sum of three contributions:

- the first one is proportional to $\vec{e}$ error, defined by the difference between $\vec{\eta}_d$ reference signal and $\vec{\eta}$ output variable of the controlled system;
- the second one is proportional to $\vec{e}$ time integral and is required to have the error cancelled asymptomatically with respect to constant reference signals or constant additive disturbances;
- the third is proportional to $\vec{e}$ time derivative and has the aim to try to "advance" the trend of the error.

Most of ROV systems [1] use PID SISO controllers (Single-Input Single-Output) where every regulator is planned for the control of just one degree of freedom of the vehicle. This fact involves K_p, K_i and K_d in the law

$$\vec{\tau}_c = K_p\,\vec{e}(t) + K_i \int_{t_0}^{t} \vec{e}(x)\,dx + K_d\,\dot{\vec{e}}(t) \tag{2.3}$$

are chosen positive and diagonal. The vector of forces and torques in the body frame is consequently calculated by the relationship:

$$\vec{\tau} = J^T(\vec{\eta}_2)\,\vec{\tau}_c + \vec{g}(\vec{\eta}) \tag{2.4}$$

where $J(\vec{\eta}_2)$ is the matrix defined by

$$J(\vec{\eta}_2) = \begin{bmatrix} \mathrm{c}\psi\mathrm{c}\theta & -\mathrm{s}\psi\mathrm{c}\phi + \mathrm{c}\psi\mathrm{s}\theta\mathrm{s}\phi & \mathrm{s}\psi\mathrm{s}\phi + \mathrm{c}\psi\mathrm{c}\phi\mathrm{s}\theta & & \\ \mathrm{s}\psi\mathrm{c}\theta & \mathrm{c}\psi\mathrm{c}\phi + \mathrm{s}\phi\mathrm{s}\theta\mathrm{s}\psi & -\mathrm{c}\psi\mathrm{s}\phi + \mathrm{s}\theta\mathrm{s}\psi\mathrm{c}\phi & \mathbf{0}_{3\times3} & \\ -\mathrm{s}\theta & \mathrm{c}\theta\mathrm{s}\phi & \mathrm{c}\theta\mathrm{c}\phi & & \\ & & & 1 & \mathrm{s}\phi\mathrm{t}\theta \quad \mathrm{c}\phi\mathrm{t}\theta \\ & \mathbf{0}_{3\times3} & & 0 & \mathrm{c}\phi \quad -\mathrm{s}\phi \\ & & & 0 & \mathrm{s}\phi/\mathrm{c}\theta \quad \mathrm{c}\phi/\mathrm{c}\theta \end{bmatrix}$$

with $\mathrm{s}\cdot = \sin(\cdot)$, $\mathrm{c}\cdot = \cos(\cdot)$ and $\mathrm{t}\cdot = \tan(\cdot)$.

The control law (2.3) allows to separately deal with each degree of freedom of the vehicle, which this way will be ruled by the scalar relationship:

$$\tau_c(t) = k_p e(t) + k_i \int_{t_0}^{t} e(x)\,dx + k_d \frac{d\,e(t)}{d\,t}, \tag{2.5}$$

where k_p, k_i and k_d are positive constants.

k_p coefficient is said coefficient of the proportional action, while k_i and k_d are respectively the coefficient of the integral action and the derivative action. The PIDs, at least in their ideal form, are dynamic linear systems, stationary at continuous time. Using the

Laplace transform at (2.5) with $t_0 = 0$, it is possible to gather they are described by the transfer function

$$R_{PID}(s) = k_p + \frac{k_i}{s} + k_d s \tag{2.6}$$

where the proportional term ($R_P = k_p$), the integral one ($R_I(s) = k_i/s$) and the derivative one ($R_D(s) = k_d s$) are identified. A different representation of the PIDs, probably more used than (2.6), is given by:

$$R_{PID}(s) = k_p(1 + \frac{1}{t_i s} + t_d s)$$

where $t_i = k_p/k_i$ is the integral time and $t_d = k_d/k_p$ is the derivative time.

2.4 Nemo Hardware

The structure and the on board instruments of a ROV deeply vary according to the tasks the vehicle has to carry out: each of these machines is consequently planned for the purpose. In this section the outer structure of Nemo ROV, the sensors, the electrical devices and its connection with the outside are described.

2.4.1 Mechanical structure

Nemo is made up of an aluminium cylindrical body, containing the electronic instruments (Figures 2.15 and 2.16). The central body is closed in the front by a hemispheric cover in transparent plexiglass which guarantees a good visibility for the adjustable camera placed inside.

Figure 2.15: Frontal view of Nemo ROV

Figure 2.16: 3D CAD view

Aft, an Al circular cap, perforated for the cable pass, makes watertight the inboard of the vehicle. Linked to the central body there are four propeller engines for the vehicle motion, four LEDs for the illumination and a safety cage made in Al too. The vehicle dimensions (Figure 2.17 and Figure 2.18) and its weight in air of about 17 kg, define Nemo as a mini-ROV, according to the classification pointed to at the beginning of this chapter.

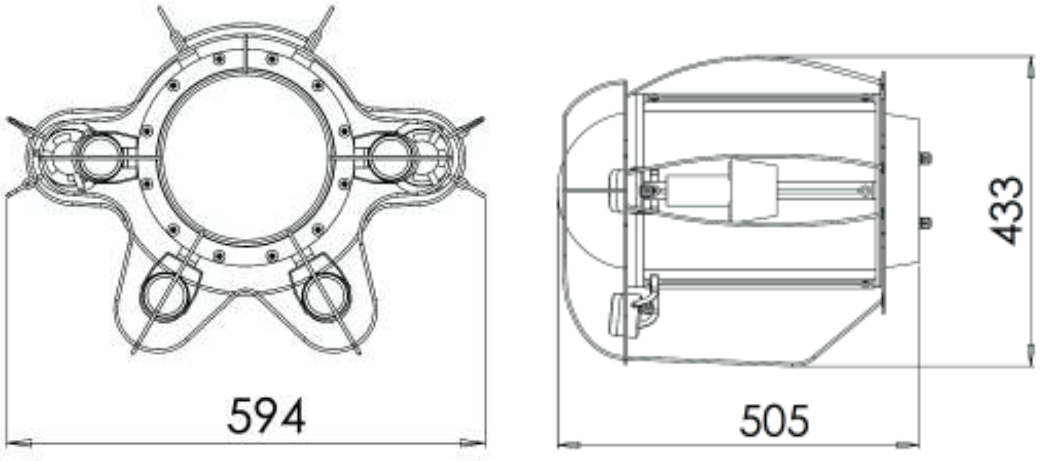

(a) Frontal view (b) Lateral view

Figure 2.17: Frontal and lateral views: sizes in mm

The choice of Al for the vehicle body has been made to guarantee a good structural strength, in order to be able to perform underwater missions in depth; at the same time aluminium guarantees a limited weight compared to materials such as, for example, steel.

Nemo ROV weight (including the payload shipped inside the vehicle) is not totally

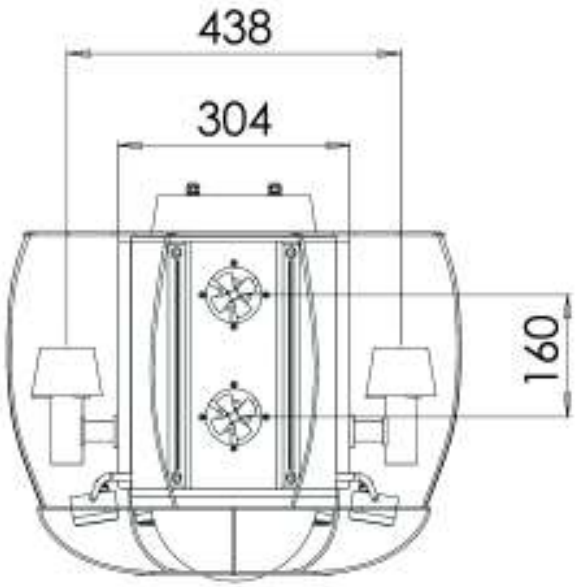

Figure 2.18: Top view: sizes in mm

balanced by the buoyancy in the water, so that Nemo is slightly negative (sinking) with a weight in the water equal about 0.4 kg. Besides it exists a noteworthy difference in longitudinal direction between the position of the center of buoyancy and the one of the center of mass of the system: the frontal cover in plastic material and the Al back cap make the vehicle in the water with a position with raised bow. The correct balance of the vehicle is obtained through small floats and counterweights anchored to the rear of the vehicle and under the front of the vehicle itself. This way the vehicle proves to be statically balanced (null pitch and roll angles) and slightly positive in the water (that is rising out of the water, an important characteristic for rescue in case of emergency).

2.4.2 Propulsion system

The vehicle is moved by 4 electrical propeller actuators (Crustcrawler High Flow 400HFS-L, Figure 2.19) which, considering (2.1), according to Figure 2.20, can be described as follows:

- two side engines S1 and S2 for the main propulsion along x_b and for rotation around z_b (yaw);
- two vertical engines S3 and S4 to control the propulsion along z_b and for rotation round y_b (pitch).

The vehicle is thus under-actuated, as, considering the propeller configuration, it is not possible to let Nemo move along y_b axis, nor to let it rotate around x_b. As regards rolling, the vehicle is made steady, from an hydrostatic point of view, lowering as much

Figure 2.19: Propeller actuators: Crustcrawler High Flow 400HFS-L

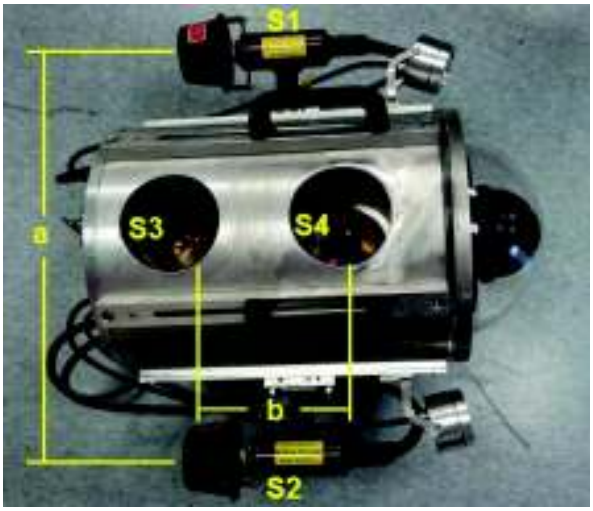

Figure 2.20: Motor positions

as possible the ROV center of mass under its buoyancy center. The engines used in this case are brushless type, they weigh 185 g and absorb 400 W each to the utmost. The thrust provided by the propeller of each engine reaches a maximum of 6.8 kg; considering the dimensions and the inertial characteristics of the vehicle, this value allows Nemo to be reactive enough in its displacements. The three phase current is generated by drivers (Castle Hydra HV-180, Figure 2.21(a)), which need, besides supply, a control signal modulated with the Pulse Width Modulation (PWM) technique. This one is generated by a servo-controller (Pololu Micro Maestro, Figure 2.21(b)) as a function of the desired speed reference for each propeller. Such a device is fed through USB at 5 V and needs a current of 40 mA.

2.4.3 On board instruments

To control the ROV its state has to be known; for instance it is necessary to understand how the vehicle is turned as to a selected reference frame, which depth it is at, and what

(a) Castle Hydra HV-180 driver

(b) Servo controller Pololu Micro Maestro

Figure 2.21: Devices for the motor control

it has in front (e.g. an obstacle). To succeed in satisfying the previous requirements the following devices have been installed on board.

Camera and lights

In the front of Nemo an adjustable camera is housed (Samsung SNP-3120, Figure 2.22) whose images are sent by Ethernet to an outer computer. The camera has its own IP address and the connection with the outer computer, video is displayed with, is put into effect by a device of data switching called switch (Netgear GS105E, Figure 2.23).

Figure 2.22: Videocamera Samsung SNP-3120

The large rotation range (0°...360°), inclination (−5°...185°) and enlargement (12x optical zoom) of the camera allow the operator, piloting the ROV, to have a large visual area, easily explorable without moving the vehicle. The maximum power consumption is 15 W and the supply is directly provided by the network cable through POE (Power Over Ethernet) technology. The switch gets the piece of information given by the camera and sends it to an outer computer; the switch itself gets the control signals for navigation given by

Figure 2.23: Switch Netgear GS105E

the outer computer and addresses them towards the on board computers. To favour the underwater vision in depth too, four LED spots (Bridgelux BXRA-56C2600-B-00, Figure 2.24) have been placed outside the plexiglass cover.

Figure 2.24: Lights: Bridgelux series ES Rectangle Array

Depth sensor

To measure the vehicle depth, a digital pressure transducer (STS DTM, Figure 2.25) has been inserted on Nemo rear cap. This device exploits the piezoresistive effect. Considering Nemo was planned to reach a maximum depth of 40 m, a sensor supporting up to 5 bar, with a maximum absolute error under 5 mbar, has been chosen.

Figure 2.25: Digital pressure transducer STS DTM

Inertial Measurement Unit - IMU

The inertial platform (Xsens MTi, Figure 2.26) is a device made up of a 3D gyroscope, 3D accelerometer and 3D magnetometer furnishing dynamic data at a maximum working frequency of 100 Hz. Such a device is able to detect little orientation variations in a 3D space in a accurate way thanks to an estimate inner owner algorithm.

Figure 2.26: IMU Xsens MTi

Once the device is configured, such a sensor can directly supply $\vec{\eta}_2 = [\phi\ \theta\ \psi]^T$ vector, defined by (2.1) and describing the vehicle orientation in the fixed frame.

On board computer

The on board computer (Raspberry Pi Foundation Raspberry Pi, Figure 2.27) is a single board computer (a calculator implemented on only one electronic card) and even if its dimensions are comparable with a micro-controller ones, its functionalities greatly approach the ones of a classical computer. The reduced dimensions and the reasonable cost make these platforms perfect to be used in vehicles or robots with restricted dimensions.

Figure 2.27: On board computer Raspberry Pi Foundation Raspberry Pi

To control Nemo ROV two on board computers like these are used, communicating each other and named “Pi 1” and “Pi 2”. Such a choice has been suggested by the restricted processing capacitance of a single card, considering the number of devices it has to manage. In particular the first card works with the inertial platform, while the second deals with the servo-controllers, the pressure sensor and the switching on of the LEDs and the motors, using three GPIO (General Purpose Input/Output) pins. The logic inside the ROV is constantly linked to an outer computer through Ethernet protocol: the local network connects the two on board computers, the camera and the outer computer thanks to the switch.

2.4.4 Outer instruments

To be remotely piloted, Nemo needs a power supply and control system which does not limit its navigation and is easy to be managed by the pilot. Here the main outer instruments are listed: they allow to satisfy these needs.

Cable and winder

The connection between the ROV and the outside takes place through the employment of three single cables kept together by insulating tape and little equidistant buoys (Figure 2.28). The two essential cables are the power supply cable, bringing 48 V DC and the Ethernet cable, allowing the transmission of the control signals. The third cable in Dyneema (material with resistance comparable with steel one and excellent to tolerate twists and foldings) is used as rescue and safety cable as it prevents a possible obstacle from cutting the umbilical cord, with the risk of losing of the vehicle. Buoys serve to make the cable approximately neutral inside the water.

Figure 2.28: Nemo wire

The cable houses in a special winder (Figure 2.30); (Figure 2.30(b)) a WiFi access point is fit up on (Ubiquiti Networks PicoStation M2-HP, Figure 2.29) allowing the communication among the devices on Nemo and the ground instrumentation over the air. The access

point lets a more comfortable place for the control instrumentation and allows to uncouple physically the user from the vehicle with a guarantee of a greater standard of safety for the pilot.

Figure 2.29: Access Point WIFI Ubiquiti Networks PicoStation M2-HP

(a) Control unit side (b) Antenna side

Figure 2.30: Winder

The electric energy is generated by an internal combustion engine to which is linked a power feeder supplying 48 V outgoing. The winder gets this tension and feeds Nemo cable and the access point.

Computer and controller

The communication with the ROV takes place through the rugged notebook Dell Latitude e6430 ATG (Figure 2.31(a)) on which runs the software necessary to the execution of the control programs for the vehicle. To give navigation orders the pilot employs an expressly set commercial joypad (Figure 2.31(b)).

(a) Notebook rugged Dell Latitude e6430 ATG

(b) Joypad GameStop

Figure 2.31: Control tools for the user

Finally, to allow to all these devices to work properly, the MDM Lab designed a suitable electrical plant. Here, for reasons of brevity, is only reported the scheme of the connections in Figure 2.32.

2.5 Nemo Control

The software architecture that allows Nemo control is based on the middle-ware MOOS [30]. Each MOOS application is able to communicate with the other programs exploiting a centralized database called MOOSDB: the only aim of MOOSDB is to receive the variable updates and to notify these changes to the subscribed applications. The software architecture is not analysed here in details; in any case, its logic is the same used for Typhoon AUV (see chapter 1) [38].

2.5.1 Control system

To succeed in piloting the vehicle it is necessary to control the four engines in a suitable way. For instance, when the vehicle has to maintain the attitude or a reference depth, it is required a control in closed loop which, on the basis of references and measures of the vehicle state, is able to minimize the errors among these quantities. The used control algorithm is of PID type, as previously mentioned.

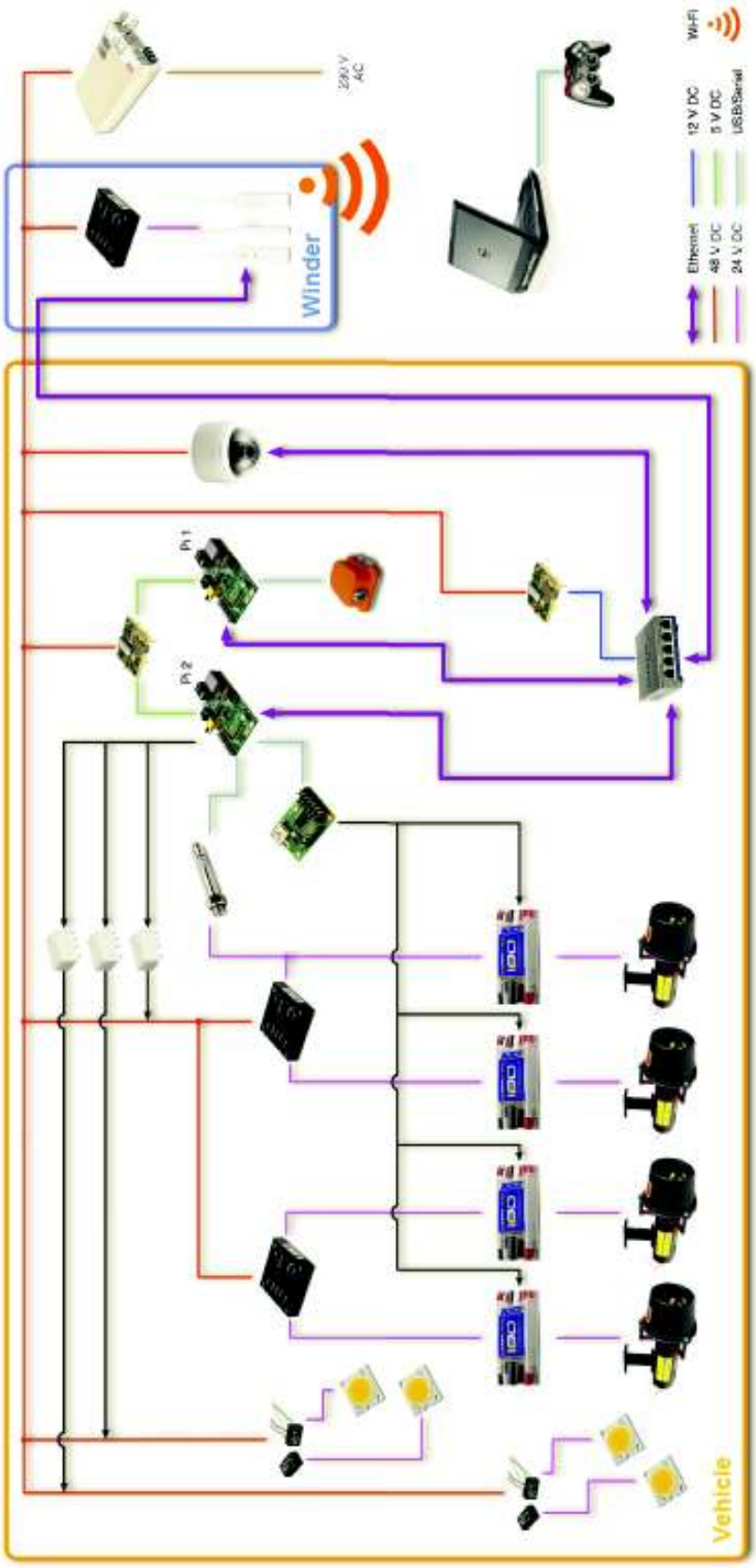

Figure 2.32: Nemo connections

In this application the PIDs to implement are three: one to control the yaw, one for the pitch and one for the depth. In the follow-up, according to the adopted notation, references are indicated by vector $\vec{\eta}_d = [z_d\, \theta_d\, \psi_d]^T$ and the controller gains by k_{ph}, k_{ih}, k_{dh} with $h = z, \theta, \psi$. The controller outputs, once saturated by s_h with $h = z, \theta, \psi$, are indicated by vector, in fixed frame, $\vec{\tau}_c = [\tau_{cx}\, \tau_{cz}\, \tau_{c\theta}\, \tau_{c\psi}]^T$ with $\tau_{cx} = 0$ for every instant of time. The horizontal thrust is not in fact controlled by any PID, but just manually by the user: this fact involves the use of a further vector, $\vec{\tau}_m = [\tau_{mx}\, \tau_{mz}\, \tau_{m\theta}\, \tau_{m\psi}]^T$, indicating the forces and torques expressed in the body frame directly furnished by the pilot. $\tau_{mz}, \tau_{m\theta}, \tau_{m\psi}$ values allow to carry out some tests on engines (without any control action), but in the standard use of the ROV these quantities are null (it is PID aim to regulate the depth, pitch and yaw).

The system outputs are instead represented by $\vec{\eta} = [z\, \theta\, \psi]^T$ with z provided by the pressure sensor and θ and ψ by the inertial platform (IMU). In Figure 2.33 the control scheme is displayed.

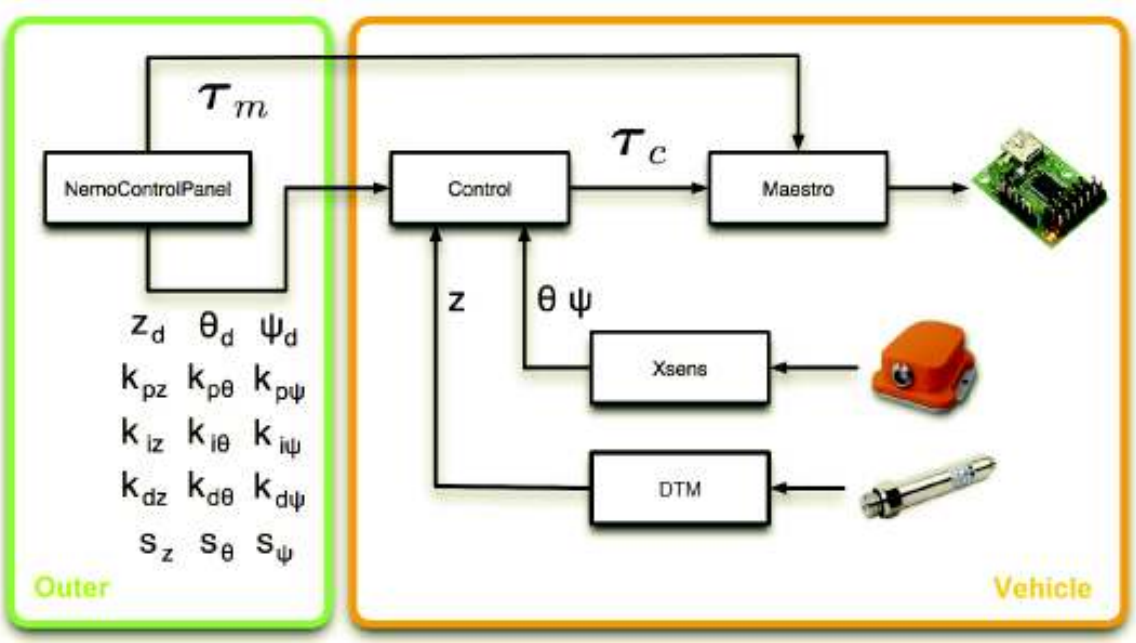

Figure 2.33: Control scheme

- the user sends the system the references, the control parameters and the desired horizontal thrust through the graphic interface ("NemoControlPanel") and the joypad;
- "Control" on the basis of references, the control parameters and estimates provided by the sensors implements the three PIDs;

- "Maestro" exploiting the forces and torques provided by Control and the user (pilot), calculates the thrust values to send to the servo-controller.

Control

Control application implements PIDs controllers governing the depth and the vehicle orientation: at every time step, on the basis of references, of measured outputs and control parameters, this application calculates the forces and torques needed for the control (Figure 2.34). The implementations of MOOS functions are described as follows:

- OnStartUp() initializes the three controllers with predetermined parameters and makes the variable updates θ, ψ and z by Xsens and DTM, and also the reference updates $\vec{\eta}_d$ and PID values k_{ph}, k_{ih}, k_{dh}, s_h, with $h = z, \theta, \psi$ by the graphic interface;

- OnNewMail() takes care of memorizing references and the present values of the three quantities to be regulated;

- Iterate() calculates the errors between the reference and the present value of each quantity and passes them to the implemented PID algorithms. The three results are memorized in $\vec{\tau}_c$ and published on MOOSDB.

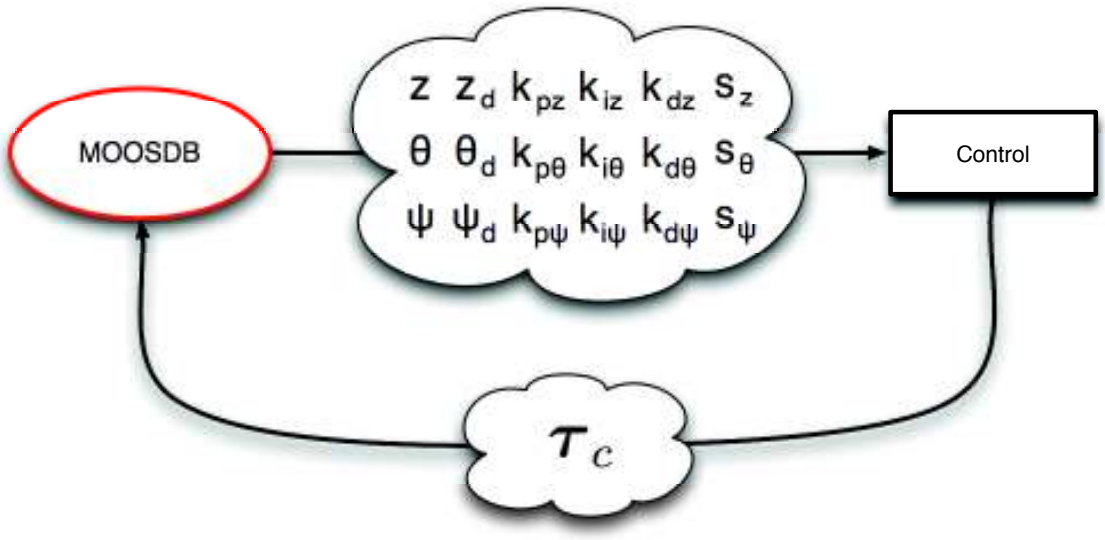

Figure 2.34: Control working scheme

Maestro

Maestro application is in charge of the computation of the thrust values of each propeller, to generate afterwards the commands to send to the drivers of each motor. The processing is put into effect considering such an order is of PWM type. As it has already been mentioned, Nemo is under-actuated and has got 4 degrees of freedom (Figure 2.35): Y force and K torque cannot be applied to the vehicle and therefore the ROV cannot either move along y_b direction or control the roll. The residual degrees of freedom are piloted considering $\vec{\tau}_c$ and $\vec{\tau}_m$ contributions respectively provided by the PIDs and the user (through the joypad or the graphic interface).

$$\vec{\tau}_c = \begin{bmatrix} 0 \\ \tau_{cz} \\ \tau_{c\theta} \\ \tau_{c\psi} \end{bmatrix}, \qquad \vec{\tau}_m = \begin{bmatrix} \tau_{mx} \\ \tau_{mz} \\ \tau_{m\theta} \\ \tau_{m\psi} \end{bmatrix} \tag{2.7}$$

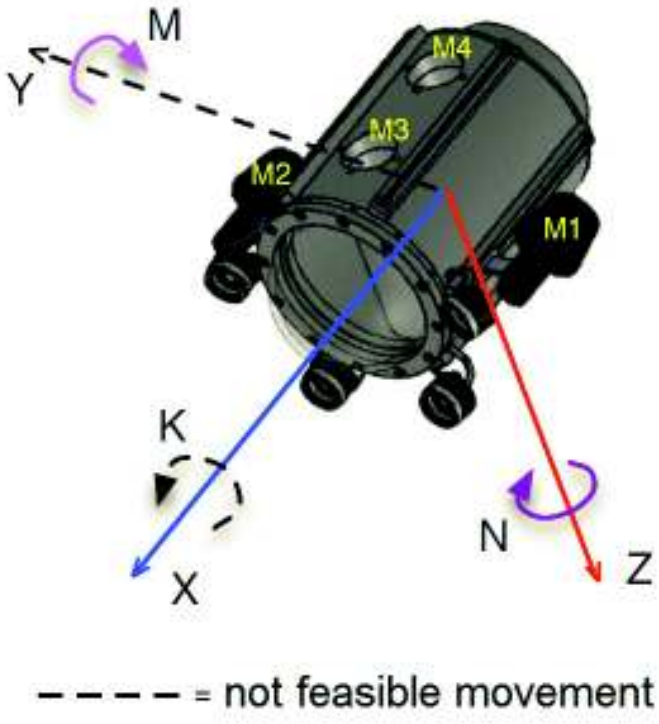

Figure 2.35: Forces and torques applied to the vehicle

Particularly, in accordance with (2.4), Maestro application previously originates the

vector

$$\vec{\tau} = \begin{bmatrix} X \\ Z \\ M \\ N \end{bmatrix} = J^T(\vec{\eta}_2)\,\vec{\tau}_c + \vec{\tau}_m + \vec{g}(\vec{\eta})$$

to bring all forces and torques in the body (mobile) frame and then calculates, inverting the relationship

$$\vec{\tau} = B\vec{u} = \begin{bmatrix} 1 & 1 & 0 & 0 \\ 0 & 0 & 1 & 1 \\ 0 & 0 & -l_2 & l_2 \\ -l_1 & l_1 & 0 & 0 \end{bmatrix} \begin{bmatrix} u_1 \\ u_2 \\ u_3 \\ u_4 \end{bmatrix}$$

the thrusts to provide to the single motors:

$$\begin{aligned} u_1 &= \frac{X}{2} - \frac{N}{2\,l_1} + 0.6\,\mathrm{sgn}\left(\frac{X}{2} - \frac{N}{2\,l_1}\right); \\ u_2 &= \frac{X}{2} + \frac{N}{2\,l_1} + 0.6\,\mathrm{sgn}\left(\frac{X}{2} + \frac{N}{2\,l_1}\right); \\ u_3 &= \frac{Z}{2} + \frac{M}{2\,l_2} + 0.6\,\mathrm{sgn}\left(\frac{Z}{2} + \frac{M}{2\,l_2}\right); \\ u_4 &= \frac{Z}{2} - \frac{M}{2\,l_2} + 0.6\,\mathrm{sgn}\left(\frac{Z}{2} - \frac{M}{2\,l_2}\right); \end{aligned} \tag{2.8}$$

where

$$l_1 = \frac{a}{2};$$

$$l_2 = \frac{b}{2};$$

with $a = 0.44$ and $b = 0.16$ representing the distances in meters respectively among S1, S2 and S3, S4 motors (Figure 2.18).

As regards the contribution made by $0.6\,\mathrm{sgn}(\cdot)$ function in (2.8), this one adds or subtracts 0.6 to each thrust in order to reduce the effect of the dead zone, every engine is subjected to when the reference is near zero. As last processing, u_i values with $i = 1,2,3,4$ are formatted according to the coding of the servo controller and sent to the device and to MOOSDB under the name of *targetSh*, with $h = 1,2,3,4$.

Maestro appliance, having to act just with an outer control command (Figure 2.36), does not need an implementation of the Iterate function. Data which are notified on

MOOSDB by Maestro will be used by the graphic interface to point out, on a dynamic pattern the engine currently in motion.

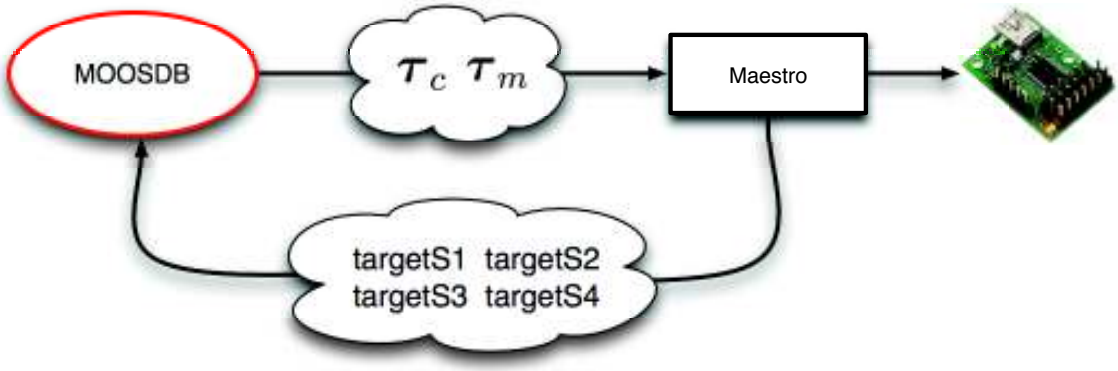

Figure 2.36: Maestro working scheme

2.5.2 Graphic interface

Once described the programs working with the vehicle management, it is worth to explain how the user can interact with the programs themselves to steer the ROV in a more intuitive and simpler way. Consequently it is essential an interface allowing to show the pilot the vehicle state and send the commands enabling to manoeuvre all the actuated degrees of freedom of the system. In this section *NemoControlPanel* application will be described, developed with Qt and integrated with MOOS. The main window of NemoControlPanel is organized with three different "graphic panels":

- *Controls*, allowing to tune the control parameters of the system (conceived for testing phases);
- *Diagrams*, allowing to display in real time the trend of the controlled quantities, proves to be very useful to understand which control parameters to act on to improve the response of the system;
- *Navigation*, used to pilot the vehicle, contains all instruments useful to the user to control Nemo ROV.

Besides, is it possible to notify on MOOSDB the following variables:

- $\vec{\tau}_m$ to manually provide the forces and torques to Maestro process;
- h_d, k_{ph}, k_{ih}, k_{dh}, s_h with $h = \theta, \psi, z$ to control respectively pitch, yaw and depth;

- *ledAbove, ledBelow* to switch on/switch off the upper/lower lights and *power* to feed or not feed the engines.

The application working principle is summarized in Figure 2.37.

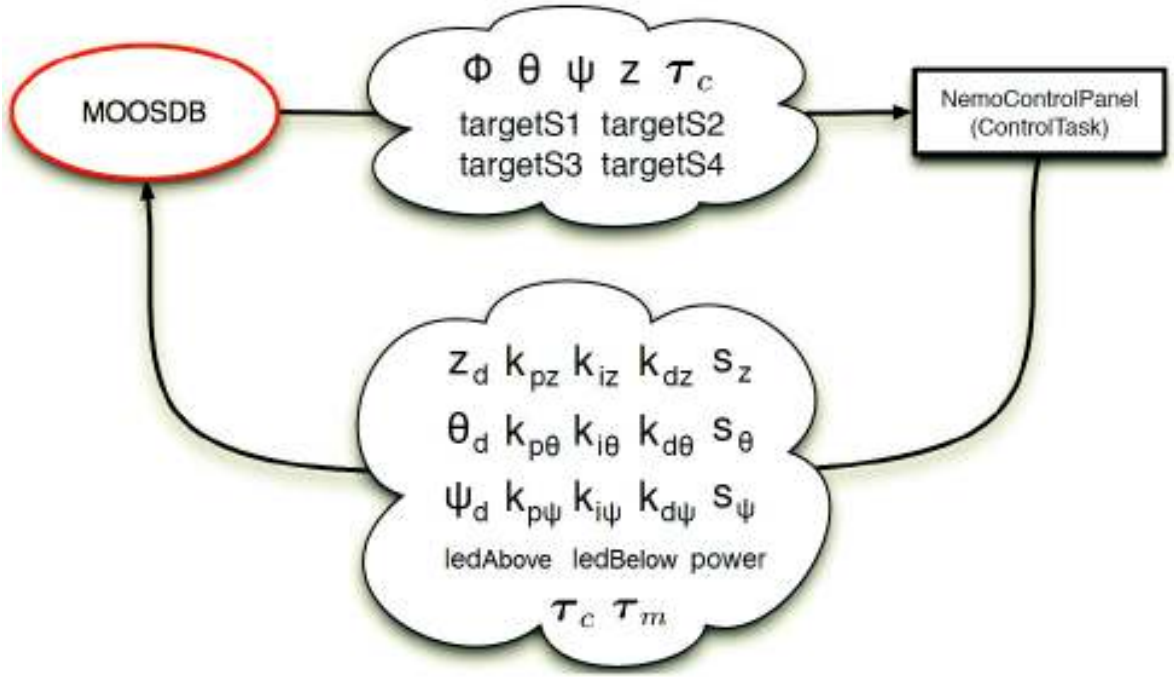

Figure 2.37: ControlTask working principle

Controller management

Joystick class manages the communication with the joypad, the USB device linked to the computer on which runs NemoControlPanel, used to give the main navigation orders. The actions performed through the joypad are mapped according to the scheme of Figure 2.38. In accordance with such an illustration, pressing select key, the video camera control mode is activated, transforming properly the orders on the joypad.

The basic orders to give to the vehicle are the motor switch on, the control of the longitudinal thrust and the references of yaw, and depth. In particular, with reference to Figure 2.38, switching on and off take place through start key while thrust and references are commanded by A1 and A2 analogue levers. In correspondence of the displacement of one of these levers, the program receives a value included between zero and a maximum value (32767) as a function of the motion entity, which is used in proportional way to generate a reference value for the above-mentioned quantities.

The value of the advance thrust is moreover multiplied for a set scalar, pressing Pn with $n = 1,2,3,4$ buttons, allowing the pilot to send backwards or forwards the vehicle at four different speeds. Analogously the speed of the yaw reference can be increased or

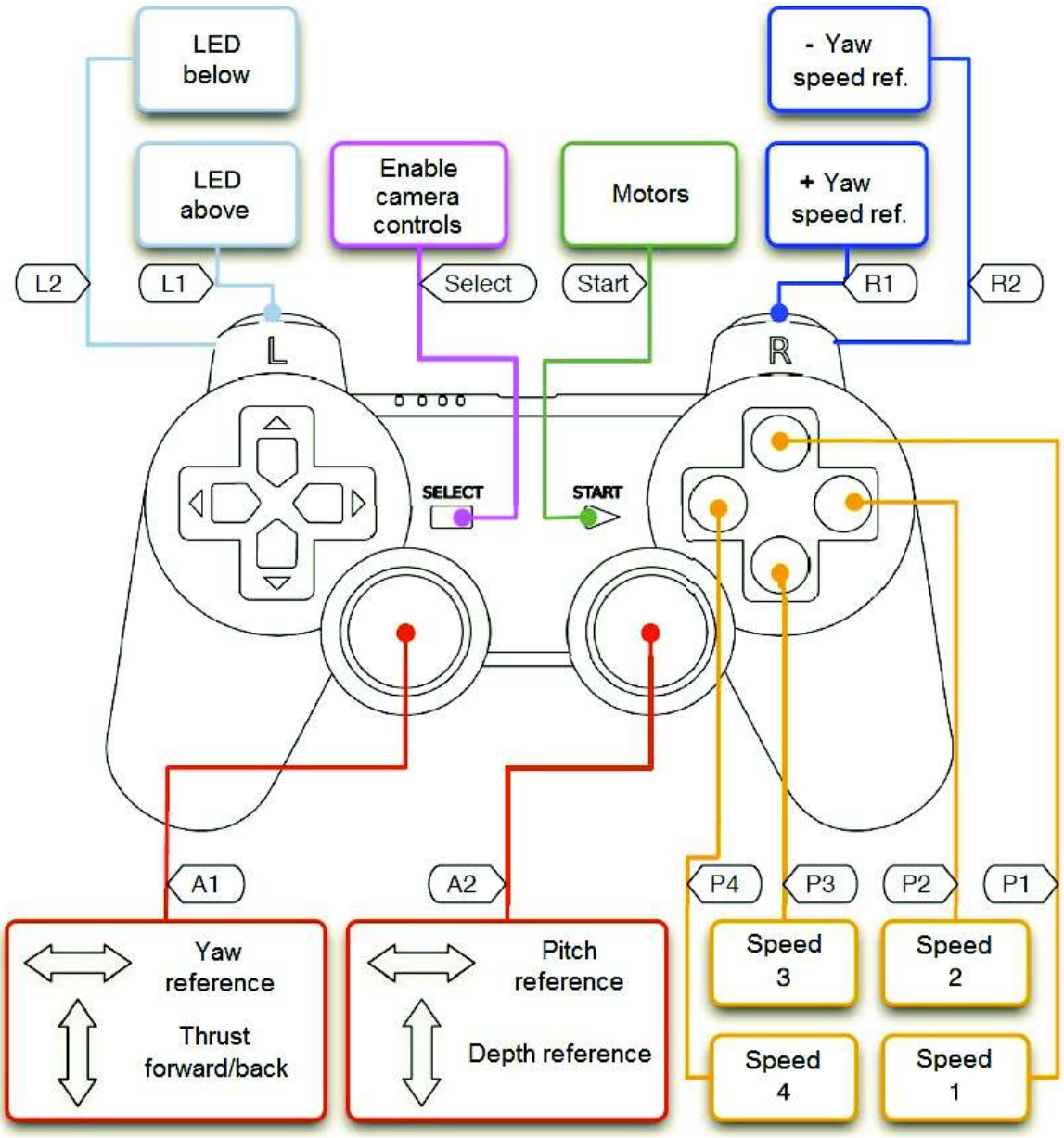

Figure 2.38: Joypad commands: navigation mode

slowed down acting on R1 and R2 keys. The upper and lower lights can be switched on (or off) respectively by pressing L1 and L2.

Controls and diagrams

As it has already been advanced, to let the user pilot in the best possible way the device, the control parameters need to be tuned. This is an operation which should take place in a controlled environment, where it may be possible to monitor accurately the vehicle behaviour; the tuning procedure, when it is ended, has to guarantee such a controllability of the vehicle to allow, not trained people either, to pilot Nemo ROV simply.

The control interface (Figure 2.39) shows on the left the three parameter groups modifying the controllers. At every change of the user taking place through slider or text field, the set value is notified on MOOSDB allowing Control to update the parameters. Once the optimum values have been set out, they can be saved: these parameters will be available for the future executions of the program, it will be sure enough to press on "Carica parametri" to recover them.

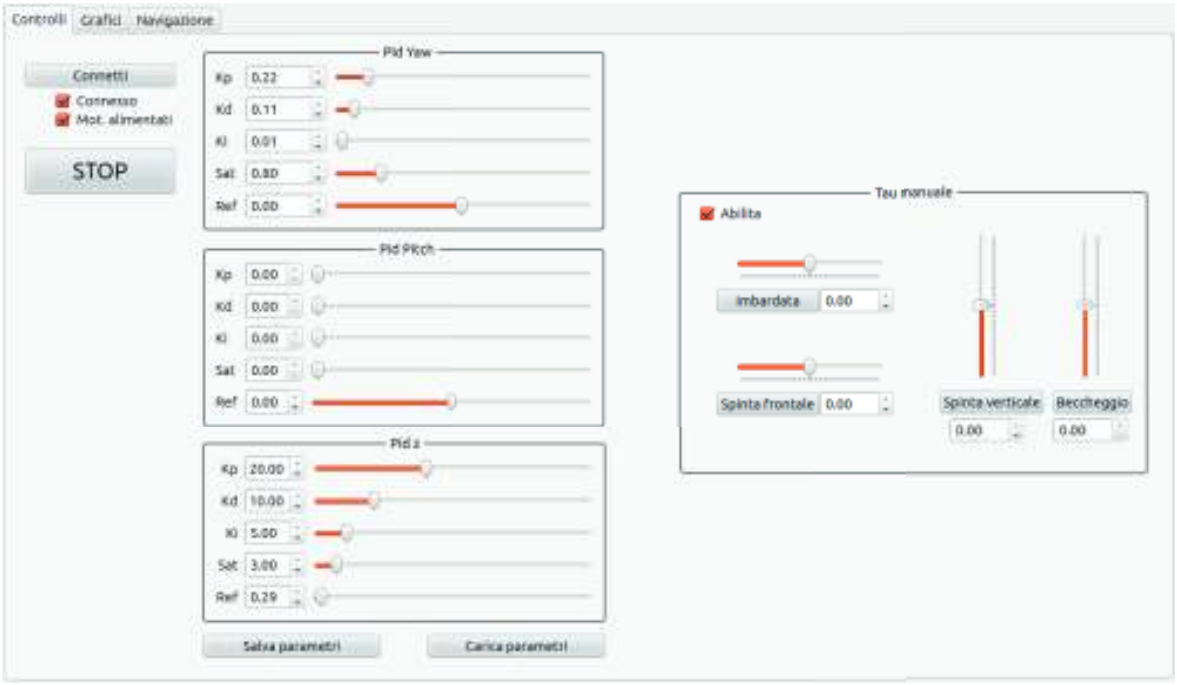

Figure 2.39: Control interface

On the right side it is possible to set $\vec{\tau}_m$ values, particularly "Spinta frontale" reflects the input given by the joypad while the other values are on the contrary modifiable only by the slider and prove to be useful to test engines, without any kind of control. As regards Diagrams interface (Figure 2.40), this makes at disposal 2D dynamic diagrams. At every time, ψ, θ, z values are passed to the objects in charge of drawing points on the related diagrams, enabling an immediate display of these three quantities.

Navigation

The main graphic part is represented by Navigation interface. If calibration has been carried out, the user will be able to pilot the vehicle without ever changing interface. This one is represented in Figure 2.41.

Video camera class takes care of managing all operations concerning video reproduction and camera handling. Movements the device can make are pan, tilt and zoom (ptz camera). In Figure 2.42 pan and tilt rotations are depicted: to make a displacement towards a direction it is necessary to combine the directions as a function of the current

Figure 2.40: Diagrams interface

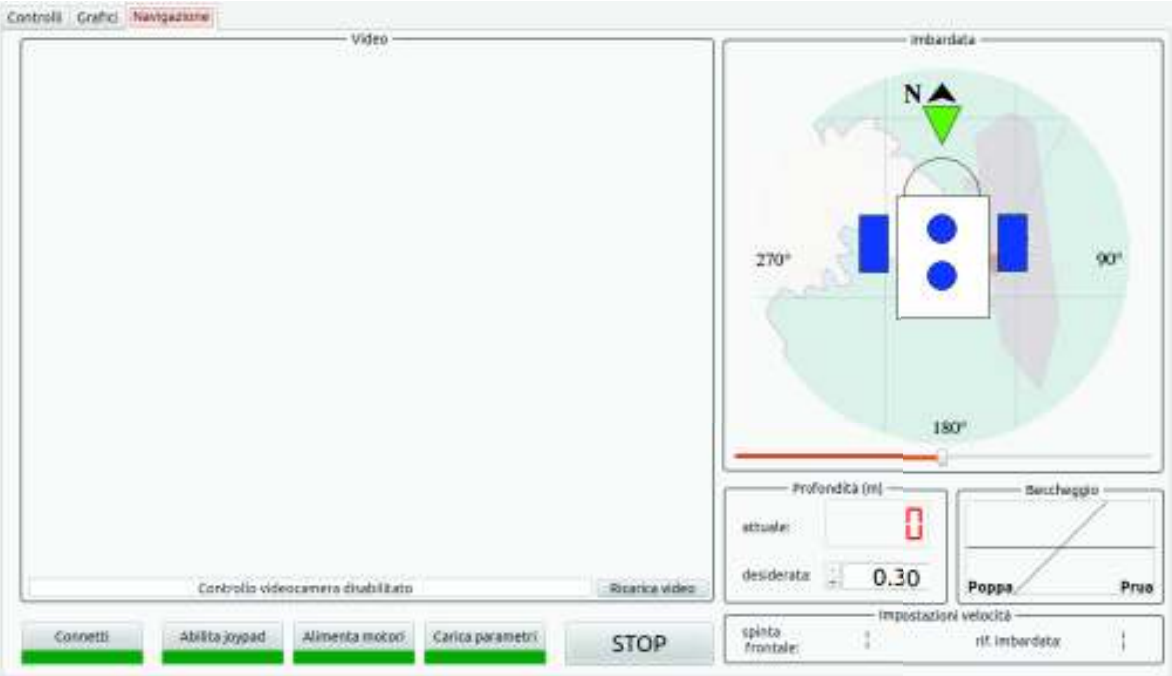

Figure 2.41: Navigation interface

position. To get an intuitive control on the part of the user it is consequently necessary to make a processing of the orders he gives.

In particular, when the user wants to look towards a desired direction, he will just press the desired button: the camera will move directly to the previously recorded position and the software will be in charge of rotating the screen in the correct way. Zoom

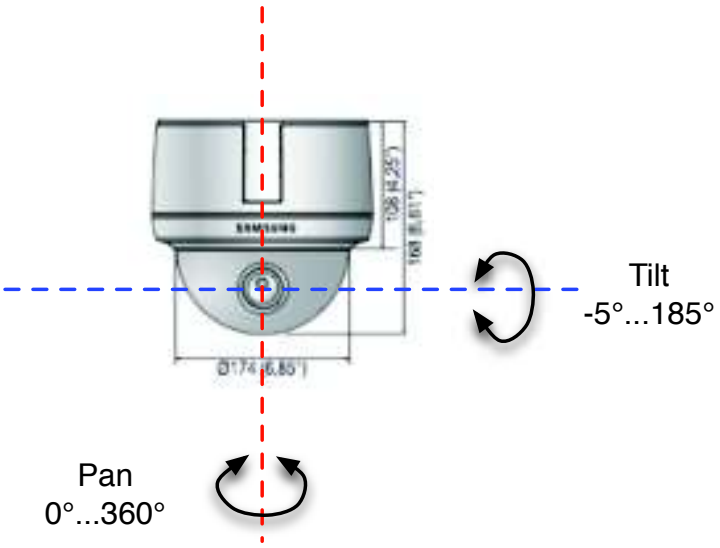

Figure 2.42: Pan and tilt

motions can be operated by R1 and R2 buttons to complete the camera control. The system that has just been described allows the pilot to check easily a large area in front of the vehicle, without moving the vehicle itself. The immediacy and accuracy of this system has eliminated the necessity of control on pitch, rather difficult, as it will be shown in the following chapter, considering the proximity between the two vertical motors (restricting the related control torque).

A video camera object is created at the program start over and if the connection with the vehicle is active, the stream is shown in the video area (Figure 2.43).

Yaw, pitch and depth indicators

To show the pilot the state of the controlled quantities, some special provided classes have been created. YawViewer and PitchViewer classes are in charge of representing on the navigation interface the diagrams depicting the yaw and the pitch state of the vehicle.

In particular YawViewer shows a diagram which, besides portraying at every instant the vehicle yaw, shows the references the pilot is furnishing (green triangle). ψ yaw value is given by Xsens program, which at every time step publishes it on MOOSDB; ψ_d yaw reference is on the contrary sent by the joypad, memorized in NemoControlPanel and made public on MOOSDB. The vehicle structure is schematized but it enables to immediately recognize the bow (hemispheric part), the stern and the engines (blue coloured). The engine colour is updated dynamically: at every command asking for a displacement, the correspondent engine is red coloured. The result can be noted in Figure 2.45: such a graphic solution proves to be very easy to verify the thrusts provided by the engines.

Under the panel there is a bar enabling to rotate the whole drawing: at the switching

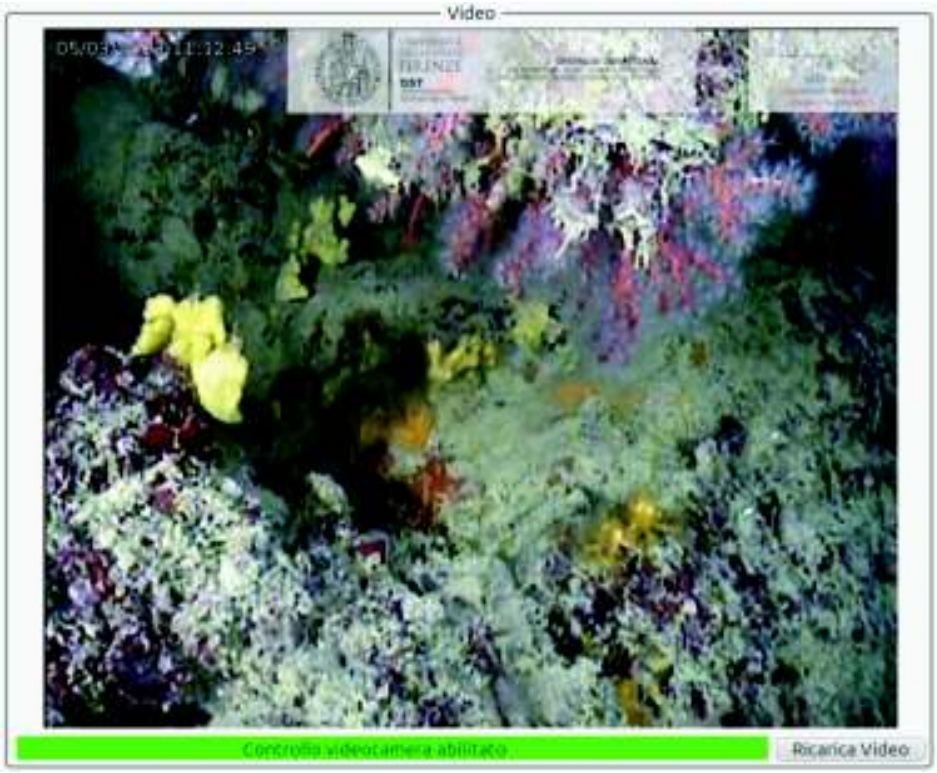

Figure 2.43: Video during one Nemo ROV mission

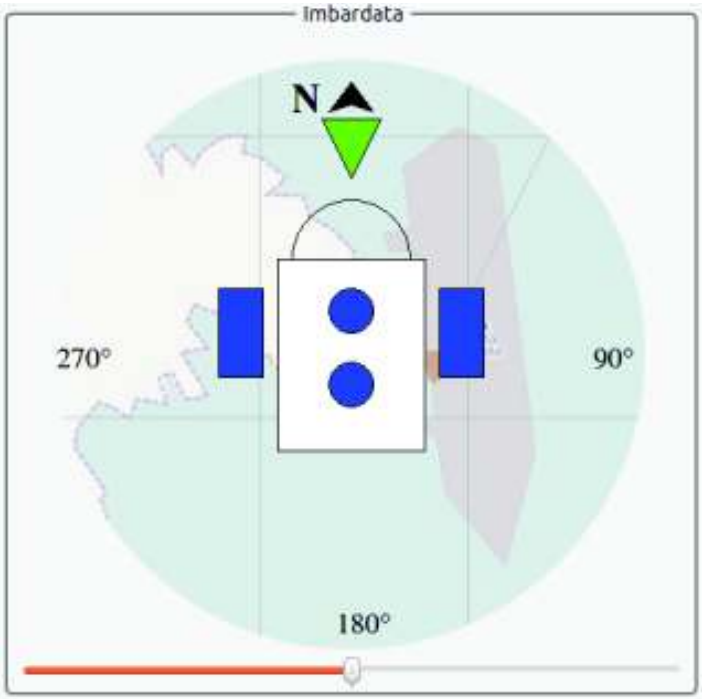

Figure 2.44: Yaw indicator

on time the vehicle takes up position towards the local north. Consequently to line up the pilot orientation with the vehicle one it is essential to turn the drawing to the point where the two systems coincide.

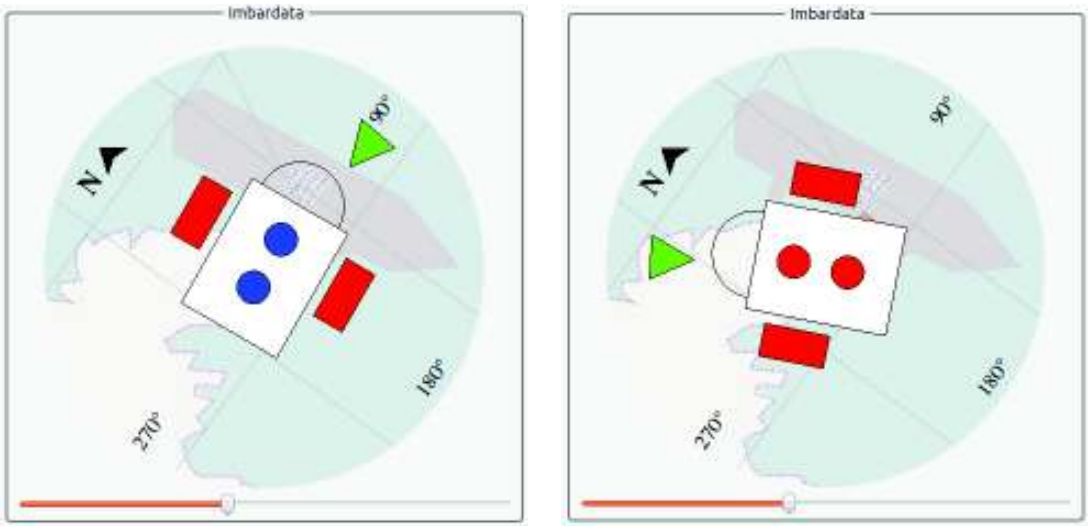

(a) Horizontal motors in operation (b) Horizontal and vertical motors in operation

Figure 2.45: Yaw reference following and motors operating

As regards PitchViewer class, having fixed not to control the pitch, this class is restricted to picture graphically the value of θ variable. Particularly, negative values indicate a state where the vehicle has its bow facing down and vice versa, see Figure 2.46; the null value coincides with a perfectly balanced situation.

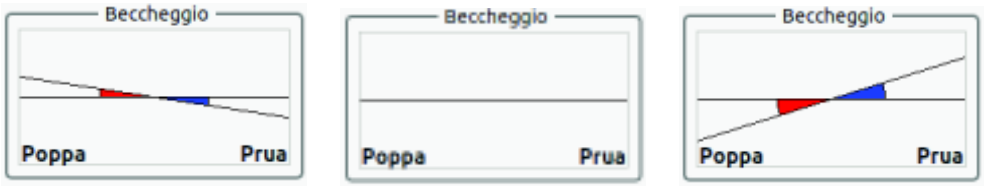

(a) Bow pointing down (b) Vehicle in the horizontal plane (c) Bow pointing up

Figure 2.46: Pitch representation

As regards depth visualization and depth setting, a specific class is in charge of reading z variable from MOOSDB and screen printing it using a simple numeric indicator. A modifiable numeric field is on the contrary in charge of displaying the present reference, allowing in case its modification by the user (in practice, using the joypad right lever).

In the video bottom area, are placed controls to enable navigation (Figure 2.48). "Connetti" button starts out MOOS Appliance and allows diagrams. After connection, YawViewer and PitchViewer show the vehicle state.

"Abilita joypad" button puts into execution the thread allowing to manage the controller events and disables other possible piloting devices (e.g. a tablet). "Alimenta motori" (which can be activated through joypad start key too) enables to modify the power

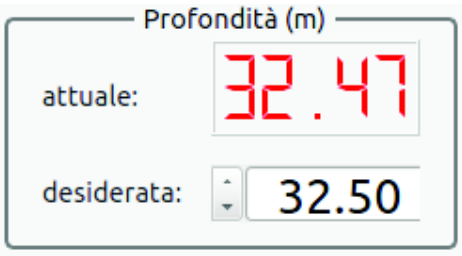

Figure 2.47: Depth indicator

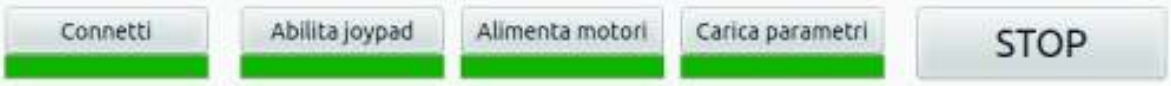

Figure 2.48: Command panel, initial button and indicator states

variable on MOOSDB: GPIO on board program enables the corresponding output by feeding this way the motors and the pressure sensor.

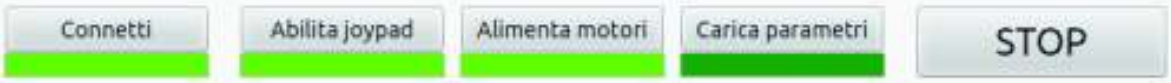

Figure 2.49: Command panel, system ready for the loading of the controlo parameters

The interface now shows (Figure 2.49) all information useful for navigation: just control parameters have to be loaded. When the button "Carica parametri" is pressed, the control parameters loaded by database will be provided to MOOSDB and so to Control, which will be in charge of calculating forces and torques able to make the vehicle follow the desired references. It is important this last operation is effected only when Nemo ROV is in the water considering the propellers will immediately try to bring the vehicle to the desired state. Besides "Carica parametri" button has not got any effect if engines have not been fed before: otherwise, at the switch on moment motors would find thrust orders different from zero and be locked.

"Stop" button is a safety one: it brings power variable to 0, disables control parameters, "Abilita joypad", "Alimenta motori", "Carica parametri" buttons, cutting off power supply to the motors and forbidding all operations which might start up the vehicle again. Unlike the other buttons, this is held pressed (Figure 2.50); until it is not clicked again, this situation is unchanged.

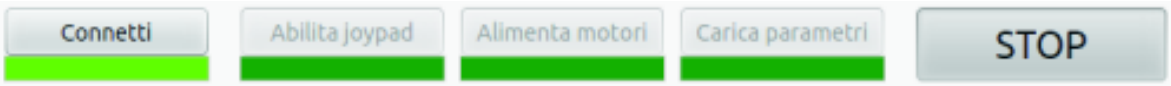

Figure 2.50: Command panel, "STOP" button pressed

When it is released (Figure 2.51), the vehicle state does not change but the panel buttons revert to be clicked, enabling the user to take the control again.

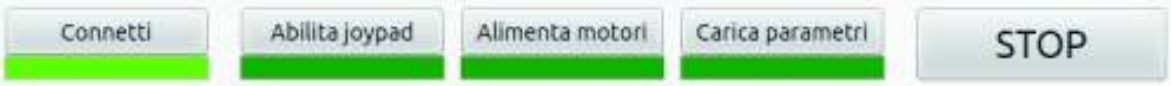

Figure 2.51: Command panel, "STOP" button released

2.6 Tests in water

In this section the calibration procedure of the PID controller parameters will be described and the experimental results obtained during a mission in the sea will be illustrated.

2.6.1 Parameter calibration

After describing the PID structure, it is obvious the performances of these controllers are based on the choice of k_p, k_i and k_d parameters. To define the triplets suitable for the best performance, several tests in the MDM Lab swimming pool (Figure 2.52) have been carried out. These tests evaluated of the vehicle response to sudden reference change, that is assessing the response to the step.

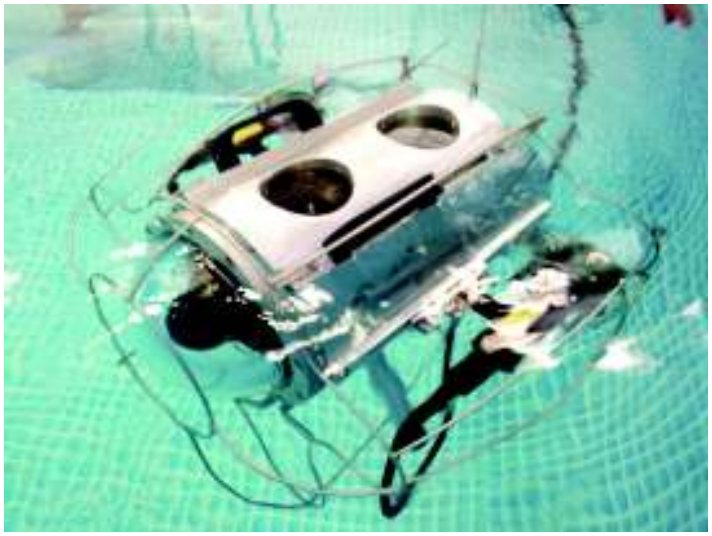

Figure 2.52: Nemo ROV inside the swimming pool of the MDM Lab

As starting point, Ziegler-Nichols method [37] have been followed, identifying k_c critical gain leading the system to reply to a reference change with a continuous oscillation of T_c period.

Yaw and depth

As regards the PID tuning for the yaw, $k_{c\psi} = 0.55$ critical gain leads to an oscillation period $T_{c\psi} = 5$ s, as it is evident in Figure 2.53.

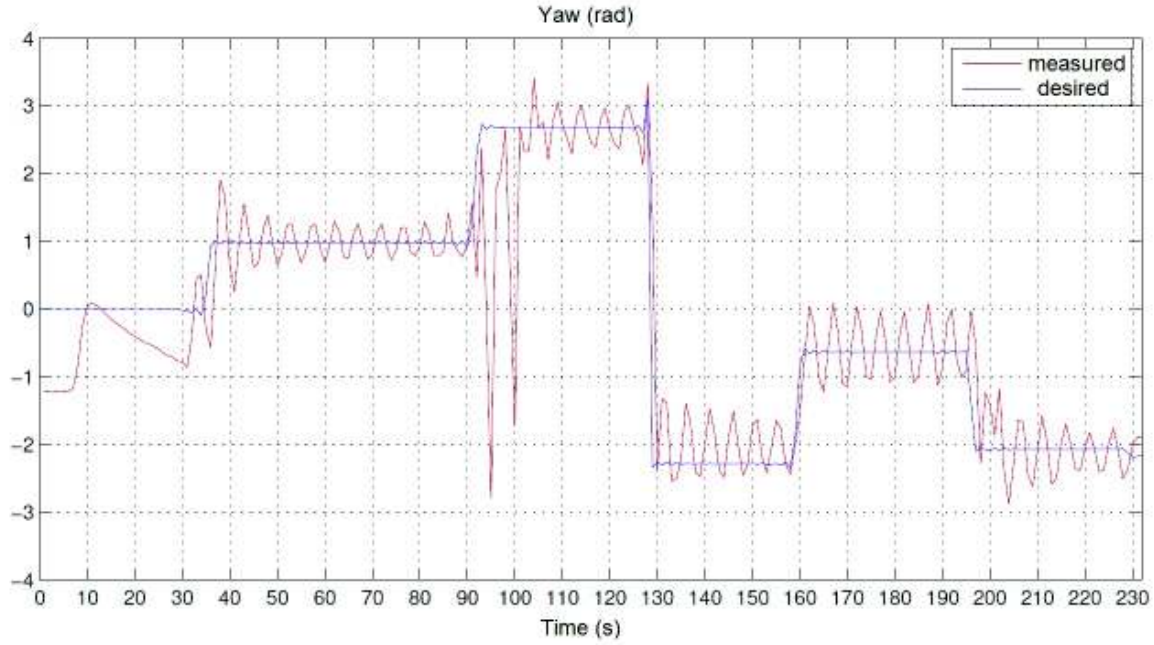

Figure 2.53: System response to step variations with $k_{p\psi} = 0.55$, $k_{i\psi} = 0$, $k_{d\psi} = 0$

Following the rules of Ziegler-Nichols method, $k_{p\psi} = 0.33$, $k_{i\psi} = 0.13$, $k_{d\psi} = 0.21$ are obtained, with the system response shown in Figure 2.54.

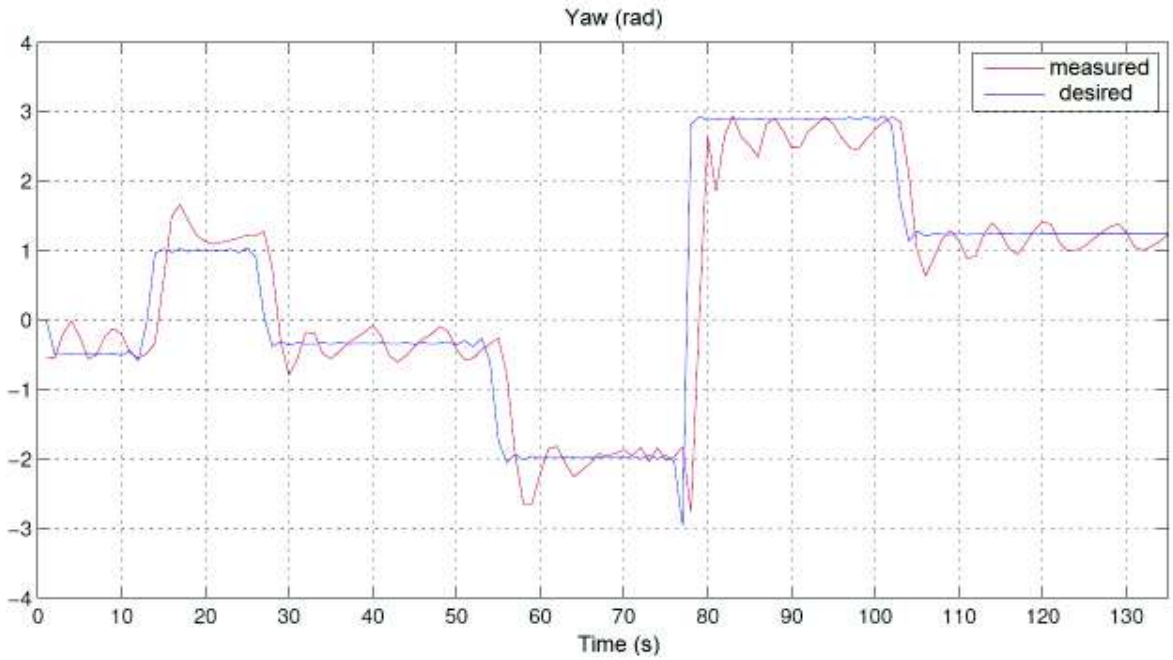

Figure 2.54: System response to step variations with $k_{p\psi} = 0.33$, $k_{i\psi} = 0.13$, $k_{d\psi} = 0.21$

Starting from this response, still too oscillatory, several tests have been carried out to improve the settlement time and the overshoot. Especially, all gains have been gradually lowered as far as to obtain the reply of Figure 2.55.

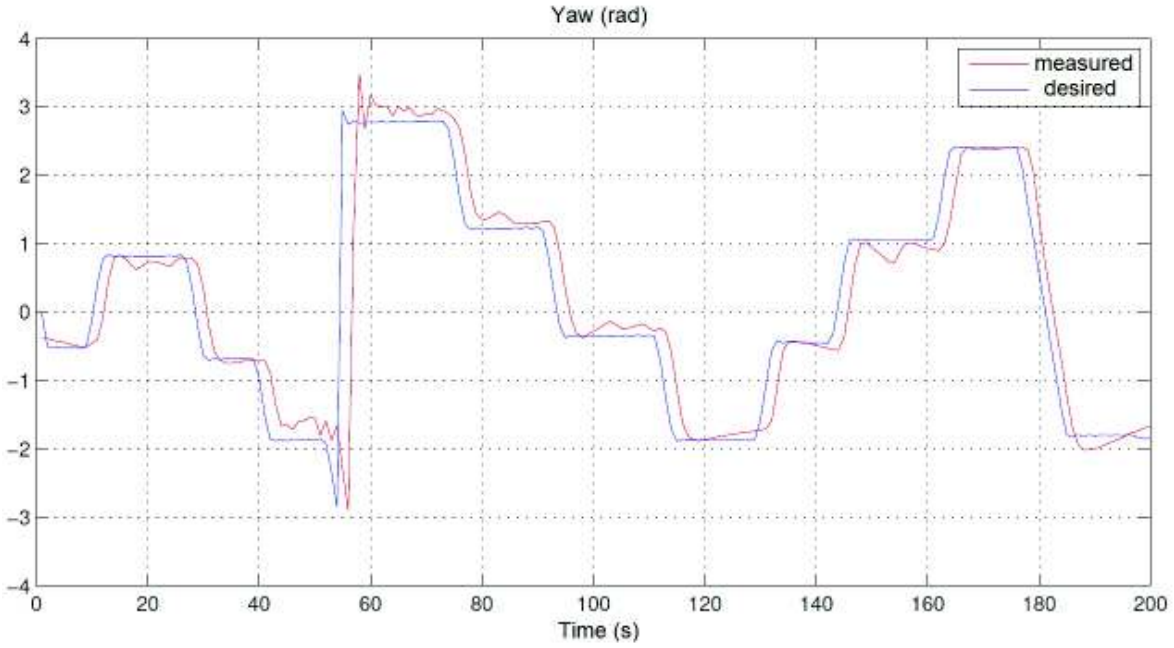

Figure 2.55: System response to step variations with $k_{p\psi} = 0.22,\ k_{i\psi} = 0.01,\ k_{d\psi} = 0.11$

For depth control the same process has been followed, identifying initially $k_{cz} = 50$ critical gain and consequently $T_{cz} = 6$ s (Figure 2.56).

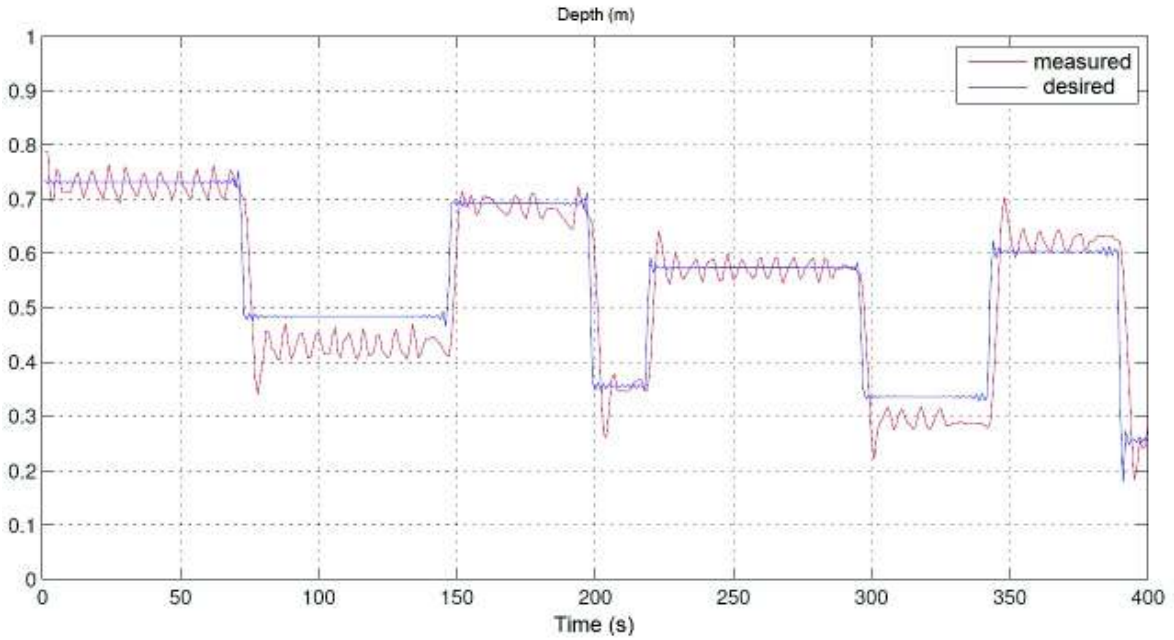

Figure 2.56: System response to step variations with $k_{pz} = 50,\ k_{iz} = 0,\ k_{dz} = 0$

The system response with Ziegler-Nichols parameters is shown in Figure 2.57.

Such a behaviour already results rather satisfactory, but to damp down oscillations further on, the various parameters have been lowered arriving at the reply of Figure 2.58.

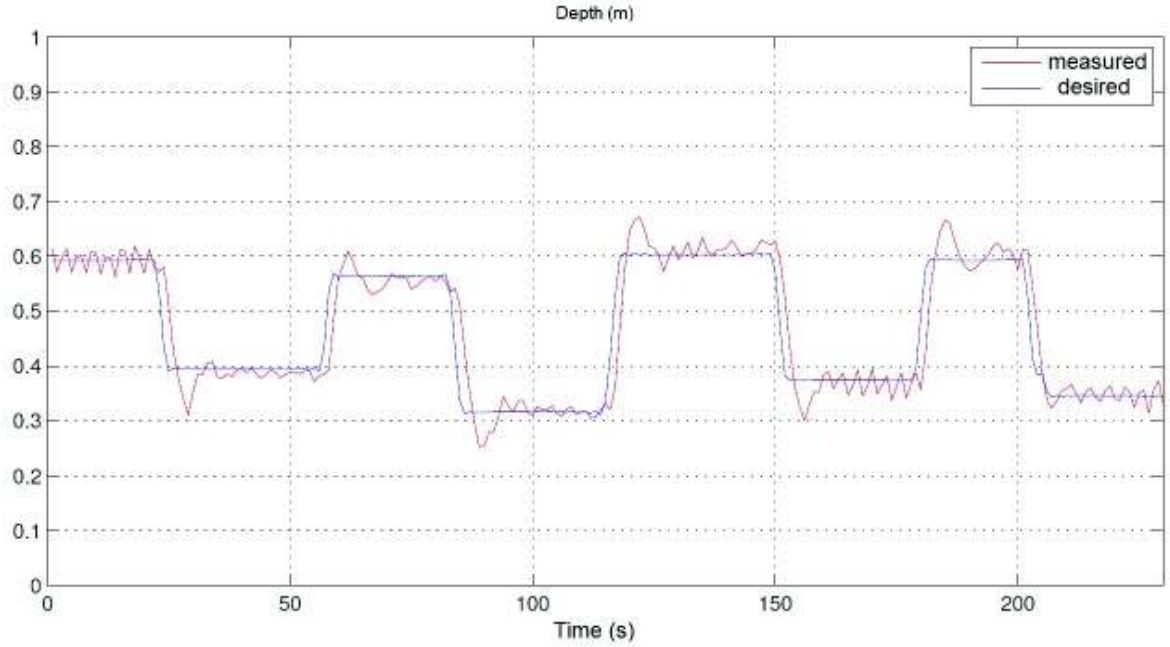

Figure 2.57: System response to step variations with $k_{pz} = 30$, $k_{iz} = 10$, $k_{dz} = 22.5$

The system has a maximum overshoot of about 7 cm, which in the operating scenario proves to be more than satisfactory.

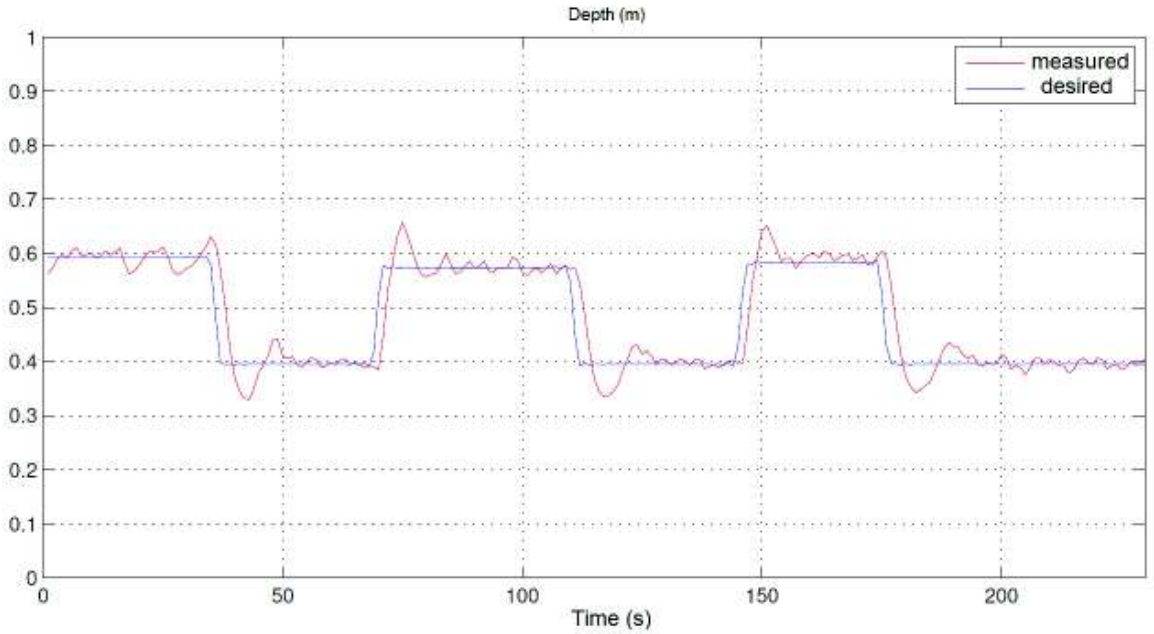

Figure 2.58: System response to step variations with $k_{pz} = 20$, $k_{iz} = 5$, $k_{dz} = 10$

Pitch

To regulate the ROV pitch it has been followed the approach shown for the yaw and depth control, but, considering the limited distance between the two vertical motors, the system has proved to be not very performing.

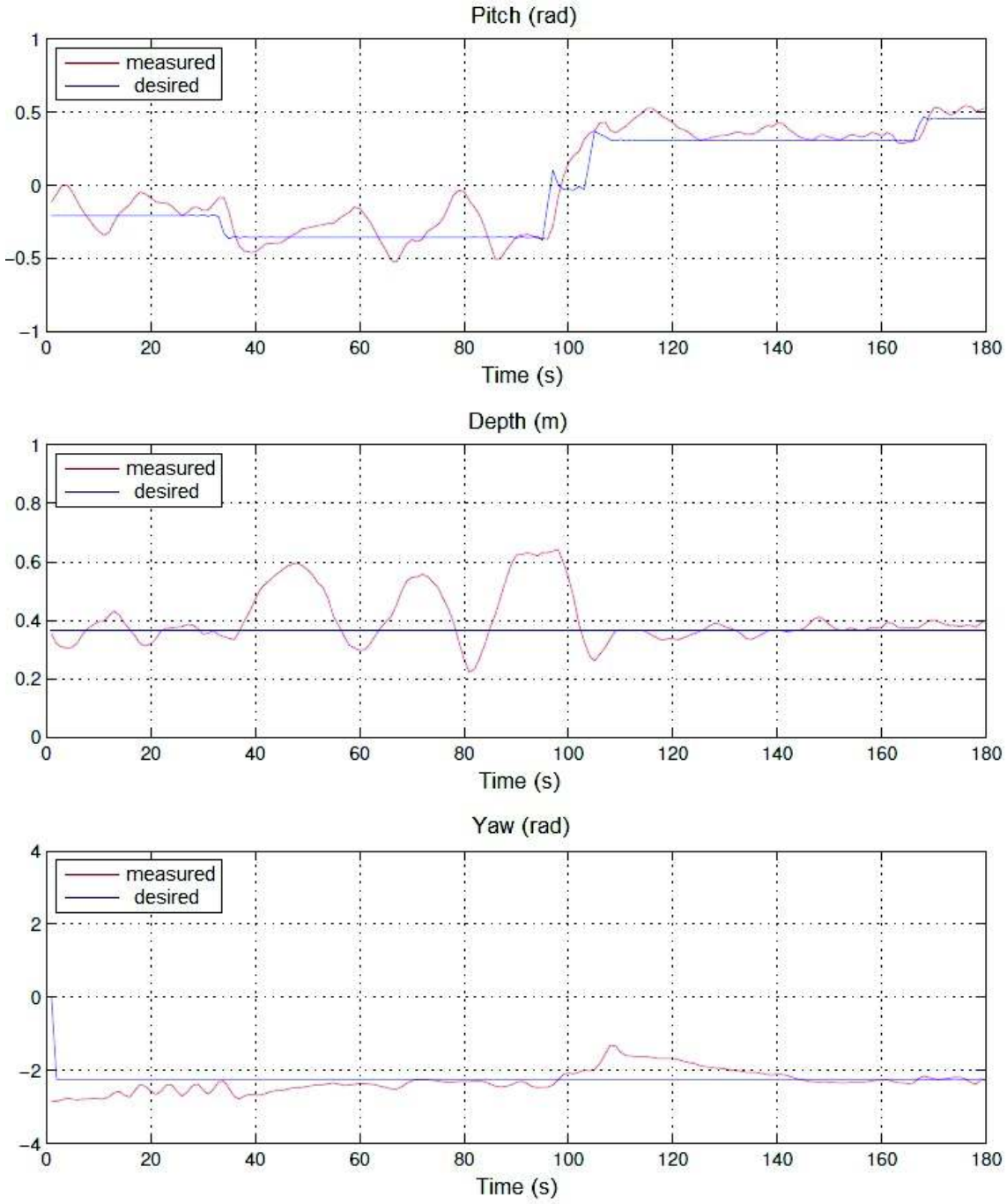

Figure 2.59: System response to step variations with $k_{p\theta} = 0.4$, $k_{i\theta} = 0$, $k_{d\theta} = 0$, $k_{pz} = 20$, $k_{iz} = 5$, $k_{dz} = 10$, $k_{p\psi} = 0.22$, $k_{i\psi} = 0.01$, $k_{d\psi} = 0.11$

In particular, setting the only proportional gain $k_{p\theta} = 0.4$, it has been observed the

vehicle is able to follow the reference, but with an excessive work of the vertical motors and consequently too much energy waste. In Figure 2.59, besides showing the pitch control, the negative effect this produces on depth and yaw control is displayed. Considering the obtained results (maximum reached inclination ±20°) and considering that the camera can be moved in the range of ±90° without having to move the vehicle, it has been decided not to implement an active pitch control.

2.7 Operating results

On March 5th 2013 the vehicle was tested at sea (Figure 2.60) in the coast area of Calafuria, in province of Livorno, Italy. The weather situation was not the most favourable as the sea was rather rough and it rained at intervals.

Figure 2.60: Nemo ROV during the mission in Calafuria

Mission started at 10:33 and ended at 12:09. The vehicle reached a maximum depth of 36.27 m and proved to be easily controllable during the whole length of the mission (in Figure 2.61 Nemo ROV, with a scuba diver, is shown during the operation). Diagrams of Figure 2.62 show the vehicle state as a function of time:

- during the first 25 minutes the vehicle was piloted at low depths and put back on the support boat to enable an area change. Data taken at zero depth are consequently negligible;
- between minute 25 and minute 53 the vehicle started its descent towards the depth showing a lower response in depth control about minute 37. This event is due to a cable problem, which proved to be too positive in the water and consequently

Figure 2.61: Nemo, with a scuba diver, during the mission in Calafuria

the engines could not provide enough vertical thrust to let the vehicle go down. To solve this problem, the cable was partly recovered on the surface, made heavier with sinkers and lowered in the water again. During this time break, the vehicle was subjected to irregular motions, explaining the unsteady behaviours of yaw and pitch;

- from minute 53 towards, the vehicle carried on its descent towards the seabed without meeting any difficulties. The excellent resolution of the camera is shown in Figure 2.63.

As regards roll and pitch (quantities not regulated by any PID for the previously described reasons), such measures have always turned out to be steady (apart from non ordinary situations which took place in the first 53 minutes) thanks to the hydrostatic balance work performed before the mission started.

Finally, on May 14th 2013 Nemo ROV carried out a monitoring mission of the Costa Concordia wreck (its sea side), at Isola del Giglio. As previously said, this was the main aim that gave birth to Nemo. Because of the confidentiality agreements with Costa Crociere (Figure 2.64) here are reported only some pictures of the underwater operations (Figures 2.65, 2.66 and 2.67):

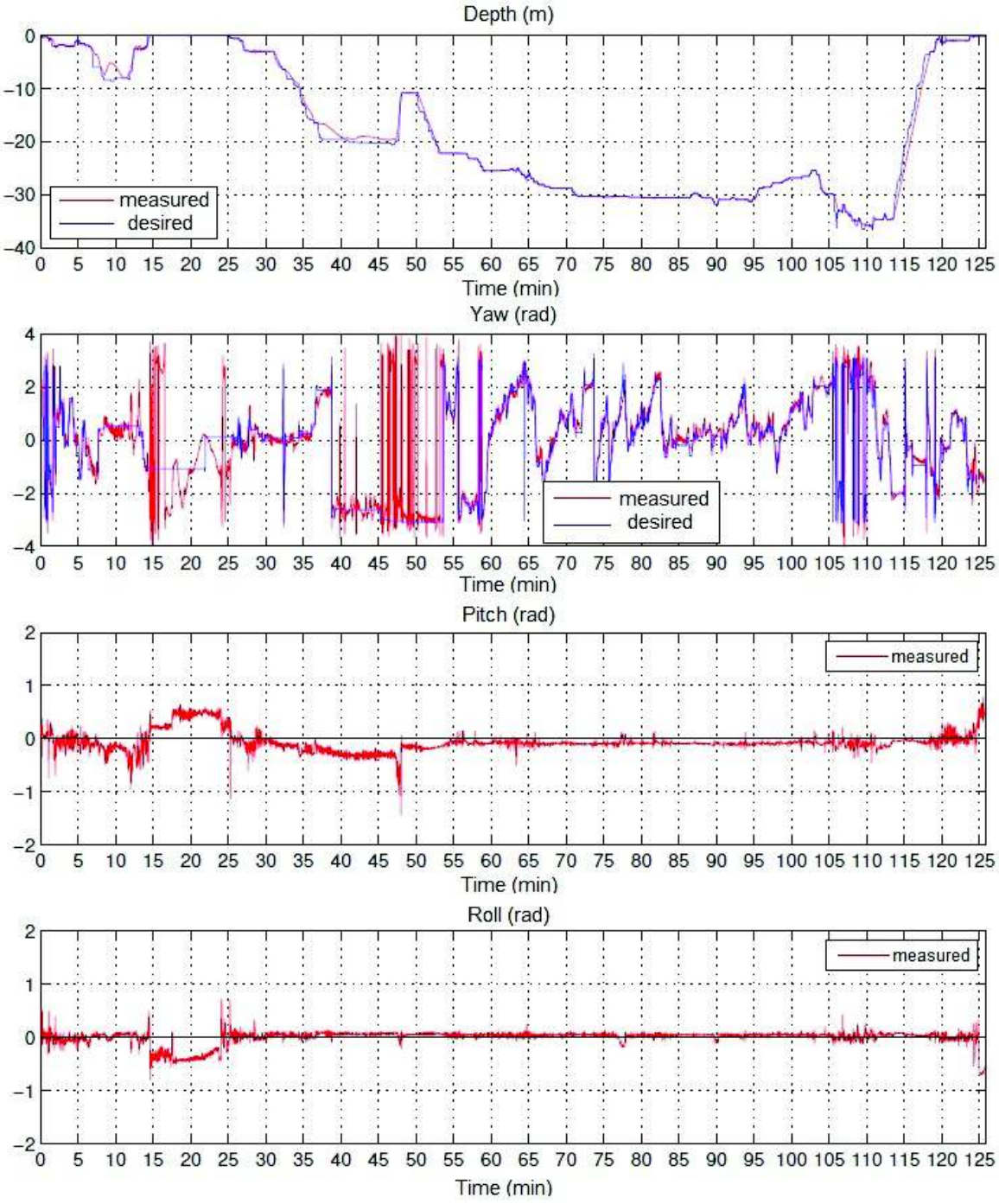

Figure 2.62: Data collected during the mission in Calafuria

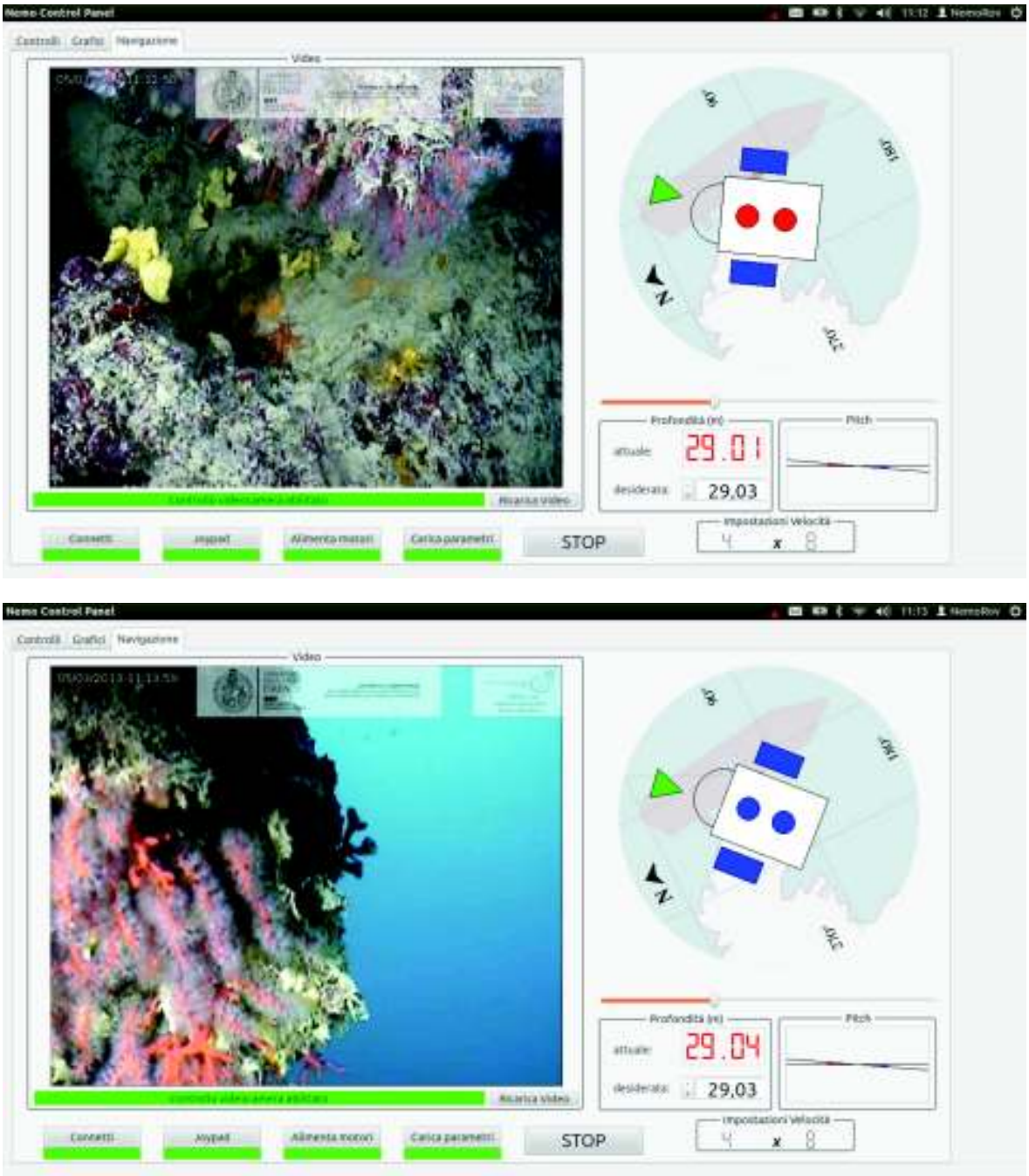

Figure 2.63: Screen shots of the mission in Calafuria

Figure 2.64: Costa Crociere logo

Figure 2.65: Nemo ROV control station

Figure 2.66: Nemo ROV control station and Costa Concordia wreck

Figure 2.67: Screen shot of Nemo graphic interface during the mission at Isola del Giglio

Chapter 3

Underwater Robotic Manipulation

3.1 State of the art of I-AUVs

The development of the Autonomous Underwater Vehicles (AUVs) has a great importance in modern society, because of their fundamental applications in the military field, in underwater explorations (e.g. archaeological field) and in the industrial field (e.g. for Oil&Gas applications). These devices, efficient and reliable, can undoubtedly lead to substantial economic and technological benefits. More specifically, in the technical evolution of the AUVs the following important topics are still characterized by many open problems: the dynamic performances and the control of the vehicle, the mobile tele-manipulation of a single vehicle and the cooperation among vehicles (whether including the manipulation operations or not). In this chapter the modelling and the control architecture of an AUV specifically thought for the underwater mobile manipulation, usually called I-AUV (Intervention-AUV), is described.

A considerable number of operations in sea-rescue, research and maintenance of oil rig appliances, got ahead nowadays using UUVs, need manipulation capacity to be concluded successfully. In such a scenario, most of the intervention missions at high depths are faced up by remotely controlled vehicles equipped with one or more robotic arms, representing up until today the standard technology in that field [5].
The ROVs for assistance, which can be teleoperated for long periods, are controlled with a master-slave approach [2] [3]. This kind of strategy has some limitations: the operator must have received a special type of training and consequently he is a highly specialized technician, underwater communication is hard and a significant delay in control can be present. If the operation has to be carried out at elevated depth, it is also necessary the presence of a supporting underwater vehicle following the ROV, in order to obviate the communication problems, and in any case of an ocean ship equipped with a heavy crane to lift the ROV when it emerges with important costs of the mission setting up. All these

problems, to which is added the presence of a long communication and power supply cable restricting the possible movements of the vehicle and of its arm, have recently brought some researchers to consider what appears as the AUV natural evolution, that is the autonomous underwater vehicle equipped with manipulator arms, the I-AUVs.

The I-AUV can be supported by small and simple surface vehicles, cutting down the mission costs. With the sensibly recent development of the technologies of batteries, and through the removal of human operator from the control loop, these vehicles can carry out operations of manipulation lasting more days: the ship is required only in the deployment and recovery phases of the AUV, while in the meantime it can be exploited for other purposes. Despite the several advantages appearing for the considered application, mainly because of the complexities in realization and control problems, only a few research centres are equipped with an I-AUV. The first attempt to realize an autonomous underwater vehicle equipped with a robotic arm dates back to the nineties and traces back to the development of ODIN and OTTER vehicles [5], respectively at Hawaii University and Stanford Robotic Lab. Both vehicles are completely actuated and have a simple manipulator with one degree of freedom, assigned to automatic rescue operations of submerged objects. Immediately afterwards, at French Ifremer, VORTEX (Versatile and Open subsea Robot for Technical Experiments) was shown, an under-actuated vehicle with 5 DOFs, equipped with a 7 link arm of Mitsubishi PA-10 type, born as ROV and usable in an automatic mode too. Such vehicles represent no doubt a step forward for the I-AUV technology, even if they are exclusively used in controlled conditions and environments, particularly for the study of the hydrodynamic model, of the manipulator arm and for considerations concerning the controllability of the hybrid system. In 1997 the European project AMADEUS (Advanced MAnipulation for DEep Underwater Sampling) was approved; the project involved many University partners, among whom University of Genova [7]. The project was focused on the coordinate control of two Ansaldo robotic arms at 7 DOFs mounted on a teleoperated ROV, in order to make an underwater cell able to pick samples and carry out complex manipulation operations on the seabed. In 2004 the development of this project led to the realization of SAUVIM (Semi-AUtonomous Vehicle for Intervention Missions), Hawaii University, shown in Figure 3.1, the first underwater vehicle to try underwater manipulation operations on the open sea [6].

SAUVIM is equipped with a manipulator arm with 7 links, the same used during AMADEUS project, which is controlled in an uncoupled way as to the vehicle body. This one is moved according to 6 degrees of freedom by 8 propellers and has a strong weight difference compared to the arm, a characteristic making possible the decoupling control of the two elements. The vehicle is just semi-autonomous, although the supply takes place through batteries, because it is equipped with a cable allowing communication during the oper-

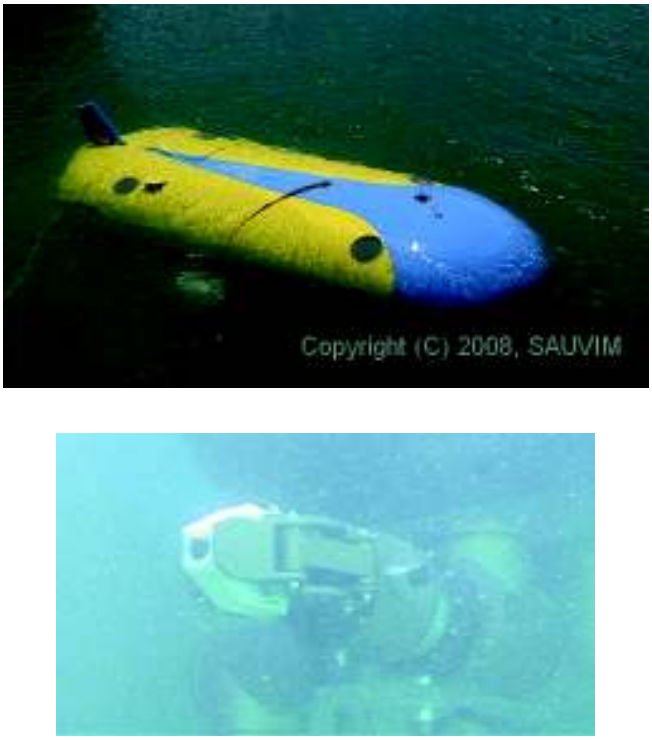

Figure 3.1: SAUVIM vehicle, with Ansaldo robotic arm

ation: the user specifies just instructions at high level, on the basis of the outputs of the vision sensor and the other on board sensors, while the robot runs in an autonomous way the low level orders, which are necessary to perform the mission. SAUVIM is till today used for the recovery of objects from the seabed or for other dexterous manipulation operations, as it can sink at a maximum depth of 4000 m. The following researches in the technology field of I-AUV are mainly focused to reach a higher and higher autonomous capacity as regards intervention missions. The vehicles, developed up to that moment, were large-sized and heavy, able to work at high depth and in ocean environments: a special interest was consequently given to the development and realization of smaller and lighter I-AUVs (with mass below 300 kg), used for intervention up to a depth of 500 m, among which ALIVE vehicle (Autonomous Light Intervention VEhicle, shown in Figure 3.2), born within the framework of the FP5 European project GROWTH.

One last important contribution to the development of the state of the art of the I-AUV is finally due to TRIDENT (Figure 3.3), an European project lasting for 3 years and started in 2010 [12]. The aim of TRIDENT was the development of new methodologies to complete manipulation assistances in non-structured underwater environments, through a cooperative team composed of an AUV equipped with a robotic arm at 7 DOFs and an ASC (Autonomous Surface Craft): the latter is an autonomous surface vehicle, whose aim is to replace, in the application near to the coast, the ship with crew necessary to the running of the AUV.

Figure 3.2: ALIVE vehicle

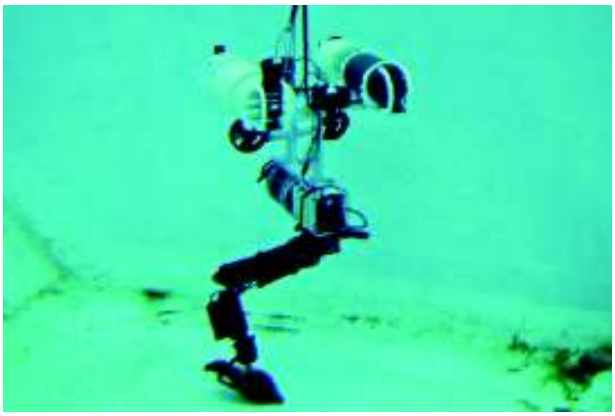

Figure 3.3: I-AUV in the framework of TRIDENT project

Through the ASC and having at disposal an USBL and an acoustic modem, it is possible to establish a communication with the I-AUV itself, useful in the phases of remote tracking and supervision on the user's part, allowing a further reduction of costs of the whole operation. Many European partners, among whom Heriot-Watt University (Scotland), with Nessie AUV, and Girona University (Spain), with SPARUS, took part in this project.

As regards the control techniques of such vehicles, the problem is still open. Up to now decoupled controls for the AUV subsystem and the manipulator have been mostly studied [5], assuming the weight difference between the two elements is wide enough, and speeds are low, so that, this way, good control performances can be achieved.

3.2 I-AUV kinematics

To face the kinematic study of the system characterized by the AUV and the robotic arm it is necessary to present the kinematic model of the manipulator arm, which is here assumed to be, for the considered application, an anthropomorphic robot with a spherical wrist. Such a manipulator can be schematized as a serial mechanism (Figure 3.5) made up of 6 rigid bodies (links of the robot) connected through some kinematic pairs (joints of the robot) of rotational type. The kinematic model of a serial robot can be dealt with by solving two problems: the former concerns the direct kinematics and the latter the inverse kinematics, to define in a complete way the relationship existing among the joint positions and the pose of the terminal member, the end-effector [15]. Some simplifications have been introduced, to lighten the treatment.

3.2.1 System schematization

In Figure 3.4, in a schematic way, the geometrical model of the system is shown: the system is made up of the AUV, with equivalent dimensions BxLxH, and the manipulator arm. This one, composed of 2 links of cylindrical form is linked to the frame (that is the vehicle body) just next to the frontal face, located down below and at the center, to minimize the rolling disturbances and keeping at the same time the center of the mass of the vehicle under the buoyancy one: the arm moves as to the vehicle rotating on two axes which are orthogonal each other.

The two links (arm and forearm) can rotate the one comparatively to the other around a transversal axis and have an end-effector equipped with a gripper. This one is made up of three rigid bodies: one first body, with prismatic shape, connected to the terminal link through a spherical pair, and two identical bodies, they too of prismatic form, connected

to the ends of the main body by two rotating joints. The center of RPY spherical wrist is in the intersection of the rotation axes of the gripper as to the link of the forearm; besides, the reference frames are shown, linked to each rigid body and used to calculate the hydrodynamic terms.
Comparing this scheme with the general one shown in Figure 3.5 it is possible to note the manipulator, the AUV is equipped with, is the same as an anthropomorphic robot with first link collapsed in a single point, the intersection of the two rotation axes of the arm as the vehicle (shoulder) and the three bodies of the spherical wrist collapsed in the center of the wrist itself, as well. To have a more realistic representation of the wrist, some finite lengths for these links and reasonable mass and inertia properties are assumed any way. The gripper, as it is composed of three mobile parts, represents a final branching of the kinematic chain, up to such a point of serial type, of the manipulator.

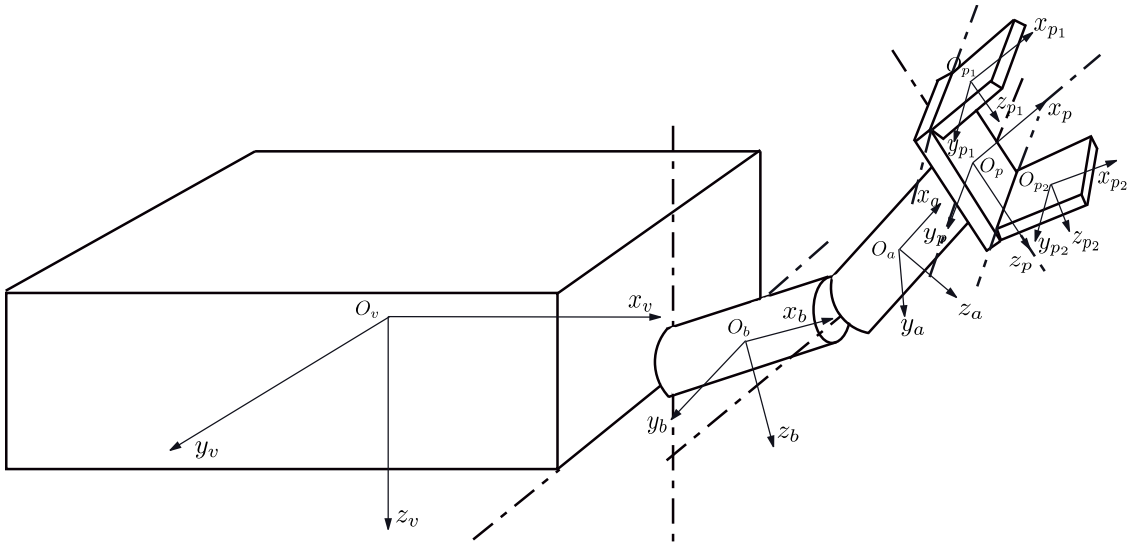

Figure 3.4: Geometrical scheme of the I-AUV, equipped with robotic arm, composed of 2 links, and a gripper (end-effector)

3.2.2 Direct kinematics

The aim of the direct kinematics is the determination of the pose of the manipulator terminal organ (end-effector), as a function of the values assumed by the joint variables:

$$T_n^0 = T_n^0(\vec{q}) \ , \tag{3.1}$$

where $T_n^0 \in \mathbb{R}^{4x4}$ is the homogeneous transformation matrix between a frame $< 0 >$ linked to the robot frame, in this case the AUV, and a frame $< n >$ linked to the end-effector, while $\vec{q} \in \mathbb{R}^{nx1}$ is the vector of the joint variables. The solution of the direct kinematic problem for serial mechanisms always exists and it is unique and can be calculated

with a systematic and totally general procedure.
On this point, an open chain manipulator made up of $n+1$ links connected n joints, where to each link is linked the $< i >$ reference frame, can be considered. Every joint is associated to a single degree of freedom to the mechanical structure, corresponding to the joint variable q_i. The total transformation, expressing the position and orientation of $< n >$ frame (linked to the end-effector) as to $< 0 >$ frame (linked to the frame) is given by:

$$T_n^0(\vec{q}) = \prod_{i=1}^{n} A_i^{i-1}(q_i) \ , \tag{3.2}$$

where $A_i^{i-1}(q_i)$ is the homogeneous transformation matrix between $< i-1 >$ and $< i >$ systems, that is a function of the only joint variable q_i.

To generalize the calculation of matrices appearing in (3.2), the reference frames linked to each link are defined in accordance with the Denavit-Hartenberg (or D-H) convention [15]. In case of the anthropomorphic manipulator with spherical wrist, made up of 6 links, joined by 6 rotational pairs, the chosen reference frames $< i >$, with $i = 0,...,6$, are displayed in Figure 3.5.

Once the frames linked to the arms have been set, the position and the orientation of $< i >$ as to $< i-1 >$ are completely specified by the four D-H scalar parameters a_i, d_i, α_i and ϑ_i; the associated homogeneous transformation matrix turns out to be the following:

$$A_i^{i-1}(q_i) = \begin{bmatrix} c_{\vartheta_i} & -s_{\vartheta_i} c_{\alpha_i} & s_{\vartheta_i} s_{\alpha_i} & a_i c_{\vartheta_i} \\ s_{\vartheta_i} & c_{\vartheta_i} c_{\alpha_i} & -c_{\vartheta_i} s_{\alpha_i} & a_i s_{\vartheta_i} \\ 0 & s_{\alpha_i} & c_{\alpha_i} & d_i \\ 0 & 0 & 0 & 1 \end{bmatrix} . \tag{3.3}$$

Link	a_i	α_i	d_i	ϑ_i
1	0	$\pi/2$	0	ϑ_1
2	a_2	0	0	ϑ_2
3	0	$\pi/2$	0	$\vartheta_3 + \frac{\pi}{2}$
4	0	$-\pi/2$	d_4	ϑ_4
5	0	$\pi/2$	0	ϑ_5
6	0	0	d_6	ϑ_6

Table 3.1: Denavit-Hartenberg parameters of the anthropomorphic manipulator with spherical wrist

D-H parameters of the anthropomorphic manipulator with a spherical wrist are specified in Table 3.1. According to (3.2) and (3.3), the homogeneous transformation matrix is

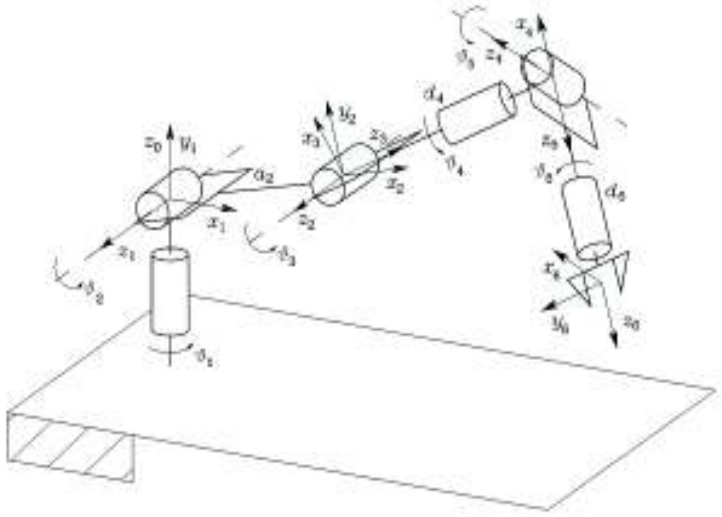

Figure 3.5: Kinematic scheme of the anthropomorphic manipulator with spherical wrist: reference frames linked to the links, joint coordinates $q_i = \vartheta_i$, with $i = 1,...,6$, and D-H parameters a_2, d_4 e d_6

therefore given by:

$$T_n^0(\vec{q}) = \left[\begin{array}{ccc|c} \vec{n}_6^0 & \vec{s}_6^0 & \vec{a}_6^0 & \vec{p}_6^0 \\ \hline 0 & 0 & 0 & 1 \end{array}\right], \tag{3.4}$$

where $\vec{p}_6^0$ vector, specifying the position of the end-effector in $<0>$ frame results:

$$\vec{p}_6^0 = \begin{bmatrix} a_2c_1c_2 + d_4c_1s_{23} + d_6(c_1(c_{23}c_4s_5 + s_{23}c_5) + s_1s_4s_5) \\ a_2s_1c_2 + d_4s_1s_{23} + d_6(s_1(c_{23}c_4s_5 + s_{23}c_5) - c_1s_4s_5) \\ a_2s_2 - d_4c_{23} + d_6(s_{23}c_4s_5 - c_{23}c_5) \end{bmatrix}, \tag{3.5}$$

while the unitary vectors, the *normal* one (along x_6), the *sliding* one (along y_6) and the *approach* one (along z_6) have this expressions, in $<0>$frame too:

$$\begin{aligned} \vec{n}_6^0 &= \begin{bmatrix} c_1(c_{23}(c_4c_5c_6 - s_4s_6) - s_{23}s_5c_6) + s_1(s_4c_5c_6 + c_4s_6) \\ s_1(c_{23}(c_4c_5c_6 - s_4s_6) - s_{23}s_5c_6) - c_1(s_4c_5c_6 + c_4s_6) \\ s_{23}(c_4c_5c_6 - s_4s_6) + c_{23}s_5s_6 \end{bmatrix} \\ \vec{s}_6^0 &= \begin{bmatrix} c_1(-c_{23}(c_4c_5s_6 + s_4c_6) + s_{23}s_5s_6) + s_1(-s_4c_5s_6 + c_4c_6) \\ s_1(-c_{23}(c_4c_5s_6 - s_4c_6) + s_{23}s_5c_6) - c_1(-s_4c_5s_6 + c_4c_6) \\ s_{23}(c_4c_5s_6 + s_4c_6) - c_{23}s_5s_6 \end{bmatrix} \\ \vec{a}_6^0 &= \begin{bmatrix} c_1(c_{23}c_4s_5 + s_{23}c_5) + s_1s_4s_5 \\ s_1(c_{23}c_4s_5 + s_{23}c_5) - c_1s_4s_5 \\ s_{23}c_4s_5 - c_{23}c_5 \end{bmatrix}. \end{aligned} \tag{3.6}$$

If, in the end, the tool frame and the basis frame do not coincide with $< 0 >$ and $< n >$ Denavit-Hartenberg frames (shown in the Figure), the actual transformation setting out position and orientation of $< e >$ tool frame with respect to $< b >$ basis frame, is obtained as follows:

$$T_e^b(\vec{q}) = T_0^b T_n^0(\vec{q}) T_e^n . \tag{3.7}$$

In the under examination case links 0 and 1 of the manipulator collapse just in one point, and D-H parameters a_2, d_4 and d_6 match, with the exception of the limited dimensions of the wrist links, respectively with the arm and forearm lengths and with the distance between the center of the wrist W and the center of the mass of the main body of the gripper. Finally as regards the manipulator gripper, referring to Figure 3.6, the homogeneous transformation matrix between $< 6 >$ frame linked to the main gripper body and $< p_1 >$ frame is:

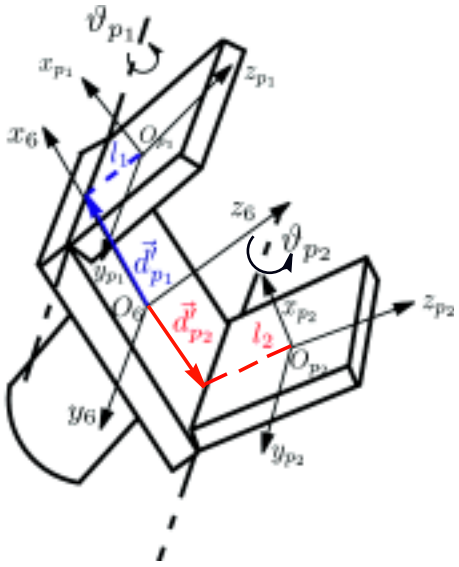

Figure 3.6: Gripper kinematics

$$T_{p_1}^6(\vartheta_{p_1}) = \left[\begin{array}{ccc|c} c_{\vartheta_{p1}} & 0 & s_{\vartheta_{p1}} & \\ 0 & 1 & 0 & \vec{d}_{p1} \\ -s_{\vartheta_{p1}} & 0 & c_{\vartheta_{p1}} & \\ \hline 0 & 0 & 0 & 1 \end{array}\right] , \tag{3.8}$$

where $\vec{d}_{p1} = \vec{d}'_{p1} + \left[l_1 s_{\vartheta_{p1}}, 0, l_1 c_{\vartheta_{p1}}\right]^T$, and similarly for $T_{p_2}^6\left(\vartheta_{p2} = -\vartheta_{p1}\right)$, where $\vec{d}_{p2} = \vec{d}'_{p2} + \left[l_2 s_{\vartheta_{p2}}, 0, l_2 c_{\vartheta_{p2}}\right]^T$.

3.2.3 Inverse kinematics

The inverse kinematic problem concerns the determination of the joint variables, when the pose of the end-effector is assigned. Its solution is crucially important to translate the motion statements, given in the operating space of the end-effector, in the corresponding motions in the joint space, that is to pass from the knowledge of $\vec{p}_n^0 = \vec{p}_{n,\mathrm{des}}^0(t)$ and $R_n^0 = R_{n,\mathrm{des}}^0(t)$, to $\vec{q} = \vec{q}_{\mathrm{des}}(t)$.
Generally speaking the inverse kinematic problem is more complex than the direct one, because equations to solve are strongly non-linear: analytic solutions can or cannot exist, and, if they exist, they can be multiple, in a finite or infinite number. Moreover such solutions have to be found case by case, with geometrical approaches, as there is not a systematic procedure to face this type of problem. In case of anthropomorphic manipulator with spherical wrist, the existence of a solution in closed form is assured by Pieper theorem: the inverse kinematic problem can actually be divided into two sub-problems, the former for the solution of the end-effector position, and the latter for the solution of its orientation, identifying one point W given by the intersection of three adjacent rotational axes, in the case, the wrist ones.

As for the first sub-problem, once position and orientation of the tool frame have been assigned, $\vec{p}_6^0$ and R_n^0, the position of the center of the wrist is identified by the equation:

$$\vec{p}_W = \vec{p}_n^0 - d_6 \vec{a}_n^0 \,, \tag{3.9}$$

function of the only joint variables ϑ_1, ϑ_2 and ϑ_3, determining the configuration of the anthropomorphic structure. From the partial matrix of homogeneous transformation $T_3^0(q_1,q_2,q_3)$, it results:

$$\begin{aligned} p_{W_x} &= c_1(a_2c_2 + a_3c_{23}) \\ p_{W_y} &= s_1(a_2c_2 + a_3c_{23}) \\ p_{W_z} &= a_2s_2 + a_3s_{23} \,, \end{aligned} \tag{3.10}$$

from which, squaring and summing the first and the third relation, is obtained

$$\begin{aligned} c_3 &= \frac{p_{W_x}^2 + p_{W_y}^2 + p_{W_z}^2 - a_2^2 - a_3^2}{2a_2a_3} \\ s_3 &= \pm\sqrt{1-c_3^2} \,, \end{aligned} \tag{3.11}$$

with condition of admissibility of solution $-1 \le c_3 \le 1$; otherwise the point of the center of the wrist would result outside the accessible workspace of the manipulator. Consequently two solutions will be possible, on the basis of the sign of s_3, corresponding to the elbow-up and elbow-down configuration.

$$\begin{aligned}\vartheta_{3,\mathrm{I}} &= \mathrm{atan2}(s_3, c_3) \in [-\pi, \pi] \\ \vartheta_{3,\mathrm{II}} &= -\mathrm{atan2}(s_3, c_3)\ .\end{aligned} \tag{3.12}$$

ϑ_2 angle on the contrary can be calculated by summing and squaring the first two relations in (3.10), put in system with the third one, so that obtaining:

$$\begin{aligned}c_2^{\pm} &= \frac{\pm\sqrt{p_{W_x}^2 + p_{W_y}^2}\,(a_2 + a_3 c_3) + p_{W_z} a_3 s_3}{a_2^2 + a_3^2 + 2a_2 a_3 c_3} \\ s_2^{\mp} &= \frac{\mp\sqrt{p_{W_x}^2 + p_{W_y}^2}\,a_3 s_3 + p_{W_z}(a_2 + a_3 c_3)}{a_2^2 + a_3^2 + 2a_2 a_3 c_3}\ ,\end{aligned} \tag{3.13}$$

with

$$\vartheta_2 = \mathrm{atan2}(s_2, c_2)\ . \tag{3.14}$$

Such a problem admits 4 solutions, according to the sign of s_3 and the one assumed for the roots appearing in (3.13) (specified as summit of c_2 and s_2):

$$\begin{aligned}\vartheta_{2,\mathrm{I}} &= \mathrm{atan2}\left(s_2^-, c_2^-\right) \\ \vartheta_{2,\mathrm{II}} &= \mathrm{atan2}\left(s_2^+, c_2^-\right)\end{aligned} \tag{3.15}$$

with $s_3 = \sqrt{1 - c_3^2}$, e

$$\begin{aligned}\vartheta_{2,\mathrm{III}} &= \mathrm{atan2}\left(s_2^-, c_2^-\right) \\ \vartheta_{2,\mathrm{IV}} &= \mathrm{atan2}\left(s_2^+, c_2^-\right)\end{aligned} \tag{3.16}$$

for $s_3 = -\sqrt{1 - c_3^2}$.

Finally to calculate ϑ_1, it is necessary to write again (3.10) in the following way:

$$\begin{aligned}p_{Wx} &= \pm c_1 \sqrt{p_{Wx}^2 + p_{Wy}^2} \\ p_{Wx} &= \pm s_1 \sqrt{p_{Wx}^2 + p_{Wy}^2}\ ,\end{aligned} \tag{3.17}$$

that, solved, provide the two solutions

$$\begin{aligned}\vartheta_{1,\mathrm{I}} &= \mathrm{atan2}\left(p_{Wy}, p_{Wx}\right) \\ \vartheta_{1,\mathrm{II}} &= \mathrm{atan2}\left(-p_{Wy}, -p_{Wx}\right)\ .\end{aligned} \tag{3.18}$$

In conclusion there are 4 configurations of the robotic structure compliant with an assigned position of the center of the wrist, if this is inside the workspace of the robot. These configurations coincide with elbow-up and elbow-down, coupled with right shoulder or

left shoulder, with ϑ_1 given by the first or second of (3.18).

On the contrary, as regards the orientation sub-problem, joint variables ϑ_4, ϑ_5 and ϑ_6 make up the set of Euler angles ZYZ of $<6>$ tool frame as to $<3>$ frame. Therefore, once T_6^3 homogeneous transformation matrix is calculated, the solution is given by:

$$\begin{aligned}\vartheta_4 &= \text{atan2}\left(T_6^3(2,3), T_6^3(1,1)\right)\\ \vartheta_5 &= \text{atan2}\left(\sqrt{T_6^3(1,3)^2 + T_6^3(2,3)^2}, T_6^3(3,3)\right)\\ \vartheta_6 &= \text{atan2}\left(T_6^3(3,2)^3, -T_6^3(3,1)\right)\end{aligned} \tag{3.19}$$

for $\vartheta_5 \in (0,\pi)$ (*wrist* configuration), and

$$\begin{aligned}\vartheta_4 &= \text{atan2}\left(-T_6^3(2,3), -T_6^3(1,1)\right)\\ \vartheta_5 &= \text{atan2}\left(-\sqrt{T_6^3(1,3)^2 + T_6^3(2,3)^2}, T_6^3(3,3)\right)\\ \vartheta_6 &= \text{atan2}\left(-T_6^3(3,2)^3, T_6^3(3,1)\right)\end{aligned} \tag{3.20}$$

for $\vartheta_5 \in (-\pi,0)$ (*flip-wrist*).

3.2.4 Differential inverse kinematics

The use of a redundant manipulator (e.g. 7 DOFs, adding 1 redundant DOF to the standard anthropomorphic manipulator previously shown) for underwater manipulation tasks is useful to complete the task and to avoid singularities. Singularities are particular robot configurations in which the Jacobian matrix loses rank. When the manipulator is redundant, the Jacobian matrix has more columns than rows and infinite solution exist to the classical relation between velocity in the operative space and velocities of the joints:

$$\vec{v}_e = \begin{bmatrix}\dot{\vec{p}}_e\\ \vec{\omega}_e\end{bmatrix} = J\dot{\vec{q}} \tag{3.21}$$

An interesting method to use the redundant DOFs is to formulate the problem as a constrained optimization problem. Particularly, once the end-effector speed $\vec{v}_e$ and the Jacobian J are given, it is desired to find the solution $\dot{\vec{q}}$ that satisfies the linear equation (3.21) and minimizes the quadratic cost functional of joint velocities. The problem can be solved through the Lagrange multipliers method.

$$\dot{\vec{q}} = J_r^\dagger \vec{v}_e \tag{3.22}$$

where

$$J_r^\dagger = J^T(JJ^T)^{-1} \tag{3.23}$$

is the right pseudo-inverse of Moore-Penrose. The obtained solution locally minimizes the norm of the joint velocities. Supposing $\dot{\vec{q}}$ a solution of (3.21), then also $\dot{\vec{q}} + N_J \dot{\vec{q}}_o$ is a solution in case that N_J were a projection of the vector $\dot{\vec{q}}_o$ in the null space of J.

$$\dot{\vec{q}} = J_r^{\dagger} \vec{v}_e + (I - J_r^{\dagger} J)\dot{\vec{q}}_0 \tag{3.24}$$

The solution of this equation is composed of two terms: the first one is relative to the minimum norm joint velocities, and the second one can satisfy an additional constrain. A direct consequence is that in case of $\vec{v}_e = 0$ it is possible to generate internal motions that reconfigure the manipulator structure without changing the end-effector pose.
The $\dot{\vec{q}}$ satisfies equation (3.21) and is very close to $\dot{\vec{q}}_0$. In literature, there are many possible choices of $\dot{\vec{q}}_0$ and one of these is:

$$\dot{\vec{q}}_0 = k_0 \left(\frac{\partial w(\vec{q})}{\partial \vec{q}} \right)^T \tag{3.25}$$

where $k_0 > 0$ and $w(\vec{q})$ is a secondary objective function of the joint variables. Since the solution moves along the direction of the gradient of the objective function, it attempts to maximize it locally compatibly to the primary objective. A typical objective function $w(\vec{q})$ is the following:

$$w(\vec{q}) = \sqrt{det(J(\vec{q})J^T(\vec{q}))} \tag{3.26}$$

which becomes zero at a singular configuration; thus, by maximizing this measure, redundancy is exploited to move away from singularities.
The inversion of the differential kinematics very close to a singularity can create many problems in terms of computational load. Therefore, it is useful to improve the robustness of the Jacobian J (or $J_r^{\dagger}$) with a damped least squares inverse, defined as:

$$J^{\star} = J^T (J J^T + k^2 I)^{-1} \tag{3.27}$$

where $k^2 I$ is the the damping factor that renders the inversion better conditioned from a numerical point of view.

3.3 I-AUV dynamics

The multibody model of the vehicle and of the robotic arm considers all the DOFs of the I-AUV; in the same way the multibody model of the gripper part accurately describes the dynamics of the object to be grasped and the interaction gripper-environment. The modelling of the gripper-object contact [26] affects the behaviour of the whole system. The whole multibody model has been implemented in the Matlab-Simulink^{TM} environ-

ment, through the SimMechanics toolbox.
The interaction among the different system bodies and the fluid, on the contrary, has been modelled by means of appropriate CFD analyses [25]. In particular the mathematical coupling between the multibody model and the fluid equations has been efficiently performed through the toolbox SimMechanics.
The adopted reference frames and notation are the same of the ones described in chapter 1 (section 1.3).

3.3.1 Equations of motion

The dynamical model of the system (I-AUV) consists of two different parts: an underwater vehicle (AUV) and a robotic arm. The hypotheses to study the models are to assume that both the vehicle and the various links of the manipulator can be considered as rigid bodies and connected by revolute kinematic joints.
The external forces and torques, i.e. the hydrodynamic effects and the buoyancy, are introduced into the model by means of generalized Lagrangian forces applied to each body constituting the multibody system (the body-vehicle, the links, the robotic manipulator arm and the gripper).
An effective approach is proposed to face the problem of the implementation of the hydrodynamic and the buoyancy effects into the multibody system. The method proposes to separate the dynamical study of the rigid system from the one of hydrodynamic and buoyancy effects; first of all, it is necessary to obtain, from the Newtonian formulation of the system, the external forces and torques acting on the various bodies of the multibody system. In the equation of motion to describe the whole system [1] there are the contributions of the control actions $\vec{\tau}$ and of the hydrodynamic and buoyancy effects $\vec{\tau}_H$:

$$\begin{aligned} M_{RB}\dot{\vec{v}} + C_{RB}(\vec{v})\vec{v} &= \vec{\tau}_H(\vec{v},\vec{v}_C) + \vec{g}(\vec{\eta}) + \vec{\tau} \\ \dot{\vec{\eta}} &= J(\vec{\eta})\vec{v} \end{aligned} \tag{3.28}$$

where the absolute velocity of the vehicle $\vec{v}$ is written in the body reference frame, $\vec{v}_c$ is the current velocity, M_{RB} is the rigid body mass matrix, C_{RB} is the Coriolis rigid body matrix and $\vec{g}$ is the gravity vector.
The hydrodynamic and buoyancy effects $\vec{\tau}_H$ can be calculated for each body in accordance with [1] and [5]. These actions are reduced and applied to the Center of Gravity (CG) of each rigid bodies.

3.3.2 Multibody system dynamics

The Lagrangian redundant approach has been used to study the dynamics of the rigid bodies (this method is mainly used in softwares able to model and simulate multibody systems).
A set of redundant Lagrangian coordinates is introduced:

$$\vec{q} = \left(\vec{q}_1^T, ..., \vec{q}_N^T\right)^T \in \mathbb{R}^{6\text{Nx1}} \text{ , with } \vec{q}_i = \begin{bmatrix} \vec{G}_i \\ \vec{\Phi}_i \end{bmatrix} \in \mathbb{R}^{6\text{x1}} \quad i = 1,...,N \text{ ,} \tag{3.29}$$

where $\vec{G}_i$ and $\vec{\Phi}_i$ are respectively the coordinates of the CG and the Euler angles of the i-th rigid bodies.
It is assumed that the constraints are two-sided, sufficiently regular and independent, representable by algebraic equations in which it does not appear explicitly the time variable and holonomic (constraints on the configuration).
The algebraic equation of the constraints can be written in a compact form, such as:

$$\vec{\psi}\left(\vec{q}\right) = \vec{0} \text{ ,} \tag{3.30}$$

with $\vec{\psi} \in \mathbb{R}^p$ (p is the number of Degree of Freedoms DOFs taken out by the constrains).
The Lagrange equations for rigid body systems are obtained as a condition of stationary (minimization) of the generalized Lagrangian function $\mathscr{L}^*$ estimated as:

$$\mathscr{L}^*\left(\dot{\vec{q}}, \vec{q}, \vec{\lambda}\right) = T\left(\dot{\vec{q}}, \vec{q}\right) - V\left(\vec{q}\right) - \vec{\lambda}^T \vec{\psi}\left(\vec{q}\right) \text{ ,} \tag{3.31}$$

where T is the kinetic energy of the system, V the potential energy and $\vec{\lambda} \in \mathbb{R}^p$ is the Lagrangian vector.
The complete differential-algebraic equation (DAE) system, which is obtained from the previous equation, can be described through a unique matrix equation:

$$\begin{bmatrix} M & \left(\dfrac{\partial \vec{\psi}}{\partial \vec{q}}\dot{\vec{q}}\right)^T \\ \dfrac{\partial \vec{\psi}}{\partial \vec{q}}\dot{\vec{q}} & 0_{pxp} \end{bmatrix} \begin{Bmatrix} \ddot{\vec{q}} \\ \vec{\lambda} \end{Bmatrix} = \begin{Bmatrix} \vec{Q} - C\dot{\vec{q}} - \left(\dfrac{\partial V}{\partial \vec{q}}\right)^T \\ \vec{\gamma} \end{Bmatrix} . \tag{3.32}$$

The use of the Lagrangian approach allows the study of the complete I-AUV model in terms of rigid dynamic equations. The hydrodynamic effects are taken into account inside vector $\vec{Q}$.

3.3.3 Hydrodynamics and buoyancy effects

The modelling of hydrodynamics and buoyancy effects is necessary to reproduce in a proper way the I-AUV during a navigation or a manipulation task. These actions in each body belonging to the I-AUV system have been implemented (vehicle, links of the arm and gripper). The hydrodynamic and buoyancy effects $\vec{\tau}_H$ can be calculated for each body. In particular, the simulated effects are:

- hydrostatic effects due to the added masses;
- hydrodynamic effects due to the added masses;
- drag and lift forces;
- buoyancy effects.

For each body, these terms are described as to a reference frame system having its origin in the CG of the body, with axes parallel to the principal axes of inertia, vertical downhill z-axis, x-axis along the direction of the vehicle (when the robotic arm is stretched) and y-axis accordingly in order to define a right-handed reference frame.
As regards the links of the robotic arm, three assumptions have been supposed: cylindrical shape, totally immersed bodies and characterized by three levels of symmetry. Assuming that the arm does not move at high velocities, in order to correctly calculate $\vec{\tau}_H$ the added mass matrix M_A and the matrix of the centrifugal and Coriolis effects C_A have to be evaluated (M_A and C_A are described in [1] [5]).
For a cylindrical body of mass m, length L and radius R, which moves in a fluid of density ρ_a, the coefficients of matrices M_A and C_A can be obtained according to the strip theory, and according to the hypothesis $R \ll L$, the following equations are obtained:

$$\begin{aligned} &X_{\dot{u}} = -\tfrac{1}{10}\pi\rho_a R^2 L,\ Y_{\dot{v}} = -\pi\rho_a R^2 L,\ Z_{\dot{w}} = -\pi\rho_a R^2 L \\ &K_{\dot{p}} = 0, \qquad M_{\dot{q}} = -\tfrac{1}{12}\pi\rho_a R^2 L^3,\ N_{\dot{r}} = -\tfrac{1}{12}\pi\rho_a R^2 L^3 \,. \end{aligned} \tag{3.33}$$

As regards the effects of the hydrodynamic resistance, the elements of the damping matrix D are evaluated, by means of CFD analysis [25], as already seen in chapter 1.

3.4 Manipulation control logic

The logic of the whole manipulation model is shown in Figure 3.7.

The control architecture [28] is made up of 3 fundamental parts (as visible in Figure 3.7): the trajectory planning [1] [11], the vehicle control [1] [5] and the robotic arm control

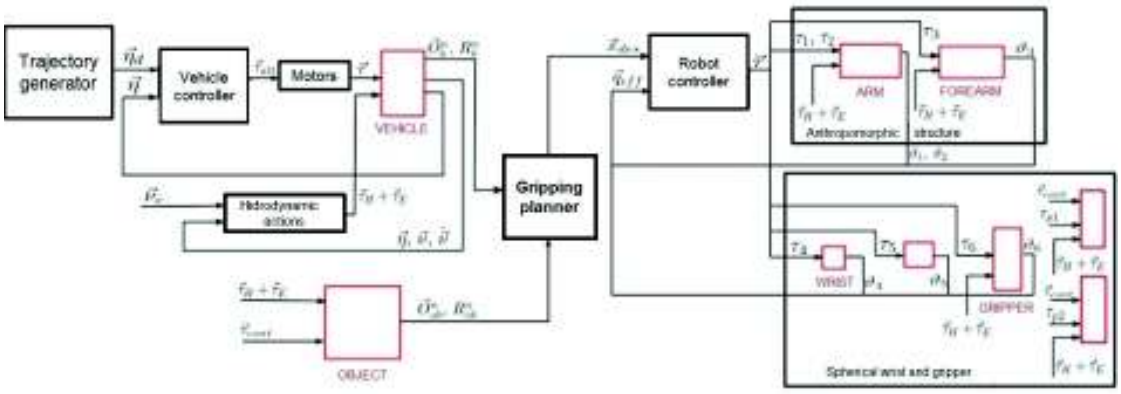

Figure 3.7: Control logic, with uncoupled controller, of the I-AUV for underwater manipulation

[5] [7]. The trajectory planning is carried out as a function of the mission the vehicle has to complete and of the environment information such as, for instance, the position of the object it has to catch. Many trajectory planning strategies can be currently found in the multibody system literature, concerning different kinds of vehicles. The main approaches are usually based on path following and tracking techniques. In this research activity a path following approach is studied since it turned out to be quite suitable for the AUV applications, e.g. for under-actuated vehicles [1] [11]. The vehicle control has to keep the AUV along the desired trajectory, modifying it, if necessary, to make the catching and the object manipulation easier. Finally the arm control has to enable the object catching from the gripper which is mounted on the arm itself, considering at the same time the desired trajectory the vehicle has to follow. In this phase a fundamental role will be played by the gripper-object contact [26] that will have to be accurately described from a multibody point of view.

3.4.1 Planning of the grasping trajectory

In order to estimate the property of robustness of the uncoupled control strategies (for the AUV and robotic arm), a complex underwater mission of the I-AUV is planned; the mission consists in grasping an object (generally mobile) simultaneously with the moving forward of the vehicle on a desired trajectory. The achievement of this type of mission requires that the skills of mobile manipulation of the vehicle have to be activated during its navigation, stressing, this way, the dynamic coupling of the system; the controllers will have thus to face non negligible disturbances. Such operations are typically carried out with the vehicle in course of hovering, i.e. in a phase where the problem of the dynamic coupling is drastically reduced. The problem is shown in a completely general form in

Figure 3.8. The vehicle is supposed to move on a desired trajectory, defined in terms of a geometrical path and an associated time law of motion, planned by the trajectory generator on board of the vehicle. The navigation trajectory can be consequently described by the distance vector between the origin of the body system $< b >$ and the origin of the NED system $< n >$, $\vec{O}_b^n$, expressed in the fixed frame, and by the rotation matrix R_b^n:

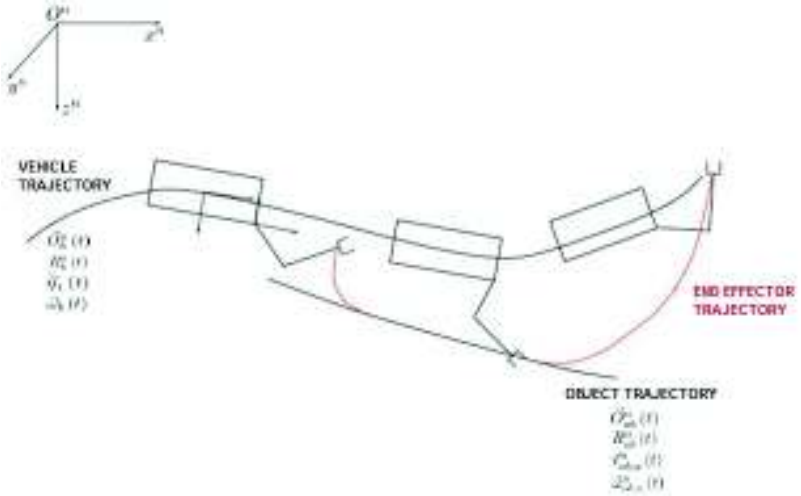

Figure 3.8: Planning of the trajectory to grasp a mobile object

$$\begin{aligned} \vec{O}_b^n &= \vec{O}_b^n(\pi) \\ R_b^n &= R_b^n(\pi) \quad \Rightarrow \quad \vec{O}_b^n = \vec{O}_b^n(t)\ ,\ R_b^n = R_b^n(t)\ . \\ \pi &= \pi(t) \end{aligned} \tag{3.34}$$

The planning of the path and of the time law is carried out in order to make the grasp [27] of the object easier: the vehicle needs to come gradually closer to the object near the grasping point, to make the intervention possible facing the limited arm and forearm length; moreover it is advisable to reduce the speed of the I-AUV compared to the one of the cruise phase, to increase the time for the grasping and thus limit the accelerations required to the joints. $\dot{\vec{\eta}}_1(t)$ is the absolute velocity of the center of mass of the vehicle, while $\vec{\omega}_b(t)$ is its angular velocity, both expressed in the NED frame. As regards the motion of the object, its trajectory is supposed to be known beforehand, as to an inertial reference. Of course, this hypothesis is generally not checked in practice, as neither the exact geometrical shape nor the trajectory of the object itself are initially known. In these cases it will be left to the intelligence on board, thanks to the outputs of the sensors (e.g. optic or acoustic sensors) to reconstruct the shape and the trajectory of the object and consequently to state the best strategies to complete the grasping operation. So right now, the motion of this body is supposed to be described through the following kinematic quantities:

$$\vec{O}^n_{\text{ob}} = \vec{O}^n_{\text{ob}}(t), \;\; R^n_{\text{ob}} = R^n_{\text{ob}}(t) \; , \tag{3.35}$$

representing the position and the orientation of the object with respect to an inertial system, expressed in $< n >$ frame. Besides, in the same reference frame the absolute linear and angular velocities $\vec{\text{v}}^n_{\text{ob,a}}$ and $\vec{\omega}^n_{\text{ob,a}}$ are known. The case of a still object is a particular sub-case where the position and the orientation in the inertial system are constant (null speeds). To plan the trajectory of the end-effector of the manipulator in the operative space first of all it is necessary to get, on the basis of the knowledge of the kinematic quantities of the centre of mass of the vehicle, the description of the trajectory of the shoulder of the robotic arm, where is fixed the origin of the $< 0 >$ reference frame, according to DH convention. Consequently, it is obtained:

$$\vec{O}^n_0 = \vec{O}^n_b + R^n_b \vec{O}^b_0, \;\; R^n_0 = R^n_b R^b_0 \; , \tag{3.36}$$

where, with the reference frames shown in Figure 3.8, $\vec{O}^b_0 = \left[\frac{B}{2}, 0, -\frac{H}{2}\right]^T$ and $R^b_0 = R_x(\pi)$. Moreover, according to the fundamental formula of the rigid motions:

$$\vec{\text{v}}^n_{0,\text{a}} = \dot{\vec{\eta}}_1 + \vec{\omega}_b \times \left(\vec{O}^n_0 - \vec{O}^n_b\right), \;\; \vec{\omega}^n_{0,\text{a}} = \vec{\omega}_b \; . \tag{3.37}$$

Successively, is it possible to move from the description of the absolute motion of the object to the description of the I-AUV relative motion, thanks to the following kinematic relations:

$$\vec{O}^0_{\text{ob}} = R^{n\,T}_0 \left(\vec{O}^n_{\text{ob}} - \vec{O}^n_0\right), \;\; R^0_{\text{ob}} = R^{n\,T}_0 R^n_{\text{ob}} \; , \tag{3.38}$$

where $\vec{O}^0_{\text{ob}} = \vec{O}^0_{\text{ob}}(t)$ and $R^0_{\text{ob}} = R^0_{\text{ob}}(t)$ set out the trajectory of the object with respect to the vehicle. The values of linear and angular velocity of the object as to the DH reference frame $< 0 >$ (the reference frame rigidly connected to the object) are extracted as follows:

$$\vec{\text{v}}^0_{\text{ob,r}} = R^{n\,T}_0 \left(\vec{\text{v}}^n_{\text{ob,a}} - \vec{\text{v}}^n_{0,\text{a}}\right), \;\; \vec{\omega}^0_{\text{ob,r}} = R^{n\,T}_0 \left(\vec{\omega}^n_{\text{ob,a}} - \vec{\omega}^n_{0,\text{a}}\right) \; . \tag{3.39}$$

Equations (3.38) allow to define the trajectory of the object in the operative space of the manipulator end-effector, expressible as:

$$\vec{x}_{\text{ob}}(t) = \begin{bmatrix} \vec{O}^0_{\text{ob}}(t) \\ \vec{\Phi}^0_{\text{ob}}(t) \end{bmatrix} \; , \tag{3.40}$$

where vector $\vec{\Phi}^0_{\text{ob}}$ contains RPY Euler angles extracted by rotation matrix R^0_{ob}. The trajectory of the object, at first, does not match the gripper one, which is in a position of rest; to get the grasping it is necessary the trajectory of the gripper is rapidly brought to match the

trajectory of the object, and that the two paths are the same (both as regards the position part and the orientation one) for a period of time ΔT long enough to operate the gripper and allow the grasping of the body. This period ΔT is mandatory to allow a correct grasping; if the manipulator had a robotic arm, or a gripper, more articulated, the operation could also take place with a relative motion between the body and the end-effector, or with a very little time gap of common motion between the two. Since, nevertheless, in the presented case the gripper is formed of just two movable bodies connected to the last link of the wrist, the end-effector is required to be positioned and remain, for a sufficient lapse of time, in that position as to the object that makes easier the grasping. When the operation is over, the trajectories of the object and the end-effector break up again and the arm e.g. can go back to a configuration of rest, fixed as to the vehicle. To optimize the performances of the arm controller and the vehicle one it is necessary to guarantee that the trajectory of the end-effector in the operative space is sufficiently smooth, so that the forces required to the actuators of the joints will not excite the system modes (not modelled). A possible process allowing the generation of a trajectory which meets such requirements is the following: the error is set out, in the operative space, between the object pose and the end-effector one,

$$\vec{e} = \vec{x}_{\text{ob}}(t) - \vec{x}_{\text{des}}(t) \ , \tag{3.41}$$

for which a time trend is defined beforehand. Particularly, each component of $\vec{e}$ has an evolution shown in Figure 3.9, with a trapezoidal speed profile.
The progress chosen for $e_i(t)$ is made up of a linear section which is joined with two parabolic sections in the neighbourhood of the initial and final positions. A constant value of the second derivative is chosen for the initial and final parts, $\ddot{e}_{i_c}$; the second derivative is discontinuous but always limited. When this value has been chosen, with $\text{sign}\left(\ddot{e}_{i_c}\right) = -\text{sign}(e_i(0))$, and $e_i(0)$ calculated through the direct kinematics, it is found:

$$t_c = \frac{t_f}{2} - \frac{1}{2}\sqrt{\frac{t_f^2\left|\ddot{e}_{i_c}\right| - 4|e_i(0)|}{\left|\ddot{e}_{i_c}\right|}} \ , \ \left|\ddot{e}_{i_c}\right| \geq \frac{4|e_i(0)|}{t_f^2} \ . \tag{3.42}$$

Once the trend of each of the 6 components of $\vec{e}$ is known, from (3.41) the trajectory of the end-effector, specified in the operative space can be evaluated:

$$\vec{x}_{\text{des}}(t) = \begin{bmatrix} \vec{O}^0_{\text{e,des}}(t) \\ \vec{\Phi}^0_{\text{e,des}}(t) \end{bmatrix} \ , \tag{3.43}$$

where $\vec{O}^0_{\text{e,des}}$ is the origin of Denavit-Hartenberg frame of the last link of the robotic arm, which, with RPY Euler's angles of the same frame with respect to $< 0 >$ $\vec{\Phi}^0_{\text{e,des}}$, allows to get the homogeneous transformation matrix $T^n_0\left(\vec{q}_{\text{des}}\right)$; from this matrix, through the in-

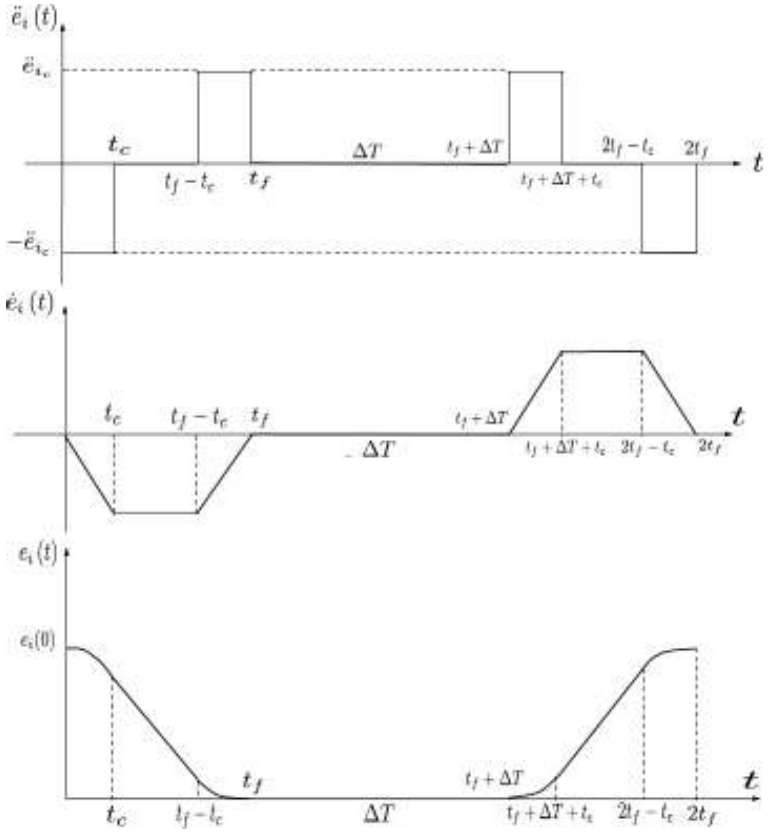

Figure 3.9: Time evolution of the generic component of the trajectory tracking error $e_i(t)$

verse kinematics, the vector of the desired joint coordinates $\vec{q}_{\text{des}}$ is calculated. If the I-AUV control is sufficiently ready and robust, tracking this desired trajectory in the joint space and moving the gripper in an appropriate way, the I-AUV mission of the object grasping concludes successfully.
The strategies of uncoupled control have been studied through the simulation architecture of the whole I-AUV system developed in a Matlab-Simulink^{TM} environment. The rigid dynamics of the vehicle and the robotic arm is reproduced through the software tool for multibody modelling SimMechanics: this tool allows the I-AUV description through blocks representing rigid bodies, joints, sensors and elements of force and, successively, the formulation and solution of the equations of motion of the whole mechanical system. In the Simulink^{TM} environment are instead implemented the modelling blocks of the vehicle and manipulator controllers, the trajectory generators and the blocks of the hydrodynamic action characterization. To analyse the performances of the proposed control typologies, and considering the complexity of the problem under examination, compared to the one concerning the simulation of a single AUV mission, the state of the dynamic system is assumed to be known, in order to carry out an analysis independent from the quality of the measurement system. Besides, a controller working with a 100 Hz frequency is used.

3.5 Simulation results

In order to evaluate the performances of the proposed strategy, the results of a simulated rescue mission of an underwater object in motion are shown (e.g. a spherical object). The mission results have been achieved with an uncoupled control strategy, in particular:

- for the vehicle both path following (navigation and control) and PID SISO controllers have been tested (strategies already described in chapters 1 and 2);
- for the manipulator (a redundant one to avoid the singularities) the differential inverse kinematics with a 7 DOFs SISO PID controller has been adopted.

Unlike the previous chapters, the current results concerning the I-AUV are only simulated. The MDM Lab of the University of Florence has just started a National project (called SUONO: Safe Underwater Operations iN Oceans) dealing also with I-AUVs and thus it will be, hopefully, possible to apply soon these ideas to a real underwater vehicle.
Starting from the knowledge of the trajectory of the object, the gripper is controlled to match this trajectory (target), and after a time interval ΔT suitable for the grasping the manipulator moves back in its rest configuration with respect to the vehicle. The mission results have been achieved through a 7 DOFs PID controller for the manipulator (basically, adding 1 redundant DOF to the standard anthropomorphic manipulator to be able

to avoid the singularities) and an uncoupled path following strategy for the AUV (suitable also for under-actuated vehicles [11]).
The spherical object moves forward with a speed of 0.04 m/s, keeping a constant depth (as to the frame $< n >$) equal to -0.18 m and following the trajectory shown in Figure 3.10. The vehicle navigation is controlled to adapt its trajectory to the object one, approaching the object, to facilitate the grasping: in the proposed example, the I-AUV moves forward, along x^n axis with a limited speed of 0.05 m/s and navigating at a constant reference depth. The manipulator, fixed at the beginning in its rest configuration, is activated and controlled to track the planned trajectory for the grasping (Figure 3.10).

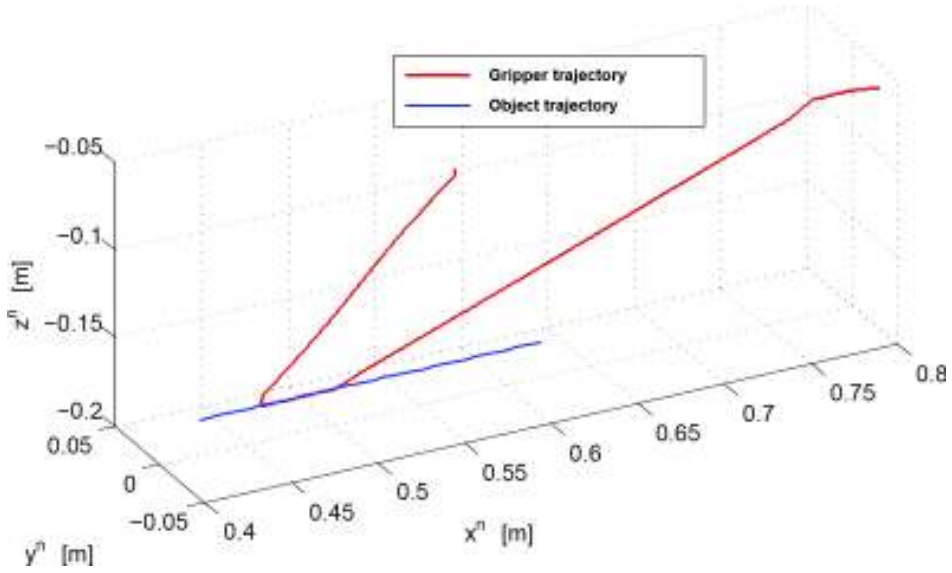

Figure 3.10: Underwater simulated trajectories of the manipulator end-effector and of the object

The gripper position moves rapidly to the target, in accordance with the planned trend of error $\vec{e}(t)$. Particularly as concerns $\vec{e}(t)$, the following parameters have been chosen, with reference to Figure 3.9, in order to have an end-effector trajectory smooth enough: $t_c = 2$s, $e_{i_c} = 0.5$m/s^2 and $\Delta T = 1$s.
The two paths match, with a limited error (a few mm), for 1 s; then the gripper gets back in its rest configuration as to the vehicle (which, during the grasping, has moved of about 0.25 m).
During the grasping intervention, the gripper maintains its orientation with respect to the NED frame: according to the arm motions, the wrist joints rotate to comply with the desired orientation of the gripper. The reference roll, pitch and yaw angles are hold with a maximum error of 0.04 rad, caused mainly by the vehicle motion.
The time trend of the position error of the vehicle is shown in Figure 3.11. The error reaches a maximum value of 4 mm at the time the manipulator starts moving, and re-

mains limited in time (about 10^{-3} m). The orientation errors are also shown, in terms of roll, pitch and yaw angles of the body frame $< b >$ compared to the desired ones (in this example, the desired ones are equal to zero, as the vehicle has to navigate in the forward direction, along x^n axis, keeping its initial orientation). These errors are important as they are linked to the time trends of the desired joint variables: the trajectory tracking of the AUV has to be accurate, to have, in the operative space, a smooth desired end-effector trajectory (linked to $\vec{q}_{\text{des}}(t)$). In the proposed case, the roll and pitch error orders are about 10^{-3} rad, while the maximum yaw error is (0.07 rad): the propulsion system is able to compensate the disturbances due to the manipulator motion.

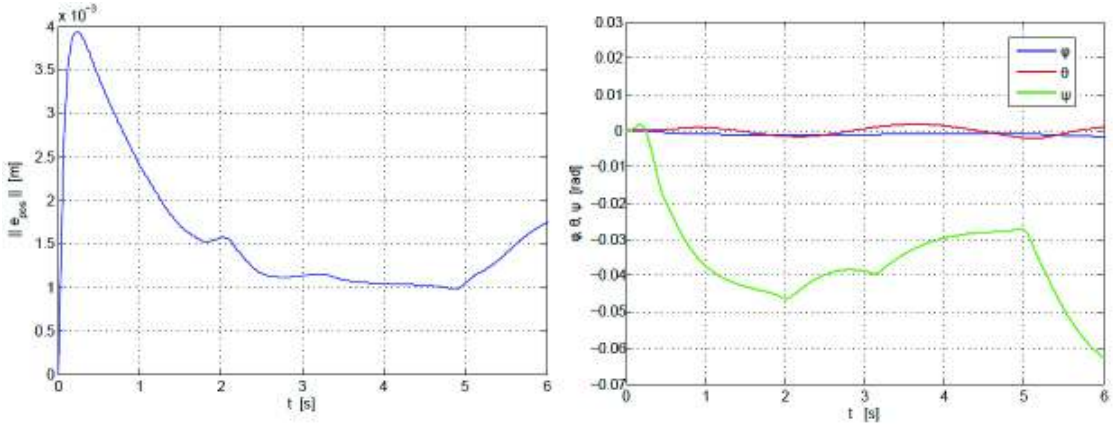

Figure 3.11: Time evolution of the position error and of the orientation errors of the vehicle

Finally, in Figure 3.12 the joint errors are shown, less than (0.01 rad for the shoulder and elbow joints, 10^{-4} rad for the wrist joints).

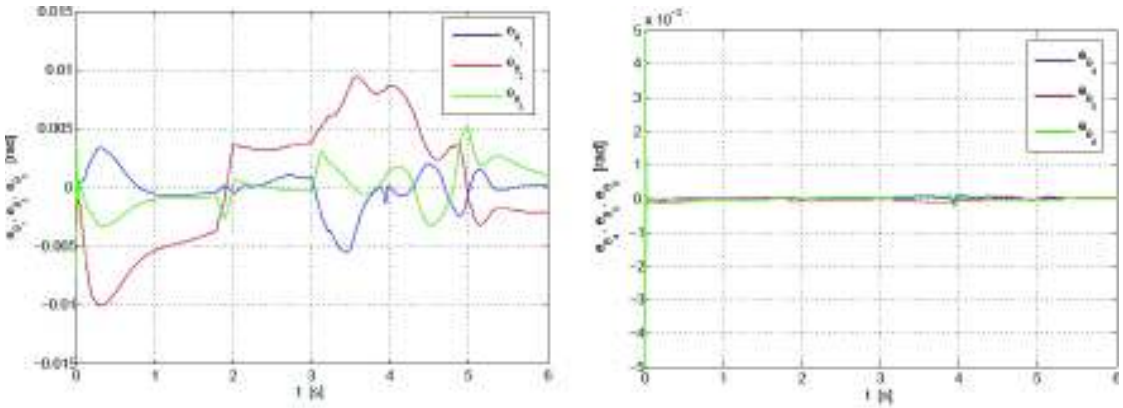

Figure 3.12: Time evolution of the joint errors of the manipulator: anthropomorphic structure and spherical wrist

To summarize, in this chapter the description of the multibody modelling and the control strategy of an AUV specifically thought for the underwater mobile manipulation,

usually called I-AUV (AUV for Intervention), has been presented. These devices, because of their fundamental applications in the military field, in underwater explorations (e.g. archaeological field) and in the industrial field (e.g. for Oil&Gas), can undoubtedly lead to substantial economic and technological benefits. The performances of such an AUV have to meet strict planning and control specifications, both as regards the vehicle itself and as for the manipulation phase. The multibody model of the vehicle and of the robotic arm considers all the DOFs of the I-AUV, coupling the classical hydrodynamic equations with the multibody approach; in the same way the multibody model of the gripper part accurately describes the dynamics of the object to be grasped. At the moment a path following approach is considered. The vehicle control keeps the AUV along the desired trajectory, modifying it, if necessary, to make the catching and the object manipulation easier. The arm control enables the object catching from the gripper which is mounted on the arm itself, considering at the same time the desired trajectory the vehicle has to follow.
The preliminary simulation results of the proposed uncoupled control strategy have been satisfactory. Further developments are scheduled in order to reach a more realistic simulation, before the hardware testing phase: particularly further efforts will be addressed to the acquisition process of the information of the object to be grasped (e.g. acoustic or optical feedbacks) and to autonomy calculations.

Conclusions

In the present work the modelling, the control and the construction of underwater robots, developed by the Mechatronics and Dynamic Modelling Laboratory (MDM Lab) of the Department of Industrial Engineering of the University of Florence during the years 2011-2013 have been described. The studies of the presented vehicles, in particular an AUV, a ROV and preliminary simulations about an I-AUV started thanks to the funding for underwater archaeologist purposes.

In chapter 1 the development of Typhoon AUV, designed and built by MDM Lab, is reported: it is a result of the awarding of the THESAURUS project in 2010 (TecnicHe per l'Esplorazione Sottomarina Archeologica mediante l'Utilizzo di Robot aUtonomi a Sciami) from Regione Toscana. The work developed on THESAURUS dealt with the project of navigation algorithms through the use of on board sensors, integrated in a mathematical model implemented in Matlab-Simulink^{TM} environment [1]. The theoretical model and the first experimental results of navigation in the sea have been here discussed.

During the THESAURUS project, the MDM Lab thanks to the collaboration with the Department of the Earth Sciences of the University of Florence developed a mini-ROV, called Nemo (chapter 2). It has been specifically designed and built to monitor the Costa Concordia wreck, at Isola del Giglio. Particularly the submarine, remotely piloted, has to operate as a robotised camera and be able to scan the wreck inside areas too. The second specification identifies with the very reasonable dimensions of the vehicle and the high control accuracy of its movements in restricted environments. In the present work the ROV development, the implemented navigation strategy and some experimental results are given.

Finally, a research topic in the advanced underwater robotics field is faced in chapter 3. The possibility to mount a robotic arm on a AUV is investigated, in the simulation environment, addressing forward complex mobile robots known as I-AUVs (Intervention - Autonomous Underwater Vehicle). The possibility to use an on board manipulator on an autonomous underwater vehicle is a complex topic of research (concerning the AUVs

only a few examples of vehicles equipped with a robotic arm are present in literature), e.g. because of problems of autonomy. Some preliminary simulation results concerning a possible planning of a task of robotic manipulation for the rescue of a object floating in water are treated in the final part of the dissertation.

The performed activities during these years (2011-2013) have improved my knowledge concerning the field of underwater robotics; in this sense, a significant contribution was definitely provided by the interesting experimental campaigns where I was lucky enough to be able to participate.

Bibliography

[1] Fossen T. I., *Guidance and Control of Ocean Vehicles*, 1st ed., John Wiley & Sons, Chichester UK, 1994.

[2] Hildebrandt M., Christensen L., Kerdels J. et al., *Realtime Motion Compensation for ROV-based Tele-operated Underwater Manipulators*, IEEE Robotics & Automation Magazine, Bremen, 2009.

[3] Christensen L., Kampmann P. et al., *Hardware ROV Simulation Facility for the Evaluation of novel Underwater Manipulation Techniques*, IEEE Robotics & Automation Magazine, Bremen, 2009.

[4] Siciliano B., Khatib O., *Handbook of Robotics*, Springer Handbooks, Napoli and Stanford, 2008.

[5] Antonelli G., *Underwater Robots*, Springer Tracts in Advanced Robotics, Springer-Verlag, 2nd edition, Heidelberg, 2006.

[6] Marani G., Choi S. K., Yuh J., *Underwater autonomous manipulation for intervention missions AUVs*, Ocean Engineering Journal, University of Hawaii, 2008.

[7] D. M. Lane, J. B. C. Davies, G. Casalino et al., *AMADEUS: Advanced MAnipulation for DEep Underwater Sampling*, IEEE Robotics & Automation Magazine, Universitat de Barcelona, 1997.

[8] THESAURUS project (2011-2013), *http://thesaurus.isti.cnr.it/*

[9] ARROWS project (2012-2015), *http://www.arrowsproject.eu/*

[10] SAUC-E 2012-2013, *http://sauc-europe.org/*

[11] Breivik M., Fossen T. I., *Giudance-Based Path Following for Autonomous Underwater Vehicles*, in Proceedings of the OCEANS'05, Washington D.C., USA, 2005.

[12] Sanz P. J., Ridao P., Oliver G. et al., *TRIDENT: a Framework for Autonomous Underwater Intervention Missions with Dexterous Manipulation Capabilities*, in the 7th Symposium on Intelligent Autonomous Vehicles, Lecce, 2010.

[13] Carlton J., *Marine Propellers and Propulsion, 2nd edition*, Elsevier, 2007.

[14] Lee S.K., *CFD Simulation for Propeller Four-Quadrant Flows*, ABS TECHNICALPAPERS, 2006.

[15] Sciavicco L., Siciliano B., *Robotica industriale Modellistica e controllo di manipolatori*, McGraw-Hill Libri Italia, I, 2nd Edition, Milano, 2000.

[16] Mathworks, *www.mathworks.it*

[17] Pan-Mook L., Bong-Huan J., Kihun K., Jihong L., Aoki T., Hyakudome T., *Simulation of an Inertial Acoustic Navigation System With Range Aiding for an Autonomous Underwater Vehicle*, IEEE Journal of Oceanic Engineering, vol.32, no.2, pp.327-345, April 2007.

[18] Park M., *Error analysis and stochastic modeling of MEMS based inertial sensors for land vehicle navigation applications, M.Sc. Thesis*, Department of Geomatics Engineering, University of Calgary, Canada, 2004.

[19] Gebre-Egziabher D., *Design and Performance Analysis of a Low-Cost Aided Dead Reckoning Navigator*, PhD Thesis, Standford University, 2004.

[20] Fofonoff N. P., Millard R. C. Jr., *Algorithms for computation of fundamental properties of seawater*, UNESCO technical papers in marine science, No. 44. UNESCO Division of Marine Sciences, Place de Fontenoy, 75700 Paris, 1983.

[21] Toni P., Giusti R., Meli E. et al., *Dispense del corso di meccanica applicata*, Università degli Studi di Firenze, 2012.

[22] Cheli F., Pennestrì E., *Cinematica e dinamica dei sistemi multibody*, Casa Editrice Ambrosiana, Milano, 2006.

[23] Fox R. W., McDonald A. T. , *Introduction to fluid mechanics*, VI Ed., John Wiley & Sons, USA, 2004.

[24] Allotta B., Fioravanti D., Malvezzi M., *Note alle lezioni di Modellistica e Controllo di Sistemi Meccanici*, Università degli Studi di Firenze, 2007.

[25] Allotta B., Costanzi R., Monni N., Pugi L., Ridolfi A., and Vettori G., *Design and Simulation of an Autonomous Underwater Vehicle*, in Proceedings of the European Congress on Computational Methods in Applied Sciences and Engineering, ECCOMAS 2012, Vienna, Austria, Sept. 10-14, 2012.

[26] Magheri S., Malvezzi M., Meli E., and Rindi A., *An innovative wheel-rail contact model for multibody applications*, Wear, vol. 271, pp. 462-471, 2011.

[27] Murray R. M., Li Z., *A Mathematical Introduction to Robotic Manipulation*, CRC Press, 1994.

[28] Allotta B., Conti R., Costanzi R., Giardi F., Meli E., Ridolfi A., *Modelling and Control of an Autonomous Underwater Vehicle for Mobile Manipulation*, in Proceedings of Multibody Dynamics 2013 Congress (ECCOMAS), Zagreb, Croatia, 2013.

[29] Bolzern P., Scattolini R., Schiavoni N., *Fondamenti di controlli automatici*, 3rd ed., McGraw-Hill, Milano, 2008.

[30] MOOS-IvP Software, `http://moos-ivp.org`.

[31] Qt Project, `http://qt-project.org`.

[32] Remotely Operated Vehicles Committee of the Marine Technology Society, `http://www.rov.org`.

[33] Yang K. C., Yuh J., Choi S. K., *Experimental Study of Fault-Tolerant System Design for Underwater Robots*, in Proceedings of IEEE Int. Conf. Robot. and Autom., vol. 2, pp. 1051-1056, 1998.

[34] Ehsani M., Gao Y., Emadi A., *Modern Electric, Hybrid Electric, and Fuel Cell Vehicles: Fundamentals, Theory, and Design*, CRC PRESS, 2009.

[35] Byron J., Tyce R., *Designing a Vertical/Horizontal AUV for Deep Ocean Sampling*, in Proceedings of OCEANS 2007, Sept. 29 - Oct. 4, 2007.

[36] Caffaz A., Caiti A., Casalino G., Turetta A., *The Hybrid Glider-AUV Folaga*, IEEE Robotics and Automation Magazine, Vol. 17, Issue 1, March 2010.

[37] J. G. Ziegler, N. B. Nichols, *Optimum Settings for Automatic Controllers*, Trans. ASME, vol. 64, pp. 759-768, 1942.

[38] Allotta B., Bartolini F., Costanzi R., Gelli J., Monni N., Natalini M., Pugi L., Ridolfi A., Vettori G., *The Thesaurus Project: AUV software design*, Oren Gal, Advanced in marine robotics, LAP publisher, pp. 93-120, 2013.

[39] Bartolini F., Conti R., Costanzi R., Gelli J., Meli E., Monni N., Natalini M., Ridolfi A., Allotta B., Toni P., *SAUC-e 2013 - UNIFI Team - FeelHippo vehicle*, SAUC-E (Student Autonomous Underwater Vehicle Challenge - Europe) 2013, La Spezia, 2013.

[40] Bartolini F., Costanzi R., Monni N., Ridolfi A., Vettori G., Giardi F., Allotta B., *SAUC-E 2012 - UNIFI Team - Turtle vehicle*, SAUC-E (Student Autonomous Underwater Vehicle Challenge - Europe) 2012, La Spezia, 2012.

[41] Allotta B., Pugi L., Bartolini F., Costanzi R., Ridolfi A., Monni N., Gelli J., Vettori G., *The Thesaurus Project, a long range AUV for extended exploration, surveillance and monitoring of archaeological sites*, in Proceedings of the V International Conference on Computational Methods in Marine Engineering, ECCOMAS MARINE 2013, Hamburg, Germany, 2013.

[42] Pivano L., Johansen T. A., Smogeli Ø. N., *A Four-Quadrant Thrust Estimation Scheme for Marine Propellers: Theory and Experiments*, IEEE Trans. on control systems technology, Vol. 17, N. 1, Jan. 2009.

[43] Pivano L., Whitcomb L. L., Johansen T. A., Fossen T. I., *Preliminary Simulation Studies of a new Four-quadrant Propeller Thrust Controller Applied to Underwater Vehicles*, IFAC Conference on Control Applications in Marine Systems (CAMS 2007), Croatia, 2007.

[44] Caiti A., Calabro V., Fabbri T., Fenucci D., Munafo A., *Underwater communication and distributed localization of auv teams*, In OCEANS - Bergen, 2013 MTS/IEEE, 2013.

[45] Mahony R., Hamel T., Pflimlin J. M., *Non-linear complementary filters on the special orthogonal group*, IEEE Transactions on Automatic Control, vol. 53, no. 5, pp. 1203-1218, 2008.